Active and passive magnetic shielding for use in OPM-MEG

Lucy Jane Edwards MSci

School of Physics & Astronomy

Thesis submitted to the University of Nottingham for the degree of Doctor of Philosophy

March 2024

Contents

Abstract

Magnetic shielding is an essential part of many sensitive experiments including magnetoencephalography (MEG) systems that measure tiny magnetic fields generated by the simultaneous firing of neurons in the brain. Recent advances in MEG have arisen due to the use of head mounted optically pumped magnetometers (OPMs).

MEG scans must be carried out inside magnetically shielded rooms (MSRs). Passive shields made up of several layers of ferromagnetic material, combined with active shielding using electromagnetic coils, create very low magnetic field environments which enable OPMs to detect femtotesla brain fields.

In order to open up the scanning environment, and increase the range of patient movement, the coils must be mounted on the walls of the MSR. However, as the coils move closer to the ferromagnetic walls, magnetic field interactions between the two occur. Therefore it is important to understand how the coils will interact with the shielding material in order to design effective shielding systems.

This thesis explores interactions between electromagnetic coils and the ferromagnetic walls of a magnetic shield by comparing experimental measurements of magnetic fields produced by a small circular coil mounted onto the inside face of a single layer, 55 × 55 × 55 cm^3 MuMetal box, to a mathematical model describing the interaction of a planar coil close to an infinite plane with high magnetic permeability.

Furthermore, this thesis investigates how the shielding factor of a magnetic shield can be enhanced using a technique called ‘shaking’. Tests were carried out on a three layer MuMetal magnetic shield made up of nested cylinders, which showed that the shielding factor for low frequency magnetic fields could be improved by applying alternating currents to coils wound around the MuMetal during an experiment. This could be a potential solution to improving the shielding factors of lighter magnetically shielded rooms used for OPM-MEG.

Finally, this thesis explores a new method to enable the nulled volume produced by a coil system to move with a sensor during an experiment, by continuously driving the nulling coils surrounding the sensor with unique frequencies. Experiments were carried out using a fluxgate magnetometer inside the 55 × 55 × 55 cm^3 MuMetal box. The methods used to carry out the continuous calibration and field cancellation are outlined and a custom LabVIEW program, which was developed to control the magnetic field during experiments, is described. Experiments showed that the magnetic field at the fluxgate magnetometer could be nulled during both translations and rotations.

Improving the shielding factor of magnetically shielded rooms, and also understanding how passive and active magnetic shielding techniques interact, is important as we move towards producing lighter magnetic shields which will rely more on active shielding to operate at efficiencies equivalent to their multi-layer counterparts. Furthermore, development of lighter magnetic shields will help enable OPM-MEG to become an affordable and widely used brain imaging technique.

Acknowledgements

Firstly I would like to start by thanking my supervisor, Richard Bowtell, for all of your support and guidance throughout the PhD. I have thoroughly enjoyed working with you!

Thank you to Niall and Jim for teaching me so much about shielding and coils. I have learnt so much from you both and will miss being a part of shielding club.

I'd like to thank my industrial sponsor Magnetic Shields Ltd, especially Prash, Ben, Xavier, and Jack for all of your help during my placement.

I want to thank my precious Hobbits, Molly and Izzy, for all of the laughs, your friendship and your encouragement.

To Adam, thank you for being there for me, for all of your love and cuddles, and also all those cups of tea in the mornings!

I'd like to thank my family, including Grandma Wynne, Grandma Sue, and Grandad Mike, for always believing in me.

And finally to Mum, Dad, and Will, this work would not have happened without your never-ending love and support. Thank you for always being there for me and getting me across the finishing line. I couldn't have done it without you!

Chapter 1

Introduction and Overview

1.1 Introduction

Magnetic shielding is an essential part of any experiment that requires an extremely low magnetic field environment, including, for example, the measurement of the neutron electric dipole moment (Baker et al. [2006]) and cold atom interferometers (Hobson et al. [2022]). This is especially true for the functional brain imaging technique magnetoencephalography (MEG), where tiny magnetic fields from the brain are measured using highly sensitive magnetic field sensors (Hämäläinen et al. [1993]). Advances in wearable MEG using optically pumped magnetometers (OPMs) has enabled functional brain imaging whilst participants are moving (Boto et al. [2018], Tierney et al. [2019], Seymour et al. [2021]). However, OPMs have very stringent background magnetic field requirements necessitating a background field <1 nT.

Passive magnetic shielding using ferromagnetic materials is highly efficient, especially when combined with active magnetic shielding in the form of electromagnetic coils (Bork et al. [1980],Altarev et al. [2015b]). Traditionally, many layers of shielding material are used to build magnetic shields. However, to create a magnetically shielded room (MSR) with a large working volume, this means shields are heavy and costly. For OPM-MEG to become a mainstream functional brain imaging technique, lighter and more affordable shields are needed (Holmes et al. [2022]). This means being able to adapt shields to fit inside existing buildings and also using fewer layers of shielding material whilst maintaining very low background magnetic fields.

Lighter magnetically shielded rooms with fewer layers of shielding material will rely more heavily on active shielding techniques to maintain very low background magnetic fields. Therefore it is important to understand more about active shielding and how it can be used to further reduce remnant background magnetic fields inside magnetic shields. Furthermore, as electromagnetic coils become wall-mounted to open up space in the MSR, it is important that we fully understand the interactions between the electromagnetic coils and the ferromagnetic walls.

Magnetic field control using electromagnetic coils is an essential part of a MEG system that uses OPMs (Holmes et al. [2018, 2019]). Current field nulling technology used at the University of Nottingham only nulls over a small static volume ($40 \times 40 \times 40$ cm^3) surrounding the head-mounted OPM array. OPMs can move within this region without issue but this volume remains in a fixed position throughout experiments (Rea et al. [2021], Holmes et al. [2023a]). To enable more naturalistic patient movements during scanning, such as walking around the MSR, or even just more movement outside the fixed nulled volume, the shielded volume needs to move with the patient during scanning (Holmes et al. [2023b]).

This thesis explores some of the themes discussed above, including:

- the interactions between electromagnetic coils and the passive shielding materials,
- a shielding enhancement technique called *Shaking*,
- a field nulling technique to enable the nulled region to move with a sensor as it moves inside a magnetic shield.

The practicalities of implementing each of the techniques for use in an OPM-MEG system are also discussed.

1.2 Overview of thesis

This thesis is organised as follows:

Chapter 2 - Background

This chapter is split into three main sections.

Electromagnetism

The fundamental principles of electromagnetism are introduced in this chapter. The chapter begins with the application of Ampere's law to obtain the magnetic field produced by a long wire and circular coil. Maxwell's equations are also described.

Magnetic Shielding

Passive and active magnetic shielding. The properties of ferromagnetic materials are described and a shielding material called MuMetal is introduced. The physical shielding mechanisms involved in passive shielding are explained. Active shielding techniques using electromagnetic coils are also described.

OPM-MEG

Magnetoencephalography (MEG) is introduced as a functional brain imaging technique. OPM-MEG is introduced as a wearable alternative to cryogenic MEG. The basic physics of a zero-field OPM is described. Most importantly, this section outlines the magnetic field constraints imposed on an OPM-MEG system. The passive and active shielding techniques used to minimise the background field surrounding the OPM array are described, and the current limitations to the system are examined.

Chapter 3 - MuMetal Interactions

The first experimental chapter in this thesis investigates the interactions between passive and active shielding. A mathematical model describing the interactions between a planar circular coil and an infinite plane of ferromagnetic material is introduced. Simulations of these interactions are compared to a perfect reflection model. Experimental measurements of the magnetic field generated by a circular coil mounted onto the inside wall of a single layer MuMetal box are compared to the infinite plane simulations.

Chapter 4 - Shaking

In this chapter a shielding enhancement technique called *shaking* is demonstrated on a three layer cylindrical MuMetal shield. Shaking involves applying an additional oscillating magnetic field to the ferromagnetic walls of the shielding enclosure. This has the effect of enhancing the relative permeability of the material, so enhancing the shielding efficiency. Firstly the on-axis magnetic shielding factor of the cylinder is found. Then shaking is applied and effects on the shielding factor are determined.

Chapter 5 - Continuous Calibration

The final experimental chapter demonstrates a new technique which enables magnetic field cancellation over a moving fluxgate magnetometer by driving coils at known frequencies. Developments were carried out inside a single layer MuMetal magnetic shield with electromagnetic coils mounted to the inside faces. The chapter begins by outlining magnetic field cancellation and the importance of an accurate calibration matrix in calculating the nulling currents. A method to continuously determine the calibration matrix by driving the coils with unique frequency sinusoidal currents is shown. The LabVIEW program developed to control the system is described. Finally, application of the technique to produce a null of the magnetic field that tracks a moving fluxgate magnetometer is demonstrated. This chapter ends by discussing the potential use of this technique for field cancellation in an OPM-MEG system.

Chapter 6 - Summary and Closing Remarks

This thesis ends with a summary of the main findings presented in each of the experimental chapters and final closing remarks.

1.3 Contributions to the scientific field

This thesis contributes to our knowledge of magnetic shielding and also to the field of OPM-MEG which relies upon very low magnetic field environments.

This thesis builds upon our knowledge of how we can model magnetic shields, specifically how we can use a simple analytical model to describe the interactions between electromagnetic coils mounted on the inside faces of cubic magnetic shields. Typically, modelling such shielding geometries analytically is difficult due to the large number of boundary conditions. Here it is shown that interactions of a coil inside a cubic magnetic shield can be modelled as a coil interacting with an infinite plane. It is also shown that these interactions are not frequency dependent below 110 Hz and can be described as perfect reflections.

Shaking has been demonstrated to improve the shielding factor of a three layer cylindrical magnetic shield. This work shows how the amplitude of the shaking current and the shaking frequency can be varied to improve the shielding performance over a range of interference frequencies. This thesis also demonstrates the effects of shaking multiple layers together as well as independently.

Finally a novel magnetic field nulling technique is demonstrated which enables a magnetically nulled volume to track a fluxgate magnetometer as it moves inside a magnetic shield. This technique has the potential of being used in an OPM-MEG system to continuously null the magnetic field over a moving array of OPMs whilst a participant is being scanned. This technique is implemented by continuously driving electromagnetic coils inside the shield at known frequencies and measuring the magnetic field per unit current produced by the coils. From these measurements the coil currents needed to null a change in the static background magnetic field at the position of the sensor can be inferred, enabling real time magnetic field cancellation.

1.4 Conferences and Meetings

The work presented in this thesis has been presented at the following conferences and meetings.

1.4.1 Presentations

- **Internal MEG conference (Nottingham, September 2021)** “Towards continuous, active magnetic field cancellation on a moving array of OPMs”.
- **SPMIC seminar (Online, April 2021)** “Magnetic shielding interactions for OPM MEG”.

1.4.2 Poster Sessions

- **BIOMAG (Birmingham, August 2022)** “Towards active magnetic field cancellation on a moving array of OPMs for MEG”.
- **Workshop on Optically Pumped Magnetometers (Glasgow, October 2021)** “Towards continuous, active magnetic field cancellation on a moving array of OPMs”.
- **MEGUK (Online, September 2021)** “Towards continuous, active magnetic field cancellation on a moving array of OPMs”.
- **Quantum Technology Hub (Online, September 2021)** “Towards continuous, active magnetic field cancellation on a moving array of OPMs”.
- **Tessella Postgraduate Physics Poster Competition (Nottingham, January 2021)** “Investigating active and passive magnetic shielding interactions for OPM MEG” (Awarded 3rd place).

Chapter 2

Background

Overview of chapter

Electromagnetism

In this section the magnetic field produced by a flow of charge is introduced. Examples of the use of Ampere's law and the Biot-Savart law to determine the magnetic field produced by simple current geometries, including a long wire and a single coil loop are discussed. Maxwell's equations for electromagnetism will be explored.

Magnetic Shielding

In this section both active and passive magnetic shielding is introduced. Firstly the properties of ferromagnetic materials and their use as magnetic shielding materials are discussed. The concept of a shielding factor is explained, and the main shielding mechanisms- flux shunting and an eddy current mechanism- are introduced. Equations describing these shielding mechanisms for a spherical magnetic shield are shown. Ways to optimise the shielding factor of a passive shield are introduced. Secondly, the concept of 'active shielding' using electromagnetic coils is described. Finally we will explore how magnetic shields are built in practice and the engineering challenges surrounding the development and construction of magnetically shielded rooms.

OPM-MEG

In this section a functional brain imaging technique called magnetoencephalography (MEG) is introduced. Conventional MEG using superconducting quantum interference devices (SQUIDs) is discussed. Conventional MEG scanners are compared to a new wearable MEG scanner which uses optically pumped magnetometers (OPMs) and can be worn directly on the scalp, improving the measurement of the MEG signal. The physics describing the working of a zero-field OPM and the subsequent constraints on the background magnetic field is discussed. Current magnetic shielding techniques used in OPM-MEG are described. Finally, the future of OPM-MEG and the need for magnetic field cancellation over a moving sensor array is discussed.

2.1 Electromagnetism

2.1.1 Magnetostatics

A constant current, I flowing through a long wire will produce a magnetic field, B perpendicular to the wire, as shown in Figure 2.1.

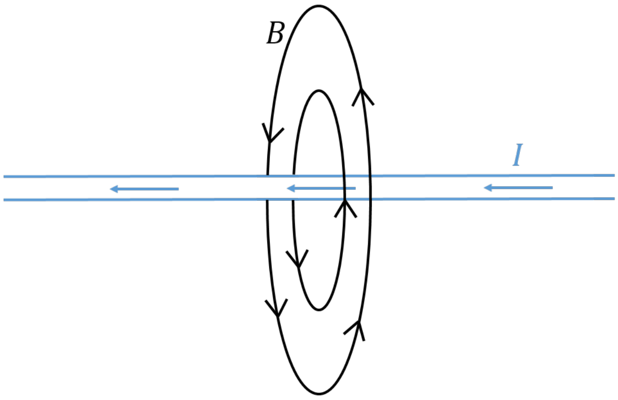

Figure 2.1: *A diagram showing the magnetic field produced by a current-carrying wire. A constant current, I, produces a magnetic field, B.*

The direction of the magnetic field can be determined using the "right hand rule", where the thumb of the right hand points along the direction of the current and the fingers curl in the direction of the magnetic field.

2.1.1.1 Ampere's law

The magnetic field a distance, r away from a long current carrying wire (shown in Figure 2.2) can be found using Ampere's circuital law.

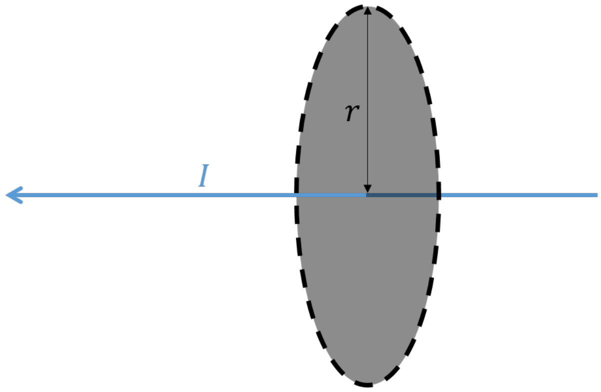

Figure 2.2: *A diagram of Ampere's law. The circular path of the magnetic flux density indicated by a black dashed line, a distance, r from a long current carrying wire which flows through the surface area (grey) bound by the path.*

Ampere's law states that the circulation of the magnetic flux density around a closed path is proportional to the total current density, $\vec{J}$ through the surface area, $d\vec{s}$ bounded by the path and is written as

$$\oint \vec{B} \cdot d\vec{l} = \mu_0 \int \vec{J} \cdot d\vec{s}, \tag{2.1}$$

where μ_0 is the permeability of free space ($4\pi\times$ 10^{-7} Tm/A), which is a constant that describes the relationship between the magnetic flux density and the magnetic field (see also 2.2.2.1.3).

A solution for the azimuthal magnetic field, B produced at a distance, r by the current, I shown in Figure 2.2 can be found by solving Equation 2.1, such that

$$B = \frac{\mu_0 I}{2\pi r}. \tag{2.2}$$

2.1.1.2 Biot-Savart law

The Biot-Savart law can be used to determine the magnetic field for current paths following more arbitrary shapes or problems with less symmetry (see Figure 2.3). The vector field, $d\vec{B}$ produced by an infinitesimally small section of current carrying wire, $d\vec{l}$ is written as

$$d\vec{B} = \frac{\mu_0 I}{4\pi} \frac{d\vec{l} \times \hat{r}}{r^2}, \tag{2.3}$$

where $\hat{r}$ is the unit vector pointing from $d\vec{l}$ to the point in space where one wishes to calculate $d\vec{B}$.

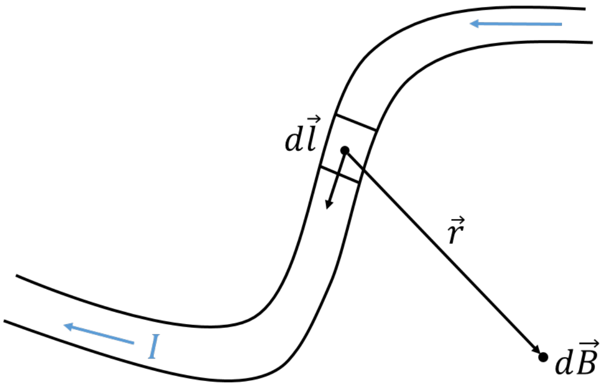

Figure 2.3: *A diagram showing how the Biot-Savart law can be used to break down an arbitrarily shaped wire path into small segments in order to calculate the magnetic field produced by the wire. An arbitrarily shaped wire path with current,* I*. The wire can be segmented into small sections,* $d\vec{l}$ *which produce a magnetic field,* $d\vec{B}$ *a distance* $\vec{r}$ *from the wire.*

To find the total field, one must integrate over the path of all of the small elements such that

$$\vec{B} = \frac{\mu_0 I}{4\pi} \int \frac{d\vec{l} \times \hat{r}}{r^2}. \tag{2.4}$$

2.1.1.2.1 Example: circular coil For example, the Biot-Savart law can be used to calculate the magnetic field at a distance, z along the axis of a circular, current-carrying wire loop (see Figure 2.4) by summing the contribution of the field from all of the small elements, $d\vec{l}$ that make up the coil.

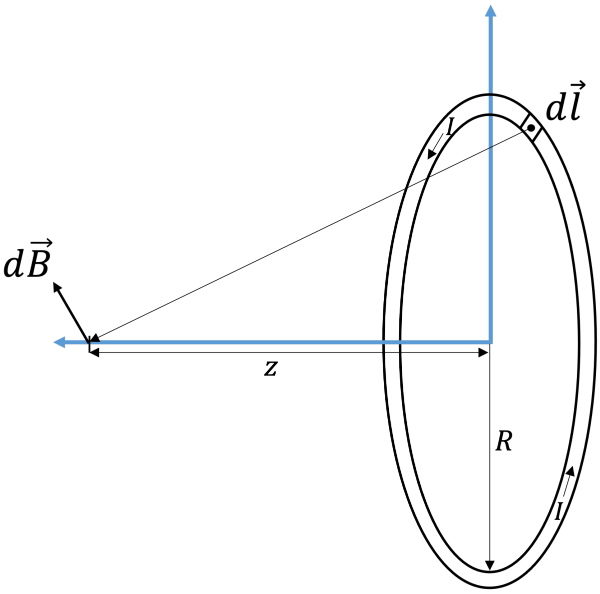

Figure 2.4: *A diagram showing how the Biot-Savart law can be used to calculate the axial magnetic field produced by a circular coil with a radius, R when a current, I flows through the coil. The coil is split into small elements, $d\vec{l}$ and the magnetic field, $d\vec{B}$ a distance produced by each element is summed to find the total field produced by the coil a distance, z from the centre of the coil.*

The axial field, B_z produced by the coil along the axis (where x=y=0) is

$$B_z = \frac{\mu_0 I R^2}{2(R^2 + z^2)^{\frac{3}{2}}} \tag{2.5}$$

where R is the radius of the coil, and I is the current flowing through the coil.

2.1.1.2.2 Example: Helmholtz coil A Helmholtz coil is a pair of identical, circular coils separated by a distance equal to the radius of the coils, as shown in Figure 2.5.

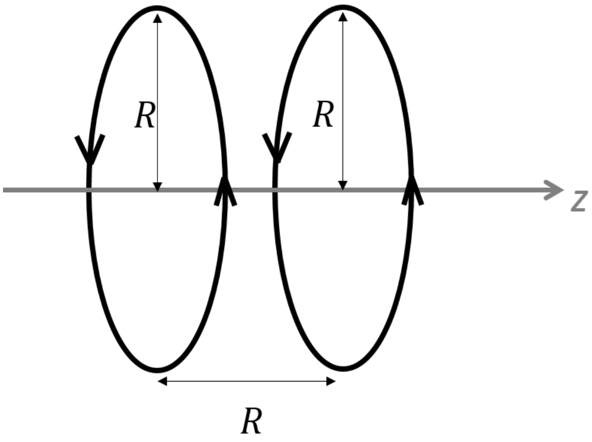

Figure 2.5: *Helmholtz coil: a pair of circular coils of radius, R separated by a distance, R.*

Using Equation 2.5, and summing the B_z contribution from each coil, the magnetic field distribution between the coils along the z-axis can be plotted (see Figure 2.6).

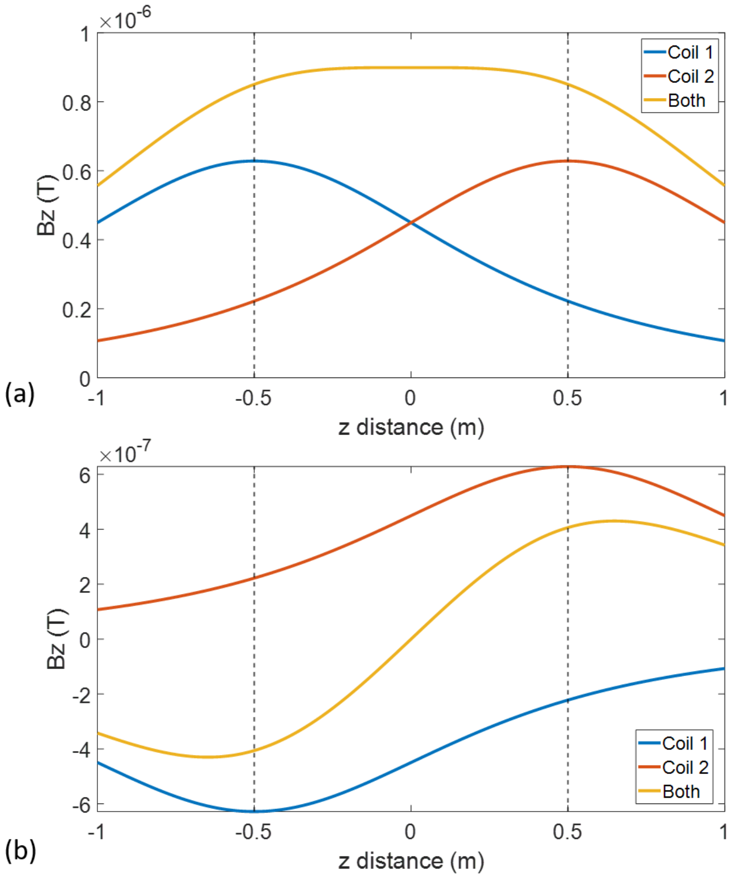

Figure 2.6: *A simulation showing how the magnetic field, B_z produced along the axis of a Helmholtz coil (where R =1 m, I =1 A) changes when the direction of current through Coil 1 is reversed. The position of each coil is shown by a dashed grey line. Coil 1 and Coil 2 are positioned at -0.5 m and 0.5 m respectively. The blue line shows the magnetic field from Coil 1 and the red line shows the magnetic field from Coil 2. The total B_z field, the summation of the field from both coils, is shown in yellow. (a) The currents through each coil are in the same direction. (b) The current through Coil 1 is reversed.*

When the current through each coil is driven in the same direction, the magnetic field along the axis of the coils constructively interferes, producing a very uniform field between the coils (shown in Figure 2.6a). Alternatively, if the direction of the current through one of the coils is switched, the magnetic field along the axis between the coils varies, creating a gradient (shown in Figure 2.6b). If the spacing between the coils is equal to $\sqrt{3}R$ the field varies linearly between the two coils. This configuration is commonly referred to as a Maxwell coil.

By varying the current through the coils, the magnetic field in the region between the coils can be controlled to create very homogeneous fields or conversely a magnetic field gradient.

2.1.2 Maxwell's equations

When currents are time-varying, the resulting electromagnetic field is also time-varying and must therefore be described by Maxwell's equations. The four unified equations describing the electric and magnetic fields and the relationships between them are:

Gauss's law for electricity

The first equation shows that the electric flux through a closed surface is proportional to the total charge contained within that surface,

$$\nabla \cdot \vec{D} = \rho, \tag{2.6}$$

where $\vec{D} = \epsilon_r \epsilon_0 \vec{E}$, and ϵ_r is the relative permittivity, ϵ_0 is the permittivity of a vacuum, and $\vec{E}$ is the electric field.

Gauss's law for magnetism

The second equation states that the net magnetic flux through a closed surface is zero

$$\nabla \cdot \vec{B} = 0, \tag{2.7}$$

where the magnetic flux density, $\vec{B}$ and the magnetic field, $\vec{H}$ are related by $\vec{B} = \mu_r \mu_0 \vec{H}$, with μ_r and μ_0 being the relative permeability and the permeability of free space respectively.

Faraday's law of induction

The third equation relates the electric and magnetic fields. It states that the curl of the electric field is proportional to the rate of change of the magnetic field, such that

$$\nabla \times \vec{E} = -\frac{\partial \vec{B}}{\partial t}. \tag{2.8}$$

More simply, Equation 2.8 shows that if there is a time-varying electric field, there will always be a time-varying magnetic field.

Ampere's law for magnetostatics

Finally, there is the fourth equation, Ampere's law, which was explored in its integral form in Section 2.1.1.1.

Here the equation is written in its differential form as

$$\nabla \times \vec{H} = \vec{J} + \frac{\partial \vec{D}}{\partial t}, \tag{2.9}$$

where the current density, $\vec{J} = \sigma \vec{E}$, σ is the electrical conductivity, and $\vec{D}$ is the electric displacement field.

In a source-free space, Ampere's law (Equation 2.9) can be simplified to

$$\nabla \times \vec{B} = 0. \tag{2.10}$$

For magnetic field nulling using bi-planar coils, equal and opposite magnetic field components can be generated based on the solutions to Equation 2.10.

A magnetic field, $\vec{B}$, can be decomposed into its vector field components. In Cartesian coordinates, $\vec{B}(\vec{r}) = B_x\hat{\imath} + B_y\hat{\jmath} + B_z\hat{k}$ represents the three field components at a position $\vec{r} = x\hat{\imath} + y\hat{\jmath} + z\hat{k}$.

Solving equation 2.7 and taking the divergence of $\vec{B}$ in space, the first three gradient components (or 'longitudinal terms') can be calculated. It follows that

$$\frac{\partial B_x}{\partial x} + \frac{\partial B_y}{\partial y} + \frac{\partial B_z}{\partial z} = 0 \tag{2.11}$$

Similarly, if we solve Equation 2.10 by finding the curl of $\vec{B}$ then we reach the condition that

$$\left(\frac{\partial B_z}{\partial y} - \frac{\partial B_y}{\partial z}\right) = \left(\frac{\partial B_z}{\partial x} - \frac{\partial B_x}{\partial z}\right) = \left(\frac{\partial B_y}{\partial x} - \frac{\partial B_x}{\partial y}\right) = 0, \tag{2.12}$$

which shows the further six gradient (or 'transverse') components of the magnetic field.

The uniform and gradient field components can be used to model the magnetic field in free space. Higher order components of the magnetic field or 'harmonics' can be obtained by finding solutions to the Laplace equation. Furthermore, electromagnetic coils can be designed to produce these uniform and gradient fields, enabling very precise magnetic field control. Examples of electromagnetic coils for magnetic field control are discussed further in Section 2.2.3.1.

2.2 Magnetic Shielding

2.2.1 Types of Magnetism

Diamagnetic and paramagnetic materials have different magnetic properties and respond differently to applied magnetic fields.

In the presence of an external magnetic field, the magnetisation of a diamagnetic material is in the *opposite* direction to the applied field (Grant [1990]). In other words, diamagnets are repelled by an applied field. Conversely, paramagnetic materials become magnetised in the *same* direction as the applied magnetic field.

A 'subset' of paramagnetic materials are *ferromagnets.* Ferromagnetic materials become strongly magnetised in the presence of external magnetic fields. Unlike paramagnets, the total magnetisation of a ferromagnetic material is dependent on the strength of the applied magnetic field. The behaviour of a ferromagnetic material is also dependent on its magnetic history which gives rise to hysteresis curves (Bozorth [1951]) (see Section 2.2.2.1.2).

In the following section, the properties of ferromagnetic materials and their use in passive magnetic shielding will be discussed in more detail.

2.2.2 Passive shielding

2.2.2.1 Ferromagnetic materials

2.2.2.1.1 Magnetic domains

An important property of a ferromagnetic material is its ability to become magnetised in the presence of an external magnetic field. On a microscopic level, ferromagnetic materials are made up of *magnetic domains.* These domains are formed of atomic magnetic moments which interact locally, forming regions of aligned magnetisation enclosed by domain walls (see Figure 2.7). The domains form to minimize the energy of the material. Due to alignment of magnetic moments within the domain, each domain can be thought of as a single magnetic moment.

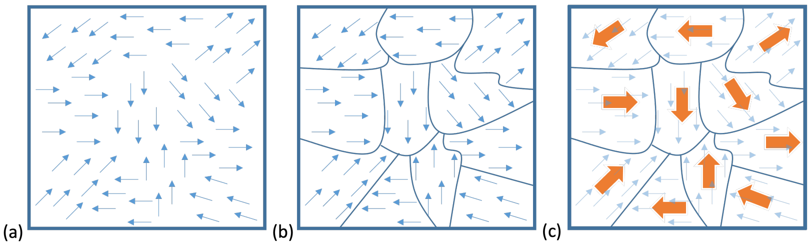

Figure 2.7: *The formation of domains in a ferromagnetic material. (a) Atomic magnetic moments (small blue arrows) interact to form regions of net magnetisation known as domains. (b) Each domain is surrounded by a domain wall (blue lines). (c) A domain can be thought of as one magnetic moment (large orange arrows).*

2.2.2.1.2 Hysteresis

In the absence of an external magnetic field, the magnetic moments are oriented within the crystal structure such that there is no net magnetisation of the sample (see point 1- Figure 2.8). If an external magnetic field, $\vec{H}$ is introduced, the magnetic moments begin to align in the direction of the magnetic field, creating a net magnetisation, $\vec{B}$. As the external field increases, more of the magnetic moments turn to align with the field, increasing the net magnetisation. If the external magnetic field is very high, all of the magnetic moments become aligned with the external field. At this point (see point 4- Figure 2.8) the sample is completely magnetised, and is described as magnetically *saturated*- no matter how much larger the applied magnetic field becomes, the magnetisation will not increase. The process of initially magnetising the material (shown via the dashed line in Figure 2.8) is irreversible, and in order to return the material to its initial state, we must apply more energy in the form of our external magnetic field, $\vec{H}$ and move the system around the hysteresis loop (shown in Figure 2.8) in order to get to zero magnetisation. The coercive field, H_c is the field needed to magnetise a magnetic material. Alternatively, $-H_c$ can be though of as the field needed to drive the magnetisation to zero.

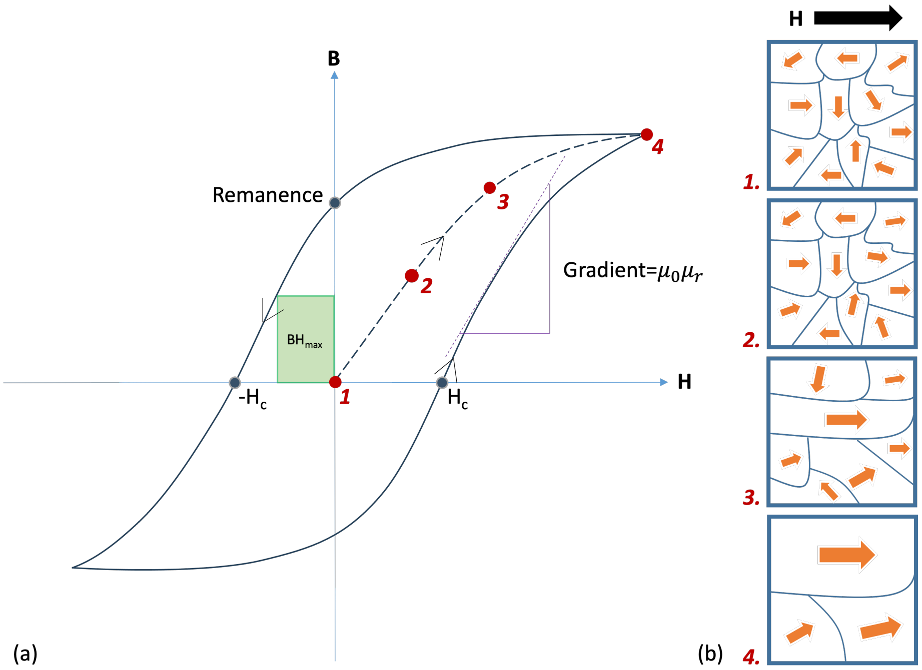

Figure 2.8: *Magnetisation of a ferromagnetic material during initial magnetisation and a subsequent hysteresis cycle. (a) Shows a hysteresis curve. The initial magnetisation is indicated by the dashed curve which starts at zero magnetisation (point 1) and reaches saturation (point 4). In order to bring the magnetisation back to zero, the material must travel around the hysteresis curve. The remaining magnetisation when no magnetic field is applied is called remanence. The coercive field,* H_c *is the field needed to bring the magnetisation to zero. The maximum energy product,* BH_{max} *is shown in the second quadrant as a green rectangle. The purple dashed line, tangential to the hysteresis curve represents the gradient at that point in the hysteresis cycle. The gradient is equal to the product of the permeability of free space and the relative magnetic permeability,* $\mu_0\mu_r$*. (b) Shows the change in the magnetic domains during the initial magnetisation. (1) The magnetic moments of the domains are randomly orientated- there is no net magnetisation of the material. (2) As the applied field,* $\vec{H}$ *increases, the magnetic moments begin to align in the direction of the field. (3) As the magnetic moments align with the applied field, the domain walls reform creating larger domains. (4) The sample is completely saturated. The magnetic moments are aligned with the applied field.*

When there is no applied magnetic field, the remaining magnetisation is referred to as the 'remanence'. The maximum energy product, BH_{max} is the largest area rectangle that can be drawn under the hysteresis curve in the second quadrant (see the green rectangle in Figure 2.8a). It is usually used as a measure of how well a magnet will perform.

2.2.2.1.3 Defining the magnetic permeability

In free space, the relationship between the magnetic field strength, $\vec{H}$ (units: Amps/metre) and the magnetic flux density, $\vec{B}$ (units: Tesla) can be written simply as

$$\vec{B} = \mu_0 \vec{H}, \tag{2.13}$$

where μ_0 is the permeability of free space (μ_0=$4\pi \times 10^{-7}$ NA^{-2}).

However, if the magnetic flux is passing through a material that becomes magnetised in the presence of a magnetic field, the total magnetic flux density is a combination of both the applied magnetic field and the magnetisation of the material, $\vec{M}$ (units: Amps/metre), such that

$$\vec{B} = \mu_0(\vec{H} + \vec{M}). \tag{2.14}$$

It is useful to define the magnetic susceptibility, χ as the ratio between $\vec{M}$ and $\vec{H}$, so that

$$\chi = \frac{\vec{M}}{\vec{H}}, \tag{2.15}$$

and hence equation 2.14 becomes

$$\vec{B} = \mu_0 \vec{H}(1 + \chi). \tag{2.16}$$

Equation 2.16 can also be written as

$$\vec{B} = \mu_0 \mu_r \vec{H}, \tag{2.17}$$

where $\mu_r = 1 + \chi$ is the relative permeability of the material, which can be thought of as a measure of how well a magnetic material is magnetised by an externally applied magnetic field.

If Equation 2.17 describes the hysteresis curve in Figure 2.8, it shows that the magnetic permeability varies as we move around the loop. Therefore we can obtain values of the magnetic permeability, μ_r by finding the gradient of the hysteresis curve (see Figure 2.8). The steeper the hysteresis loop, the higher the relative permeability.

2.2.2.1.4 MuMetal

MuMetal is the trade name of a soft ferromagnetic alloy that is commonly used to make magnetic shields. It is made up of nickel (80%), molybdenum (5%), and iron (15%). The addition of nickel increases the strength and corrosion resistance of the alloy, and molybdenum decreases eddy current losses and increases the magnetic permeability (Bozorth [1951]).

The relative magnetic permeability of MuMetal is quoted to be $\leq$ 400,000 (for DC fields) and $\leq$ 75,000 (for AC fields at 60 Hz) (Magnetic Shield Corp). A B-H curve for MuMetal (at DC fields) is shown in Figure 2.9, which shows the very high magnetic permeabilities at low magnetic field strengths.

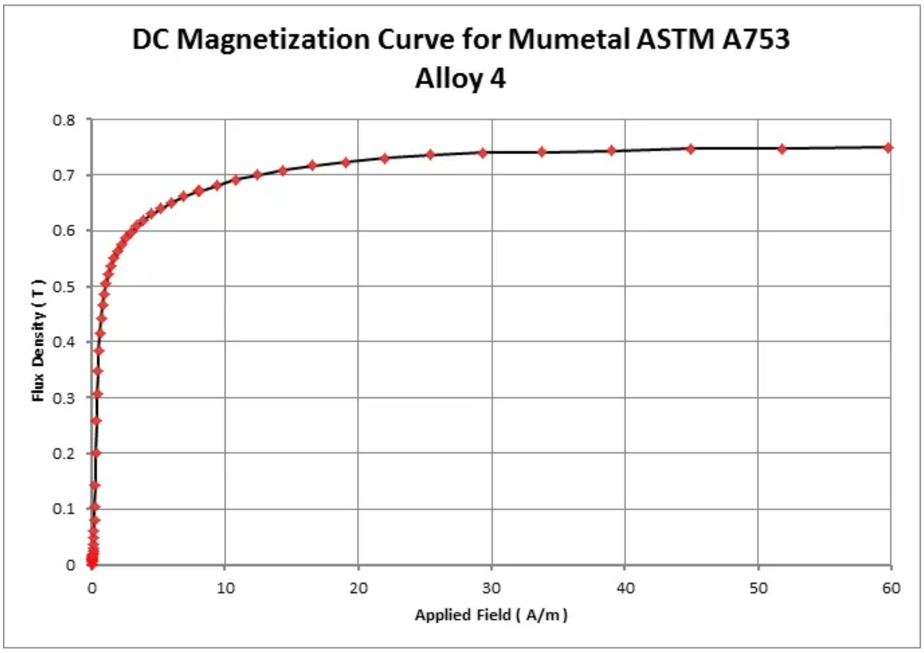

Figure 2.9: *An example of a magnetisation curve of a MuMetal alloy courtesy of Magnetic Shields Ltd (Magnetic Shields Ltd [b]).*

When the MuMetal is worked to form different shapes, such as sheets or cylinders, stress is introduced to the crystal structure which in turn causes the magnetic permeability of the alloy to decrease. The magnetic permeability of a MuMetal shield can be improved by heat treating the shield components after the alloy has been worked to change the crystal structure. The following section outlines the heat treatment process and the impact of heat treatment on the hysteresis curve.

2.2.2.1.5 Heat Treatment

After working MuMetal into its final form, the relative permeability can be improved by heat treating the alloy (see Figure 2.10b)(Bozorth [1951], Füzer et al. [2009], Arpaia et al. [2021]). Heat treatment involves heating the MuMetal in a hydrogen-rich atmosphere (Magnetic Shields Ltd [a]). The entire process consists of slowly heating the MuMetal to a very high temperature which removes any stresses in the crystalline structure. The high temperature is then held for sufficient time to allow the crystal structure to reorder and form large grains. It is the formation of larger grains within the crystal structure which increases the magnetic permeability (Hou [1996], Zhou et al. [2021]). During the temperature hold, the hydrogen-rich atmosphere reacts with impurities in the alloy, removing them from the crystal structure. Finally, the temperature is reduced slowly to allow the MuMetal to recrystallise. Figure 2.10a outlines several heat treatments and how the temperature varies over time, as well as showing the effect of heat treatment on the B-H curve.

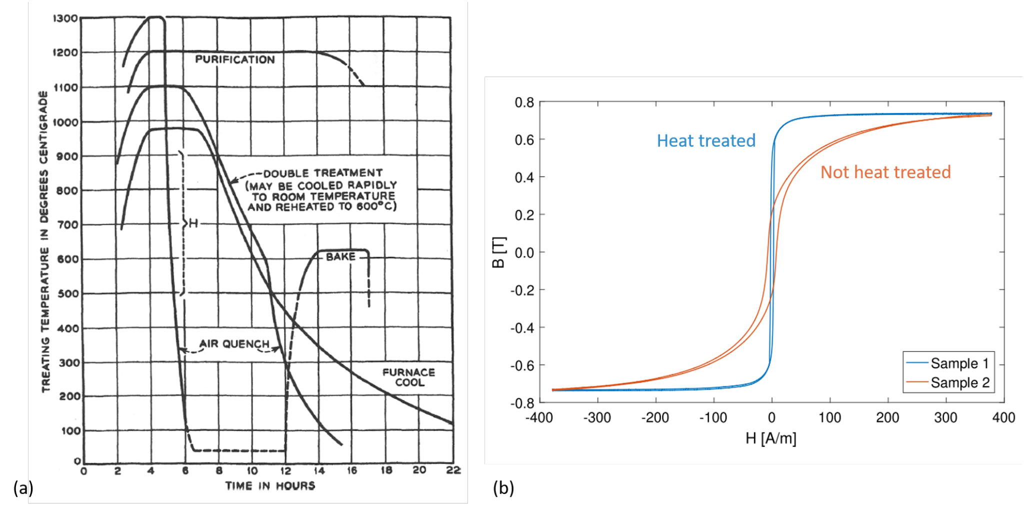

Figure 2.10: *(a) A figure taken from Bozorth [1951] showing different heat treatment protocols and how the treatment temperature is varied over time. (b) A figure taken from Arpaia et al. [2021] shows how heat treating MuMetal changes the hysteresis curve. The narrower curve for the heat treated sample (blue) indicates a higher magnetic permeability.*

2.2.2.2 Shielding factor

The ability of a magnetic shield to screen magnetic fields is called the *shielding factor* or *shielding effectiveness*, and is defined as

$$SF = \frac{|\boldsymbol{B_0}|}{|\boldsymbol{B_{shield}}|}, \tag{2.18}$$

where $\boldsymbol{B_0}$ is the measured magnetic field at a point in space without a shield, and $\boldsymbol{B_{shield}}$

is the measured magnetic field at the same point with the magnetic shield in place (Yashchuk et al. [2013]). Larger shielding factors indicate better shielding performance.

2.2.2.3 Shielding mechanisms

Static (DC) and time-varying (AC) magnetic fields interact with ferromagnetic shielding materials via two main shielding mechanisms- *flux shunting* and an *eddy current mechanism* (Celozzi et al. [2008]).

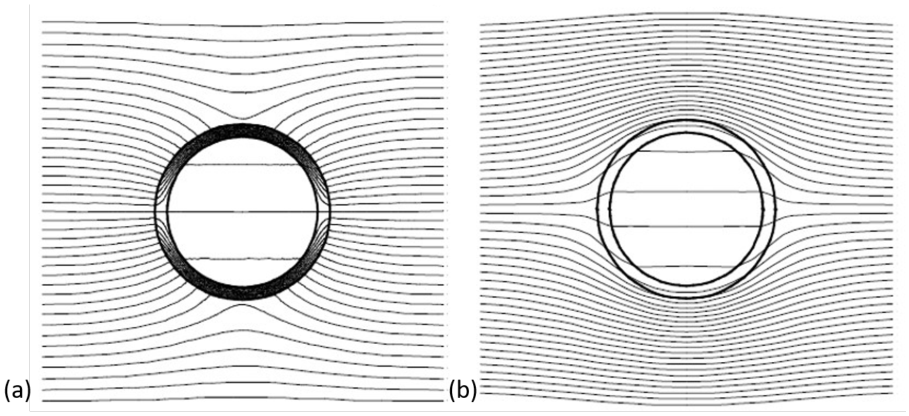

Figure 2.11: *Diagrams of magnetic flux interacting with a spherical shield via (a) flux shunting and (b) eddy current shielding. Adapted from Celozzi et al. [2008].*

2.2.2.3.1 Boundary conditions

In order to explore how magnetic fields interact with shielding materials with high magnetic permeability and conductivity, one must first understand what happens to a magnetic field at the boundary between two materials.

Both $\vec{B}$ and $\vec{H}$ can be spilt into their vector components, where B_{norm} is the component of the flux density perpendicular to the boundary and H_{tan} is the component of the applied field parallel to the boundary.

Following Gauss's law for magnetism defined in Equation 2.7 where the net flux through a closed surface is zero, the condition can be derived that

$$B_{norm_1} = B_{norm_2}, \tag{2.19}$$

where B_{norm_1} and B_{norm_2} represent the normal components of the field to the boundary in materials 1 and 2 respectively. It follows that

$$\mu_{r_1} H_{norm_1} = \mu_{r_2} H_{norm_2}, \tag{2.20}$$

by substituting in Equation 2.17.

The boundary condition for the tangential component of $\vec{H}$ can be found using Ampere's law for magnetostatics

$$\nabla \times \vec{H} = \vec{J}, \tag{2.21}$$

where $\vec{J}$ is the current density enclosed by the field surface. Assuming that there is no surface current flowing at the boundary between the materials it can be found that

$$H_{tan_1} - H_{tan_2} = 0. \tag{2.22}$$

2.2.2.3.2 Flux shunting

Flux shunting redirects static and very low frequency (<10 Hz) magnetic fields through the bulk of the shielding material, away from the shielded region (Figure 2.11a). The shunting process occurs due to the very high magnetic permeability of the shielding material compared to air, which in turn causes the magnetic field to change direction inside the material and travel roughly parallel to the surface of the shield before being released into the air.

This phenomenon can be described by examining what happens to the magnetic field at the material boundary shown in Figure 2.12.

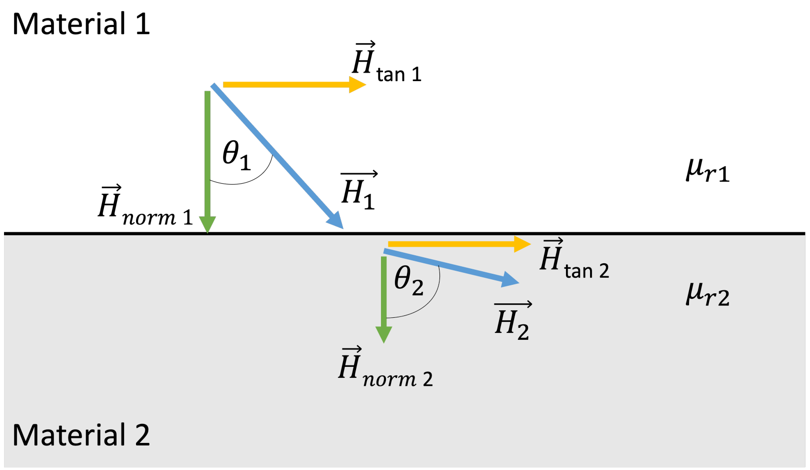

Figure 2.12: *A diagram showing how the direction of the magnetic field, $\vec{H}$ changes at the boundary between two materials of different magnetic permeabilities, μ_{r_1} and μ_{r_2}. $\vec{H}$ can be decomposed into tangential, $\vec{H}_{tan}$ and normal, $\vec{H}_{norm}$ components in each material. θ_1 is the angle of incidence of the field $\vec{H}_1$ inside Material 1 on the material boundary. After passing through material boundary into Material 2, the resulting magnetic field can be described by the vector field, $\vec{H}_2$ at an angle θ_2.*

The angle of the resulting magnetic field inside material 2, θ_2 can be written as a function of the angle of the incident magnetic field, θ_1 using the boundary conditions derived in Section 2.2.2.3.1. It follows that

$$\theta_2 = arctan\Big(\frac{\mu_{r_2}}{\mu_{r_1}} tan(\theta_1)\Big), \tag{2.23}$$

which shows that θ_2 depends not only on the angle of incidence but also the relative magnetic permeability of the materials.

If Equation 2.23 is evaluated for a magnetic field traveling in air ($\mu_{r1} = 1$) incident on a magnetic shielding material with a high magnetic permeability such as MuMetal (where $\mu_{r2} \approx 400,000$), at an angle between $0° < \theta_1 < 90°$, the magnetic field will enter the shield and be redirected at an angle of $\theta_2 \approx 90°$.

More generally, the flux will travel parallel to the surface of the shielding material if $\mu_2 \gg \mu_1$. Therefore, for flux shunting to be effective, the relative magnetic permeability needs to be high.

2.2.2.3.3 Eddy currents

The eddy current mechanism occurs in conductive materials and shields against time-varying magnetic fields. Its effectiveness and importance increases as the frequency increases.

When AC fields interact with conductive materials, eddy currents are induced as described by Faraday's law (Equation 2.8). These circulating currents produce a magnetic field which opposes the applied field (Figure 2.11b). Eddy currents decay exponentially from the surface into the bulk of the conductive material. The majority of the current flows within the skin depth, δ. The skin depth is defined as the depth at which the current density is 37% of that at the surface of the material. δ is dependent on the frequency, f and is defined as:

$$\delta = \sqrt{\frac{2}{\sigma w \mu_r \mu_0}}, \tag{2.24}$$

where $w = 2\pi f$, σ is the conductivity, and μ_0 is the permeability of free space (Celozzi et al. [2008]).

For effective AC shielding the thickness, Δ of the conductive material must be greater than the skin depth. Using equation 2.24 the skin depth for MuMetal at 60 Hz can be calculated, where the conductivity, $\sigma = 1.6 \times 10^6\ \Omega^{-1} m^{-1}$, and the relative magnetic permeability, μ_r at 60 Hz is $\leq$ 75,000, $\delta \approx 0.19$ mm. In this thesis, the thickness of the MuMetal shields range from 1 mm to 2 mm which is approximately a factor of 10 greater than skin depth at 60 Hz. At higher frequencies there is a further decrease in the skin depth.

One can see that if a ferromagnetic material has a high relative permeability and also a high conductivity, it will enable both flux shunting and eddy current mechanisms, and will consequently be a good magnetic shielding material. Additionally, layers of highly conductive material, such as copper, can be used alongside ferromagnetic materials to shield against high frequency interference fields.

2.2.2.4 Spherical shield

Shape and size play a significant role in determining the efficiency of a magnetic shield. The design of the shield must enable shunted DC flux to flow with minimal obstruction through the bulk of the material, and also allow eddy currents (induced by AC magnetic fields) to circulate freely. The following section considers how the design of a magnetic shield affects the flux shunting and eddy current mechanisms, and how these processes impact on the overall shielding factor. This will be done by looking briefly at the shielding properties of a thin spherical shell (shown in Figure 2.13).

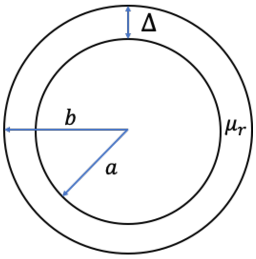

Figure 2.13: *A simple diagram showing the shell of a spherical shield with an inner radius, a and outer radius, b. The thickness of the shell is defined as* $\Delta = b - a$. *The shell has a relative permeability,* μ_r.

2.2.2.4.1 Static approximation

An approximation for the DC shielding efficiency of a spherical shell, with a diameter, d was described by Celozzi et al. [2008] to be,

$$SE = 1 + \frac{4\mu_r}{3}\frac{\Delta}{d}, \tag{2.25}$$

where $\Delta = b - a$ and $d = 2r_0$. The shell is assumed to be thin such that $r_0 \approx a \approx b$ and $\mu_r >> 1$. For DC fields, flux shunting is the shielding mechanism.

By plotting the shielding efficiency as a function of the thickness to diameter ratio, $\frac{\Delta}{d}$ for various magnitudes of the magnetic permeability, μ_r, it can be seen how the dimensions of the magnetic shield effects the performance (see Figure 2.14).

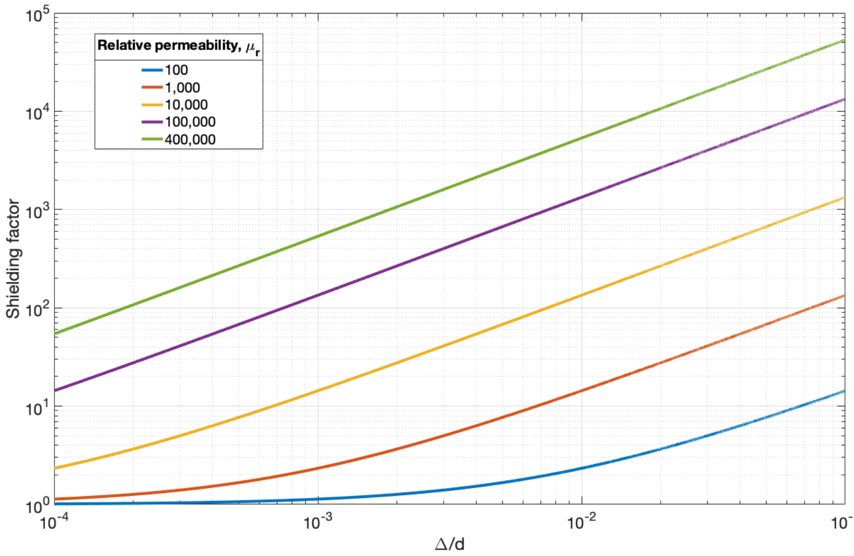

Figure 2.14: *A simulation showing the change in the shielding factor for increasing thickness to diameter ratio,* $\frac{\Delta}{d}$ *of a spherical shield. Plots for five values of relative magnetic permeability are shown, where* μ_r *= 100, 1,000, 10,000, 100,000, and 400,000. As* $\frac{\Delta}{d}$ *increases there is an increase in the shielding factor. An increase in* μ_r *also increases the shielding factor.*

Figure 2.14 shows that the shielding factor is better for a shield with a thicker shell and a small radius. As the shield gets bigger and the shell gets thinner, the shielding gets worse. Additionally, the shielding gets better as the relative permeability of the shielding material increases.

Therefore, for effective flux shunting, shields must be small with a large wall thickness.

Furthermore, Mager [1970] showed that the shielding factor can be improved by having concentric spherical shells, described by the approximation

$$SE_{total} = 1 + S_1 + S_2 + S_1 S_2 \left(1 - \frac{d_2^3}{d_1^3}\right) \tag{2.26}$$

where S_1 and S_2 are the shielding factors, and d_1 and d_2 are the diameters of the outer and inner shells respectively, and the shielding factors are calculated using

$$S_n = \frac{4\mu_r}{3d}\Delta_n. \tag{2.27}$$

Figure 2.15 shows how the shielding factor of a single layer spherical shield compares to that of a two layer shield. The two layer shield was made up of two spherical shells, separated by 10 cm, each with a relative permeability of 10,000 and a thickness 2 mm. The diameter of the outer shield, d_2 was varied from 30 cm to 10 m, and the inner diameter varied as $d_1 = d_2 - 2 \times 10$ cm.

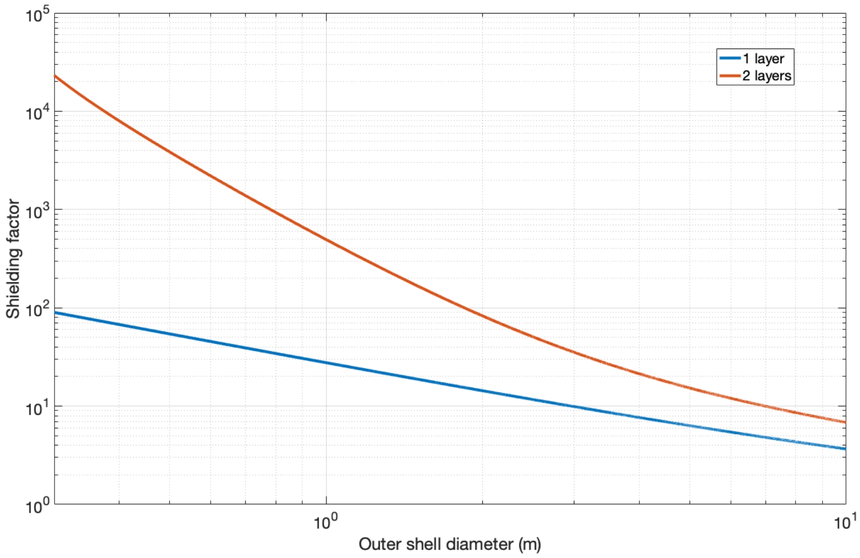

Figure 2.15: *A simulation comparing the shielding factors of a single layer (blue) and two layer spherical shield (red) with varying diameter of the outer shield between 30 cm and 10 m.* μ_r *was set to 10,000 and the distance between the two layers was fixed at 10 cm. The thickness of each shell was 2 mm.*

The simulation shows that there is a significant improvement in the shielding factor after adding a second layer, especially when the diameter of the outer layer is less than 1 m. As the outer shell diameter (and subsequently the inner shell diameter) increases, the effects of having a second layer are not as prominent.

2.2.2.4.2 High frequency approximation

A high frequency approximation where ($\Delta >> \delta$) can be made for the shielding factor of a thin spherical shell (Celozzi et al. [2008]), such that

$$SE = \frac{r_0}{3\sqrt{2}\mu_r \delta} e^{\frac{\Delta}{\delta}}, \tag{2.28}$$

where the radius of the shell is r_0, Δ is the thickness of the shell, and δ is the skin depth (as described in Equation 2.24).

Using Equation 2.28, the magnitude of the shielding factor of a conductive sphere with respect to increasing frequency of the incident magnetic field can be simulated, as shown in Figure 2.16.

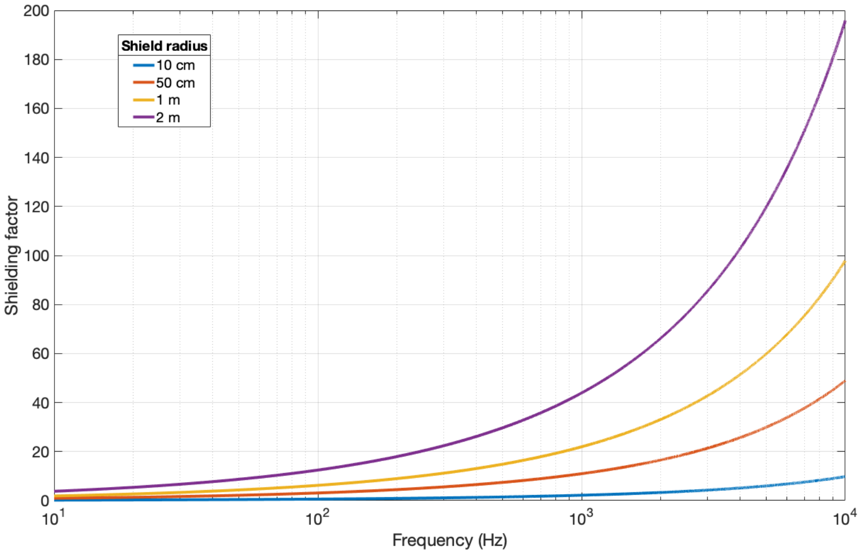

Figure 2.16: *A simulation showing how the shielding factor of a conductive spherical shield varies at high frequencies. The plots show how this relationship varies with the shield radius,* r_0 *= 10 cm (blue), 50 cm (red), 1 m (yellow), and 2 m (purple). The frequency was varied between 10 Hz and 10,000 Hz.* $\sigma = 1.6 \times 10^6\ \Omega^{-1} m^{-1}$ *(conductivity of MuMetal), and the thickness of the shield was 2 mm. The relative permeability,* $\mu_r = 1$.

As the frequency of the interference field increases, the shielding factor increases. Furthermore, as the radius of the magnetic shield increases, the shielding gets better. This is the opposite to flux shunting, where the shielding factor decreases with an increase in the radius of the shield. The increase in shielding factor with radius in the high frequency approximation can be explained due to better circulation of the eddy currents over a larger surface.

2.2.2.5 Optimising passive shields using electromagnetic coils

2.2.2.5.1 Degaussing coils

Degaussing coils are electromagnetic coils which are wound around the MuMetal and are used to reduce the remnant magnetisation of the material. Common degaussing coil configurations consist of ‘L’ shaped coils (Altarev et al. [2015b]) wound around each face of the MSR, and connected to maximise the magnetic flux driven through the shielding material (see Figure 2.17a).

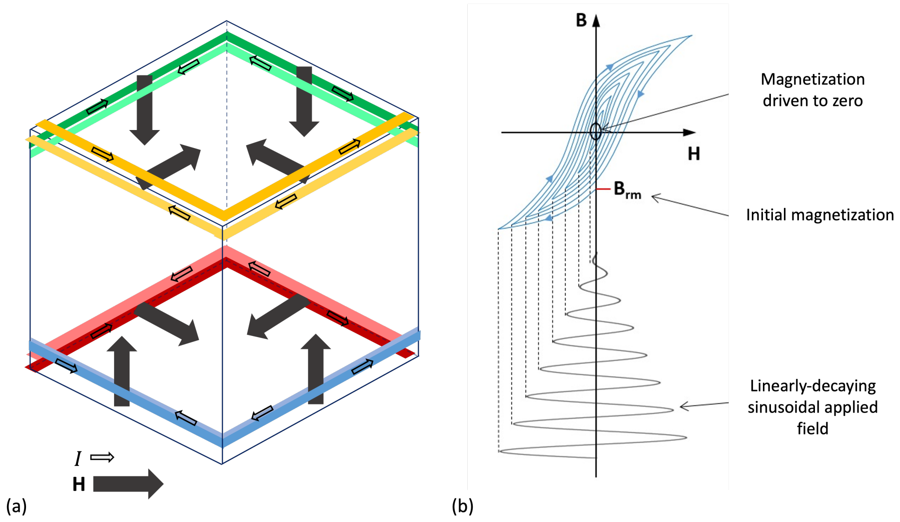

Figure 2.17: *A diagram of degaussing coils around a cubic shield. (a) A diagram showing L-shaped degaussing coils wound around a magnetic shield, where light colours show where the coil is inside the shield and dark colours are outside the shield. Small arrows show the direction of the applied degaussing current, I and large black arrows show the degaussing field, H produced by the coils. (b) A graph showing how the sinusoidal degaussing waveform applied to the coils drives the ferromagnetic shielding material about the hysteresis loop towards zero magnetisation (Adapted from Cestriom: https://cestriom.com/en/technology/demagnetization-basics/).*

Before an experiment, a sinusoidal, linearly decaying current is driven through the degaussing coils. A single cycle of the current drives the remnant magnetisation of the MuMetal once about the hysteresis loop. Repeating cycles of decreasing amplitude drives the magnetisation of the MuMetal close to zero, which in turn reduces the remnant magnetic field in the MSR (see Figure 2.17b).

2.2.2.5.2 Shaking

An uncommonly used method for increasing the shielding factor of a passive magnetic shield is shaking. Shaking involves driving a time-varying magnetic field at a constant amplitude through the shielding material during an experiment. Counter-intuitively, this action improves the shielding factor of a passive shield.

It has been suggested that shaking ferromagnetic materials improves shielding factors by narrowing the hysteresis loop and in turn increasing the effective magnetic permeability of the material (Kelhä et al. [1980]). When a shaking field is applied, the material is driven around *minor* hysteresis loops (see Figure 2.18). The narrowing of the main hysteresis loop occurs due to averaging of the minor loops. The magnetic permeability, which is the gradient of the main loop, becomes higher, which in turn increases the shielding factor.

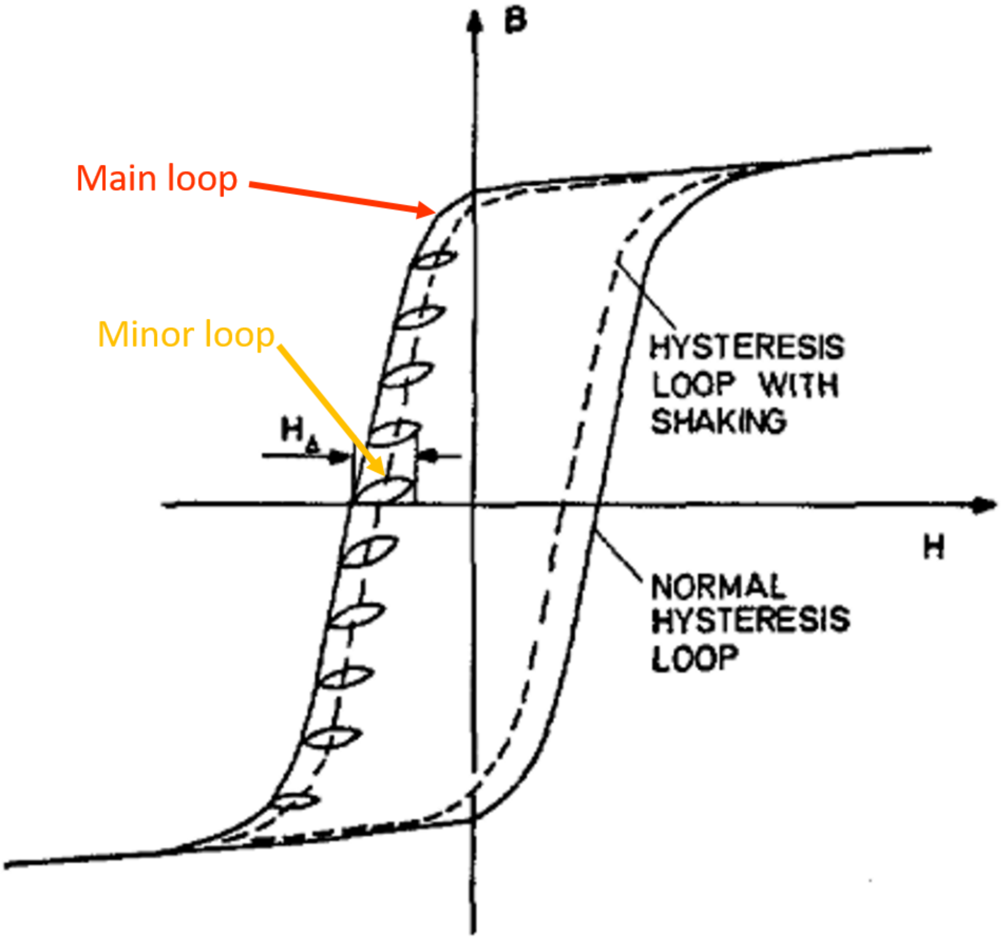

Figure 2.18: *A graph showing a hysteresis curve without shaking (solid line) and a hysteresis loop with shaking (dashed line). Shaking drives the material around the minor loops (labelled in yellow). The narrowing of the main hysteresis loop (labelled in red) is thought to occur due to averaging the effects of the minor loops. Adapted from Kelhä et al. [1980].*

Previous work carried out by Cohen [1967] showed an increase in the shielding factor of a single layer 4-79 moly-permalloy shield, at frequencies above and below the shaking frequency (60 Hz). Similar results have been shown on different shield geometries including square cylinders (Kelhä et al. [1980]) and open-ended cylinders (Sasada et al. [1988], Nagashima et al. [2002]). There does not seem to be a ‘universal’ shaking frequency, however, shaking close to mains frequencies is common in the literature.

Shaking and its application with a multi-layer shield will be discussed in depth in Chapter 4.

2.2.3 Active shielding

Active shielding enables the number of layers of a passive shield to be reduced while still obtaining DC shielding factors similar to those with more layers (Holmes et al. [2023b]). Common active shielding techniques are outlined below.

2.2.3.1 Electromagnetic coils

Active shielding, using electromagnetic coils, is often used alongside passive shielding to cancel any remnant background magnetic field or in some cases generate a known 'bias' magnetic field.

As well as Helmholtz coils (see Section 2.1.1.2.2), coils made up of distributed windings are commonly used for magnetic field control. The wire paths of distributed windings are designed using a stream function approach (Mäkinen et al. [2020]). Examples include gradient coils for magnetic resonance imaging (Hidalgo-Tobon [2010]) and also as active magnetic shielding solutions inside MuMetal cylinders (Hobson et al. [2023]). Some examples of different coil geometries are shown in Figure 2.19.

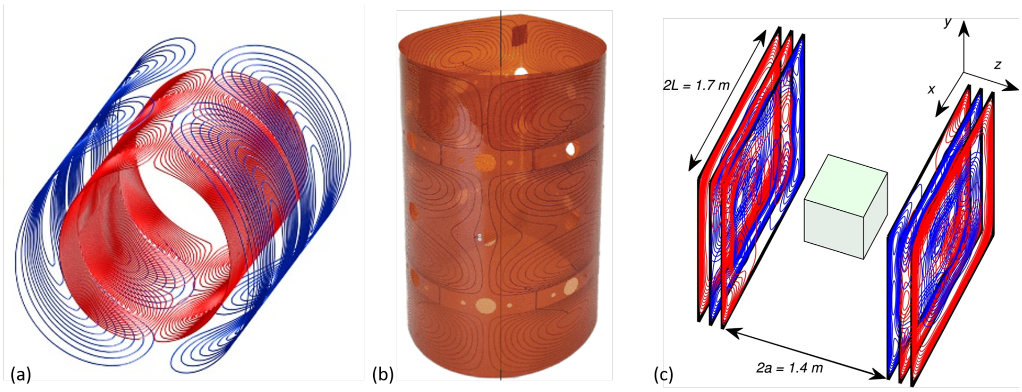

Figure 2.19: *Examples from the literature of electromagnetic coils with distributed windings. (a) A transverse gradient coil design for an ultra high field MRI scanner (taken from Winkler et al. [2018]). (b) A coil design etched onto a flexible printed circuit board for magnetic field control inside a benchtop magnetic shield (taken from Hobson et al. [2023]). (c) A biplanar coil design to control the magnetic field inside a magnetically shielded room used for magnetoencephalography with optically pumped magnetometers (taken from Holmes et al. [2019]).*

Biplanar 'fingerprint' coils can be used to cancel remnant uniform and gradient magnetic fields inside magnetically shielded rooms (Holmes et al. [2018, 2019]). The current paths are wound to produce distinct coils which generate a known field component. This includes three uniform field terms (i.e B_x, B_y, B_z) as well as magnetic field gradients shown in Equations 2.11 and 2.12. However, since the divergence and curl of the magnetic field is equal to zero, it follows that

$$\frac{\partial B_z}{\partial y} = \frac{\partial B_y}{\partial z}, \tag{2.29}$$

$$\frac{\partial B_z}{\partial x} = \frac{\partial B_x}{\partial z}, \tag{2.30}$$

$$\frac{\partial B_y}{\partial x} = \frac{\partial B_x}{\partial y}. \tag{2.31}$$

Hence six gradients can be reduced to three coils. The remaining three gradients can be reduced to two coils, where

$$2\frac{\partial B_z}{\partial z} = -\frac{\partial B_x}{\partial x} - \frac{\partial B_y}{\partial y}, \tag{2.32}$$

$$\frac{\partial B_x}{\partial x} = -\frac{\partial B_y}{\partial y}. \tag{2.33}$$

For the coils to be able to accurately null the magnetic field, the design of the coils should account for the interactions of the magnetic field produced by the coil with the ferromagnetic walls of the MSR. These have previously been modelled as perfect reflections using a method of images approach (Holmes et al. [2019], Packer et al. [2022]). A method of images assumes that charges next to a conductive plane are mirrored inside the material, creating a mirror current. The mirror current is treated as though it is in free space, it creates its own magnetic field, which is reflected back across the boundary.

It is important to understand how the coils interact with the MuMetal walls and the effect this may have on the final field produced by the coil. Chapter 3 will describe an analytical model which can be used to describe how a planar coil interacts with MuMetal.

Examples of using electromagnetic coils for field control in OPM-MEG are discussed further in Section 2.3.4.

2.2.3.2 Dynamic stabilisation and feedback controllers

The use of feedback controllers, which rely on measurements of the magnetic field to dynamically update the currents to the coils, allow real-time field control and also the cancellation of time-varying changes in the magnetic field. The controllers drive any changes in the magnetic field to a chosen set point (Afach et al. [2014]). The controllers must be uniquely tuned for each system by adjusting variables called gains. By choosing appropriate gain values a user can control how quickly the system reaches the set point, whilst ensuring that the system does not become unstable.

2.2.3.2.1 PID controller

A commonly used controller is the proportional, integral, derivative (PID) controller. A PID controller has three gain values: k_p, k_i, and k_d, which are the proportional, integral, and derivative gains respectively. The error, $e(t)$, which is the difference between the set point and a measurement of the variable you want to control, is scaled by the gain values, such that

$$u(t) = k_p e(t) + k_i \int_0^T e(t)dt + k_d \frac{d}{dt} e(t), \tag{2.34}$$

where $u(t)$ is the final scaled error which is fed back into the system. This process is outlined in Figure 2.20.

The first term is the proportional term which is the product of $e(t)$ and k_p. The second term is the integral term, which is the summation of the error terms over a time, T multiplied by the integral gain, k_i. Finally there is the derivative term, which is the derivative of the error multiplied by the derivative gain, k_d. These terms are summed to get a value, $u(t)$ which is fed back into the system.

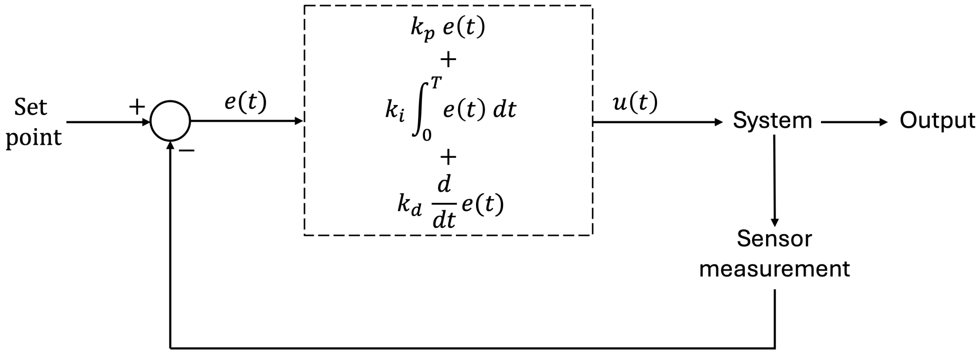

Figure 2.20: *A flow diagram of a proportional, integral, derivative (PID) controller. A set point is chosen for the system. The difference between the set point and a sensor measurement is calculated- this is known as the error,* $e(t)$*. The error is then scaled by each of the terms shown inside the dashed box. The error is multiplied by the proportional gain,* k_p*. The integral term involves summing the error term over time,* T *and multiplying by the integral gain,* k_i*. The derivative of the error is multiplied by the derivative gain,* k_p*. Each contribution is summed to get a scaled error term,* $u(t)$ *which is fed back into the system. This process repeats to try and keep the system close to the chosen set point.*

2.2.3.2.2 Proportional controller

The most simple controller, which will be used in Chapter 5, is a proportional controller (see Section 5.3). In a proportional controller the error (or change in the signal), $e(t)$ is only scaled by the proportional gain, k_p such that,

$$u(t) = k_p e(t). \tag{2.35}$$

The effectiveness of a proportional feedback controller relies on k_p being carefully tuned. If the gain is too small then the response of the system will be slow to reach the set point. If the gain is too large the system will respond quickly but will oscillate before reaching the set point. Tuning of the gains is about finding a balance between how fast the system responds and how stable the system is.

2.2.4 Magnetic shields in practice

2.2.4.1 Building magnetic shields

Whilst the spherical shell model presented in Section 2.2.2.4 is simple, the manufacture of a perfect spherical shield presents significant engineering challenges. Therefore, boxes and cylinders are more commonly used in research and industry. Manufacture of a shield using one continuous sheet of material is also not possible. Therefore, for ease of construction, the shields are made up of multiple sheets of shielding material, joined via welding at the joints or fastened with bolts. The inside of the shields are usually accessible via holes in the walls, waveguides, lids or doors. Unfortunately, the introduction of joins and holes inhibits the flow of magnetic fields and prevents eddy currents circulating throughout the shielding material.

Special consideration needs to be taken when adding access points, like waveguides and doors, into the magnetic shield to prevent sources of interference leakage. Magnetically shielded rooms typically have copper contacts around the edges of the door which aim to create good electrical contact between the door and the shielding material around the door when it is shut. This improves the flow of eddy currents across the boundary of the material and aims to improve the AC shielding. Waveguides, which are used to feed cables into the shield (sensor cables for instance), are usually made up of arrays of smaller holes so there is not one large single opening into the shield. The holes can be lined with copper, and any waveguides that are not in use can be covered with a copper endcap to attempt to minimise the flux leakage of AC fields into the shield .

The single layer MuMetal cubic shield, that is introduced in Chapter 3, has a large MuMetal lip which ensures that there is contact between the lid and the other adjoining faces of the magnetic shield when the lid is locked into place. Endcaps can be used to reduce leakage into small cylindrical shields. The endcaps tend to have a large overlap with the main body of the shield, such as those seen in the three layer MuMetal cylindrical shield in Chapter 4. The overlap ensures that there is good contact to improve flux shunting and stop leakage into the shield.

Building passive magnetic shields requires finding a balance between flux shunting and eddy current mechanisms. Magnetic shields as large as a room will require more layers to increase the shielding of static fields, but the joints in the MuMetal will inhibit the circulation of eddy currents, which in turn decreases the effectiveness of shielding at higher frequencies afforded by the increase in size of the shield which was demonstrated in Figure 2.16. Therefore it is common for layers of copper or aluminium to be sandwiched between MuMetal layers for better high frequency shielding (Altarev et al. [2014, 2015a]). Additionally, overlay strips can be used across the joins of the conductive layer to improve the flow of eddy currents (Cohen et al. [2002]).

2.2.4.2 Modelling shields

Modelling real magnetic shields is not as simple as modelling geometries such as spheres. Finding analytical solutions to Maxwell's equations for rooms and boxes is made more complex by an increasing number of boundary conditions. Consequently, numerical methods, for example, finite element methods (FEM) using software such as Ansys Maxwell (Ansys, Canonsburg, PA) and COMSOL Multiphysics (COMSOL Inc, Burlington, MA) are usually used to estimate how well a magnetic shield will perform. Whilst these methods are powerful, they require large computer processing units and very complex models. A simple analytical model of an infinite sheet is introduced in Chapter 3.

2.2.4.3 BMSR-2

The most magnetically quiet place on Earth is the Berlin Magnetic Shielded Room 2 (BMSR-2) at the Physikalisch-Technische Bundesanstalt (PTB) (Bork et al. [1980]). The BMSR-2 is a cubic shield with inner side lengths of 2.9 m. The shield is made up of seven layers of MuMetal and one layer of aluminium and is mounted on a raised gantry and a concrete foundation to reduce vibration artefacts.

The MSR is housed inside a custom built building, and an active shielding system surrounds the MSR to further compensate the Earth's magnetic field. Square coils with a side length of 11.9 m are used to null the static field along the x, y and z axes of the shield. A feedback controller is also used to actively control any changes in the background magnetic field. Degaussing coils wound around each MuMetal layer are used to remove any remnant magnetisation in the walls.

The MSR has a background magnetic field of 500 pT (Schurig [2019]) and a passive shielding factor of 75,000 at 0.01 Hz, which increases to to over 200,000 with active shielding (Bork et al. [1980]).

The BMSR-2 contains a 304 channel SQUID magnetometer array (SQUIDS are discussed in Section 2.3.2) which is used for biomagnetic measurements, fundamental physics experiments and material characterisation (Schurig [2019]).

2.2.4.4 Magnetic shielding for Magnetoencephalography

An important use of magnetic shielding is in Magnetoencephalography (MEG), a functional brain imaging technique where tiny magnetic fields, generated by neural activity in the brain, are measured by magnetometers placed around the head (see Section 2.3.1).

Magnetic shielding is important for MEG in order to reduce magnetic noise and redirect large background magnetic fields away from the scanning environment. This is typically done using magnetically shielded rooms made of materials with high magnetic permeability for efficient flux shunting of the background field away from the scanning region (Section 2.2.2.3.2), and also layers of highly conducting material such as copper or aluminium which shield AC fields from the mains frequencies via the eddy current mechanism (Section 2.2.2.3.3) (Hämäläinen et al. [1993]). The original MEG MSR at the Sir Peter Mansfield Imaging Centre (SPMIC), which houses a SQUID based MEG system (see Section 2.3.2) has two layers of MuMetal and one layer of aluminium with a background magnetic field of around 25 nT (Vacuumschmelze, Hanau, Germany). A similar magnetic shield is used for MEG at the Wellcome Centre for Human Neuroimaging at University College London (Holmes et al. [2019]).

Alongside passive magnetic shields, active magnetic shielding using electromagnetic coils is used to further control the magnetic field inside the MSR. Reference sensors inside the shielded room measure the remnant magnetic field, and by applying currents to the electromagnetic nulling coils, an equal and opposite magnetic field can be produced, cancelling the remnant field measured by the reference sensors. If the background magnetic field is changing over time, a feedback controller can be used to constantly update the currents through the coils based on real time magnetic field measurements- also known as dynamic nulling or dynamic stabilisation (Section 2.2.3.2). This technique can be used to reduce low frequency background magnetic fields which swamp the low frequency fields produced by the brain which are of interest in MEG research (Platzek et al. [1999].

Recent advances in MEG using optically pumped magnetometers (OPMs) have placed further constraints on the magnitude of the background magnetic field, which has lead to the development of highly efficient MSRs and electromagnetic nulling coils for OPM-MEG systems, which are discussed further in Section 2.3.4. This includes: the reduction of the static background magnetic field using degaussing coils (Section 2.2.2.5.1), nulling the magnetic field over the sensor array using bi-planar coils, and also the application of dynamic nulling to ensure that any drifts in the background magnetic fields do not take OPMs outside of their working dynamic range (see Section 2.3.3).

2.3 OPM-MEG

2.3.1 Magnetoencephalography

Magnetoencephalography (MEG) is a functional brain imaging technique which enables the measurement and localisation of magnetic fields arising from the simultaneous firing of neurons (Hämäläinen et al. [1993]). Not unlike electric current flowing through a wire, synaptic currents produce magnetic fields which, largely unimpeded by the conductive surface of the skull, can be detected outside of the head.

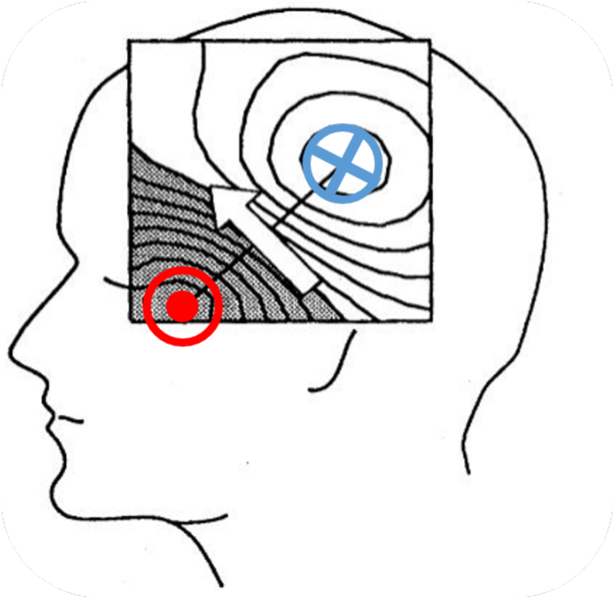

Figure 2.21: *A diagram demonstrating a magnetic field produced from a current dipole source in the brain. (adapted from Hämäläinen et al. [1993]).*

MEG has both excellent temporal (millisecond) and spatial (millimetre) resolution making it an invaluable tool in measuring and mapping brain activity (Baillet [2017]). The study of brain activity can tell us about brain function and also help clinicians and researchers to understand brain health, especially during illness. Areas of MEG research include the study of neurological conditions, such as schizophrenia (Robson et al. [2015], Gascoyne et al. [2021]), multiple sclerosis (Barratt et al. [2017]) and also the identification and localisation of epileptic activity (Ebersole [1997], Rampp et al. [2019]).

The MEG signal is of the order of 10s to 100s of femtotesla (see Figure 2.22) and the frequencies of interest to neuroscientists tend to range from 0.2 Hz to 100 Hz (although some very high frequency fields are also studied) (Baillet [2017]). The frequencies of the magnetic fields can be roughly grouped into bands- δ (0.2-3.5 Hz), θ (4-7.5 Hz), α (8-13

Hz), β (14-30 Hz), and γ (30-90 Hz) (Lopes da Silva [2013]).

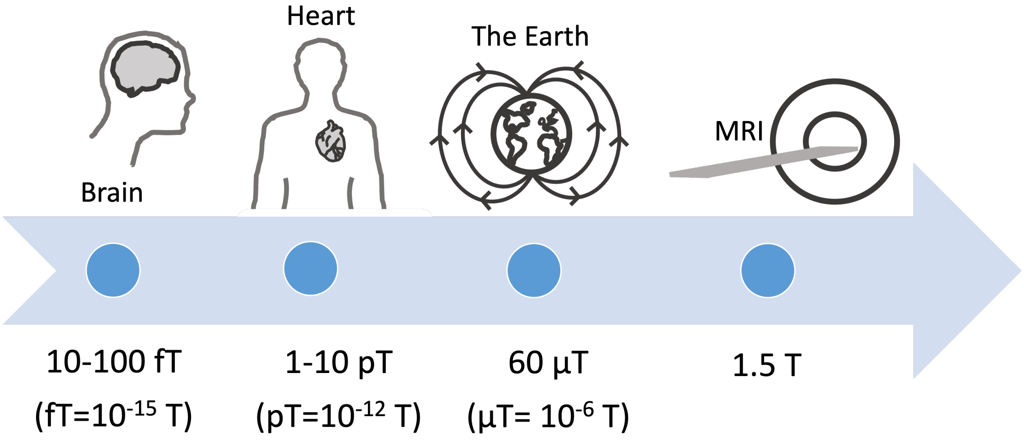

Figure 2.22: *A scale showing sources and magnitudes of magnetic fields.*

Given the small size of the magnetic fields produced by the brain, they must be detected using arrays of highly sensitive magnetometers positioned close to the head.

2.3.2 Cryogenic MEG

In a conventional MEG scanner, superconducting quantum interference devices (SQUIDs) are used to measure neural oscillations (Cohen [1972]). A SQUID is made up of a ring of superconducting material containing two Josephson junctions, which enables the measurement of a change in magnetic flux that passes through the ring (Zimmerman et al. [1970], Clarke [1974]). SQUIDS have a noise floor of ≈ 15 fT/$\sqrt{Hz}$ (Boto et al. [2018]). For the SQUIDs to remain superconducting they must be cryogenically cooled using liquid helium to a temperature of 4 Kelvin (-269 °C). Consequently, the sensor array is housed inside a large insulated dewar. A concave opening forms a fixed helmet array (see Figure 2.23), with sensors positioned several centimeters from the scalp. Participants are raised into the scanner in a seated position, or the dewar is positioned so participants can lie in a supine position. To reduce magnetic noise, the scanner is housed inside a magnetically shielded room, which is typically made up of several layers of MuMetal and a layer of conductive material for high frequency shielding (Section 2.2.4).

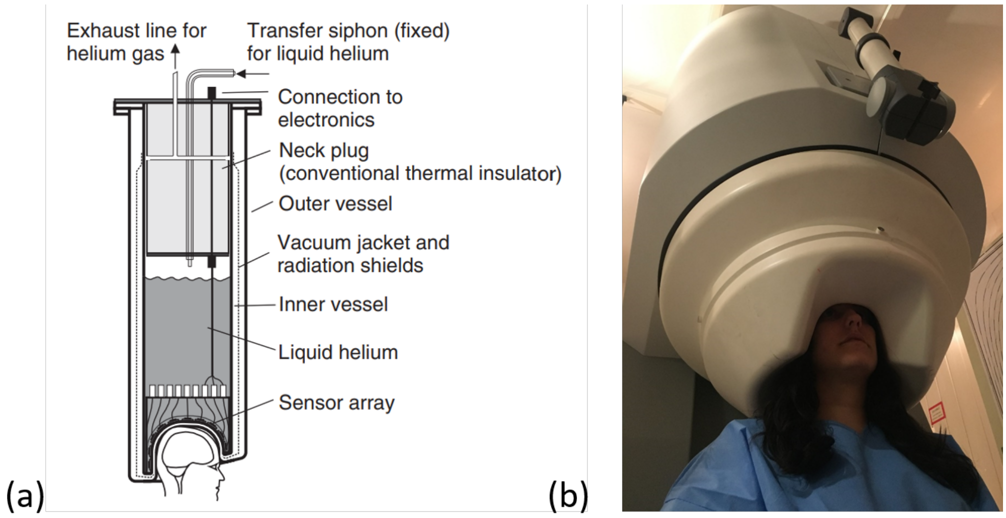

Figure 2.23: *A cryogenic SQUID-based MEG system. (a) A diagram of a cryogenic MEG system taken from Hansen et al. [2010].(b) A participant sitting inside a CTF (CTF MEG Neuro Innovations Inc., Canada) MEG scanner at the University of Nottingham.*

The 'one-size-fits-all' nature of the conventional MEG helmet means that the sensors are not always ideally positioned around the head. The signal to noise ratio will be greatly reduced for those participants with smaller heads, such as children, as the MEG signal follows an inverse square law decay with distance from the head. Furthermore, any head movement during an experiment makes it difficult to localise brain activity, so participants must remain still (with ideally less than 5 mm of movement). Constraints on movement mean that obtaining data from participants who move inside the scanner is difficult.

However, advancements in atomic magnetometers, with sensitivities comparable to SQUIDs, and also the development of precision magnetic field control using electromagnetic coils, has brought forth a new generation of magnetoencephalography scanners- wearable MEG.

2.3.3 OPM-MEG

Recently, optically pumped magnetometers (OPMs) have been used to develop MEG systems which allow the sensors to be worn directly on the scalp (Brookes et al. [2022]).

2.3.3.1 OPMs VS SQUIDs

OPMs are atomic magnetometers which can be used to measure biomagnetic fields (Tierney et al. [2019], Schofield et al. [2022]). They work by exploiting the properties of the atomic species contained in the sensor that are sensitive to magnetic fields.

Commercially available QuSpin Zero-Field OPMs (QZFM) (QuSpin Inc, Louisville, CO) have a sensitivity of < 15 fT/$\sqrt{Hz}$ (comparable to a SQUID), and have a bandwidth of 130 Hz, making them ideal sensors to detect brain activity (Boto et al. [2016]).

Unlike SQUIDs, OPMs operate close to room temperature meaning they can be placed directly on the head. The advantage of this is a larger signal strength measured by the OPMs (as shown by the contrasting heat maps in Figure 2.24) compared to an array of SQUIDs, where the sensors sit several centimetres from the head (as shown in Figure 2.24).

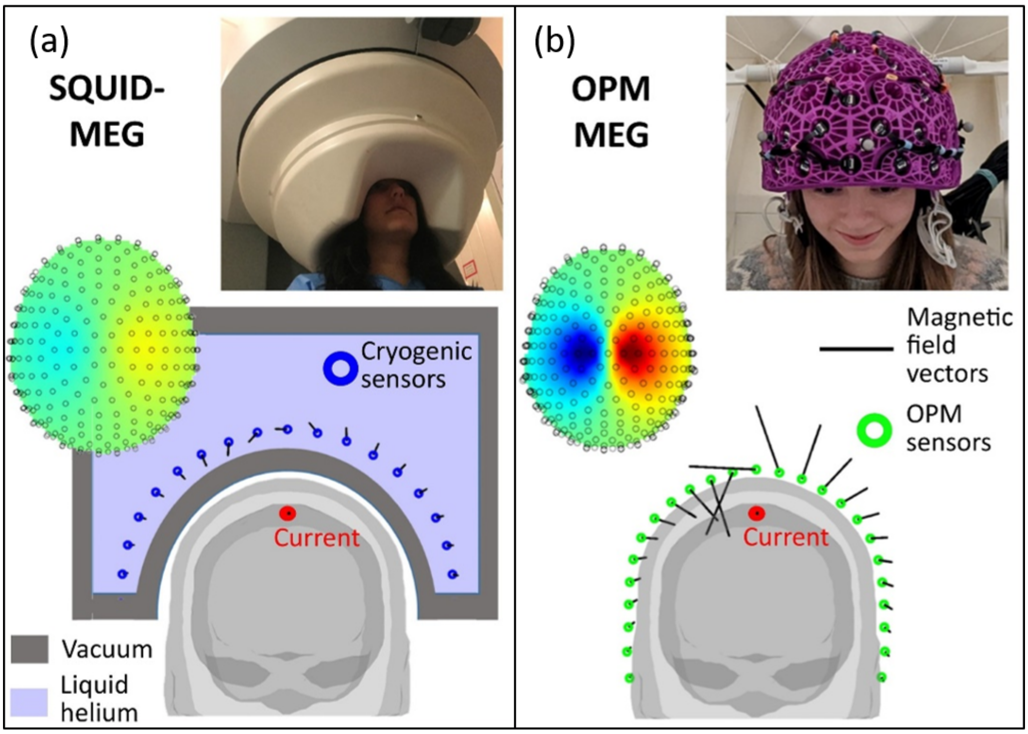

Figure 2.24: *A comparison between SQUID MEG and OPM-MEG. A simulation of the magnetic field produced by a current dipole source in the brain as measured by: (a) a cryogenic MEG system with an array of SQUIDs and (b) an array of OPMs. Taken from Brookes et al. [2022]*

The light-weight and compact size of these sensors (see Figure 2.25a) means that they can be mounted in helmets akin to a bicycle helmet or on a flexible cap, which can be made to fit different sized heads- including those of children (Hill et al. [2019], Feys et al. [2022]) and babies (Feys et al. [2023]) (see Figure 2.25). In principle, this wearability means that participants are able move their heads during a MEG recording (Boto et al. [2017, 2018].

Figure 2.25: *Photographs of an OPM and OPM-MEG helmets. (a) A QuSpin Zero-Field OPM Gen 2 (Photo courtesy of QuSpin Inc.). (b) A child-sized rigid OPM-MEG helmet (Photo courtesy of the University of Nottingham). (c) A flexible MEG cap (Photo courtesy of the University of Nottingham). (d) A baby wearing a flexible OPM-MEG cap (Taken from Feys et al. [2023]).*

Comparisons between MEG data taken using OPMs and data taken with conventional cryogenic MEG scanners show good agreement (Hill et al. [2020], Feys et al. [2022]), an example of which is shown in Figure 2.26.

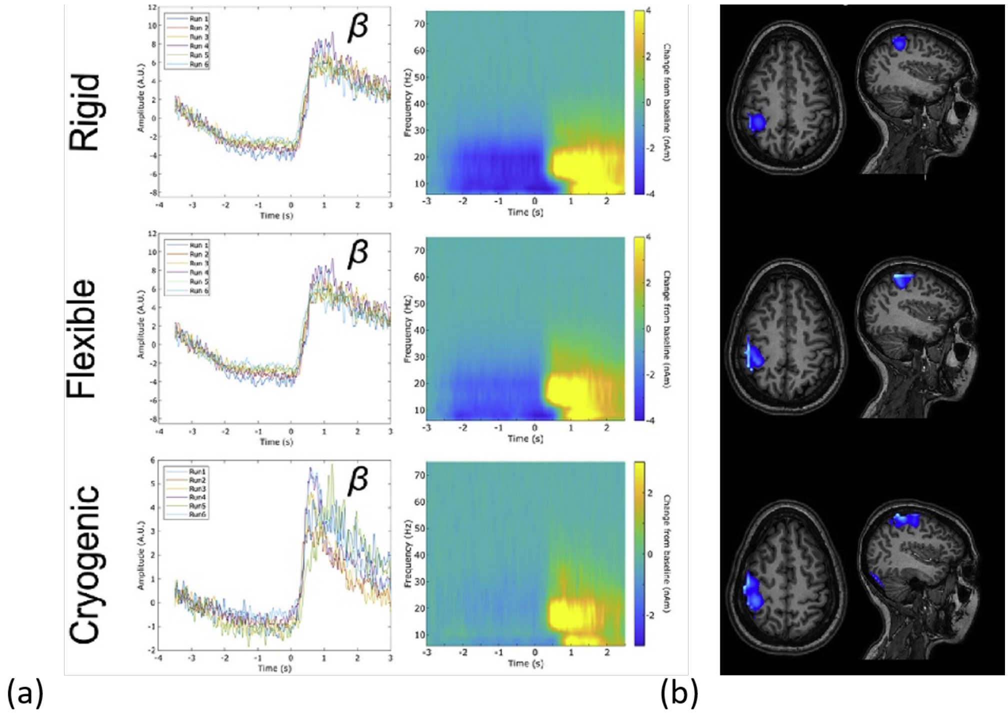

Figure 2.26: *Comparisons between MEG data collected during a visuo-motor paradigm (visual stimulus and finger abduction) using a CTF MEG system, and an OPM-MEG system with two different style helmets, a flexible cap and a rigid helmet. (a) Shows time series data (left) and time-frequency spectrograms (right) taken from the regions of peak beta modulation in the motor cortex. (b) Shows the results of source localisation of the peak beta modulation. Adapted from Hill et al. [2020].*

2.3.3.2 Zero field OPMs

Inside a QZFM is a glass vapour cell containing atoms of Rubidium-87. The spin of the atomic species means that the atoms have the potential to be sensitive to magnetic fields. However, the atoms must be carefully prepared, the process of which is outlined below.

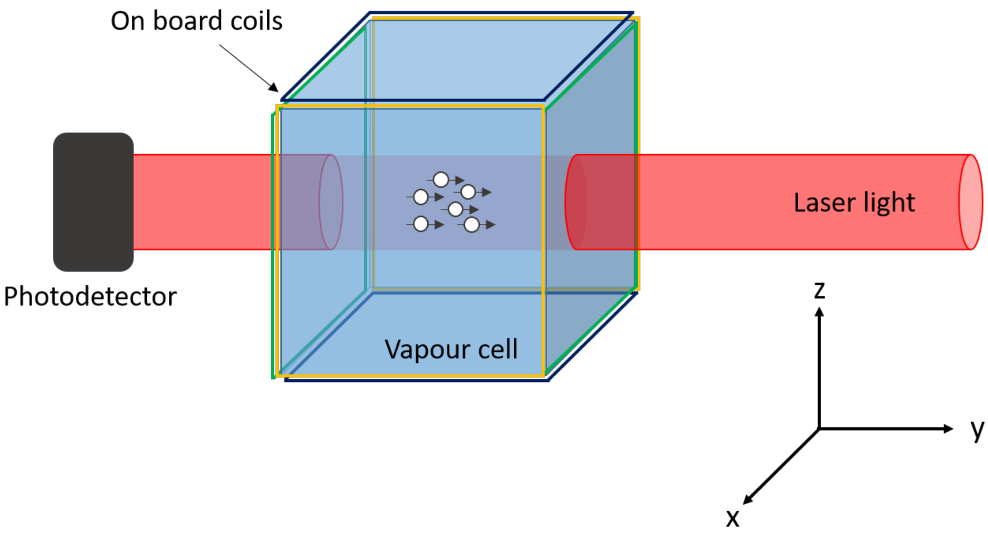

Figure 2.27: *A diagram of an optically pumped magnetometer. Inside the OPM is a glass vapour cell containing an atomic spin ensemble of Rubidium-87. Laser light (shown in red) passes through the cell and the vapour, and the intensity of the laser light is measured by a photodetector. On board coils (shown in yellow, green, and blue) are used to control the magnetic field inside the cell. Adapted from Schofield et al. [2022]*

1. The glass cell is heated, forming a vapour of Rubidium-87 atoms.
2. Currents are applied to the on-board electromagnetic coils surrounding the vapour cell (see Figure 2.27) to cancel the background magnetic field to < 1 nT. These coil currents are fixed and remain the same throughout an experiment.
3. Circularly polarised laser light (with a wavelength of 795 nm) optically pumps the Rb vapour into a magnetically sensitive state. The atoms are spin polarised in the direction of the laser light.
4. A photodetector is used to measure the amount of laser light passing through the vapour.
5. After being spin polarised, the atoms in the vapor cell are ‘transparent’ to the incoming light- meaning that the amount of laser light detected by the photodetector is at a maximum.
6. As the atoms are now in an optically pumped state and sensitive to magnetic fields, any other external sources of magnetic fields will change the spin polarisation. A change in polarisation means that more laser light is absorbed by the atomic ensemble to re-pump the atoms. This in turn reduces the amount of laser light detected by the photodetector.

7. Time-variation in transparency can be used as a sensitive magnetometer.

Figure 2.28a shows the polarisation of atoms as a function of the applied magnetic field. At 0 nT, polarisation is at a maximum. Any change in the applied field, for example, an increase in the magnetic field from the brain, causes a change in the polarisation. In order to differentiate between a positive and negative change in magnetic field, a modulation field is applied. Finally, a lock-in amplifier is used to detect the raw analogue output signal of the magnetometer, which is described by the plot shown in Figure 2.28b.

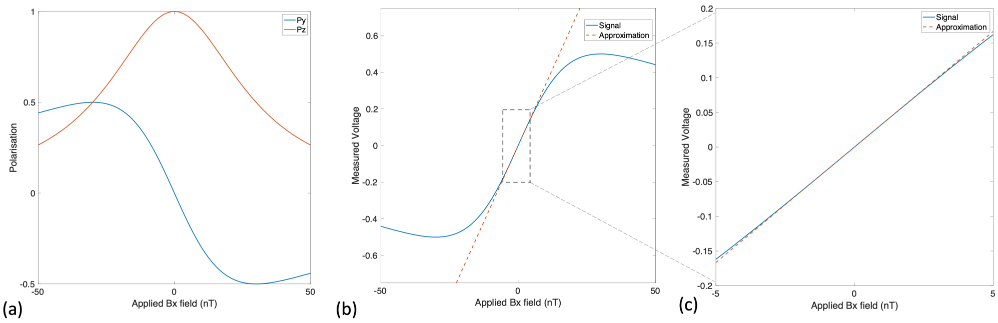

Figure 2.28: *Simulated OPM response curves. (a) The change in polarisation of Rb-87 vapour due to an applied magnetic field along the x-direction. The polarisation along the y and z-direction is shown. The circularly polarised laser beam is applied along the z-direction. The transparency depends on Pz. (b) The voltage output of an OPM for a unit of measured magnetic field (c) The approximately linear region about 0 nT is magnified.*

The dynamic range of the sensor is characterised by the approximately linear, central region of the curve (which is magnified in Figure 2.28c). For small changes in the magnetic field about zero within ±5 nT, the magnitude of the field can be calculated from the voltage recorded by the sensor using the simplified linear equation

$$V \propto \gamma T B_x, \tag{2.36}$$

where γ and T are constants which describe the atomic properties of the OPM (the derivation and explanation of such constants are beyond the scope of this thesis. For rigorous and detailed theory of optically pumped magnetometers please see Shah et al. [2007], Shah and Romalis [2009], Osborne et al. [2018]).

If the change in magnetic field experienced by the OPM is outside the ±5 nT range, then the magnetic field cannot be accurately inferred from the linear equation. Outside of this range the voltage output from the OPM can be “degenerate”, i.e. the same voltage can correspond to multiple different magnitudes of the magnetic field. Therefore, when the OPM moves outside of the ±5 nT the OPM is said to be “out of range” or has “saturated”.

OPMs can saturate during an OPM-MEG experiment due to movement through remnant magnetic fields or due to a change in the magnetic field from external sources of interference. If the sensors are to stay within their working range and measure brain activity, magnetic field control must be employed to reduce the background field and compensate for any changes in the magnetic field.

2.3.3.3 Movement artefacts

Even when magnetic field nulling is being used to keep OPMs within range, movement artefacts still occur. These artefacts manifest as very low frequency noise in the magnetic field data. The frequency range of movement artefacts is shown in Figure 2.29.

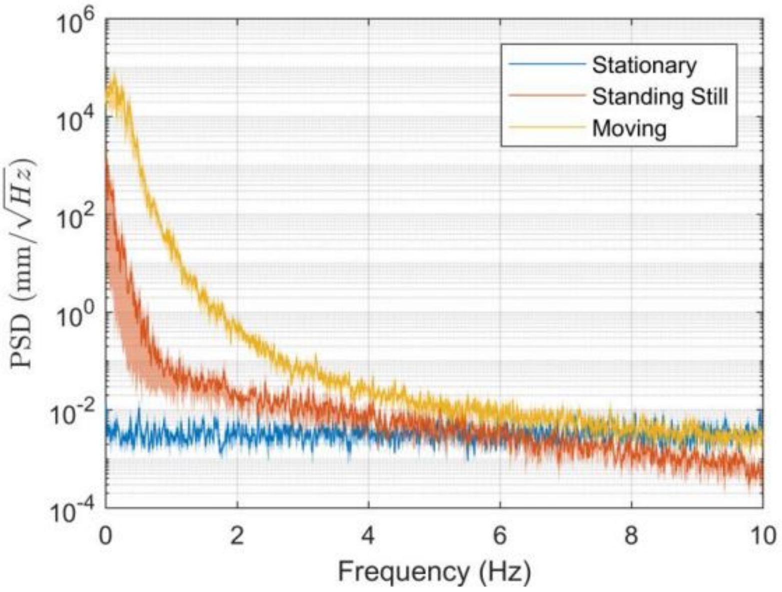

Figure 2.29: *A graph taken from Mellor et al. [2022] showing how the power spectral density of movement (measured using an optical tracking camera) changes when a person is stationary and seated (blue), standing still (red), and actively moving (yellow).*

2.3.4 Magnetic shielding for OPM-MEG

As the OPMs only work under very stringent background magnetic field requirements, the use of OPMs for MEG requires extremely efficient passive and active magnetic shielding. For a QZFM, the ambient magnetic field must be less than 50 nT, with any field changes (induced via environmental fluctuations or by head movements) within the ±5 nT dynamic range of the OPM.

2.3.4.1 Passive shielding

To achieve these low background magnetic fields, all scanning is carried out inside a multi-layer magnetically shielded room (MSR). The MSR, along with passive shielding enhancement such as degaussing, is used to reduce the background magnetic field to less than 50 nT.

At the University of Nottingham, the magnetically shielded room used for OPM-MEG is made up of 4 layers of MuMetal and a single layer of copper for high frequency shielding (MuRoom, Magnetic Shields Limited, Staplehurst, Kent). Additional degaussing coils, wound as ‘L’ shaped coils around the individual layers of MuMetal, are used to drive the remnant magnetisation of the MuMetal towards zero (described in Section 2.2.2.5.1). The magnetically shielded room, along with degaussing, reduces the background magnetic field to several nanoteslas (as described by Rea et al. [2021]).

2.3.4.2 Active shielding

Active magnetic shielding, via currents in electromagnetic coils, is used to cancel any remnant magnetic field inside a magnetically shielded room. Several coil designs have been previously developed to null the magnetic field over a volume surrounding an OPM helmet before an experiment takes place.

2.3.4.2.1 Biplanar fingerprint coils

A set of biplanar ‘fingerprint’ coils were used to carry out the first wearable-MEG experiments at the University of Nottingham (Boto et al. [2018]). A set of fingerprint coils, whose wire paths are designed to create specific magnetic field distributions (see Section 2.2.3.1), were used to null a 40 × 40 × 40 cm^3 volume at the centre of the coils (see Figure 2.30a).

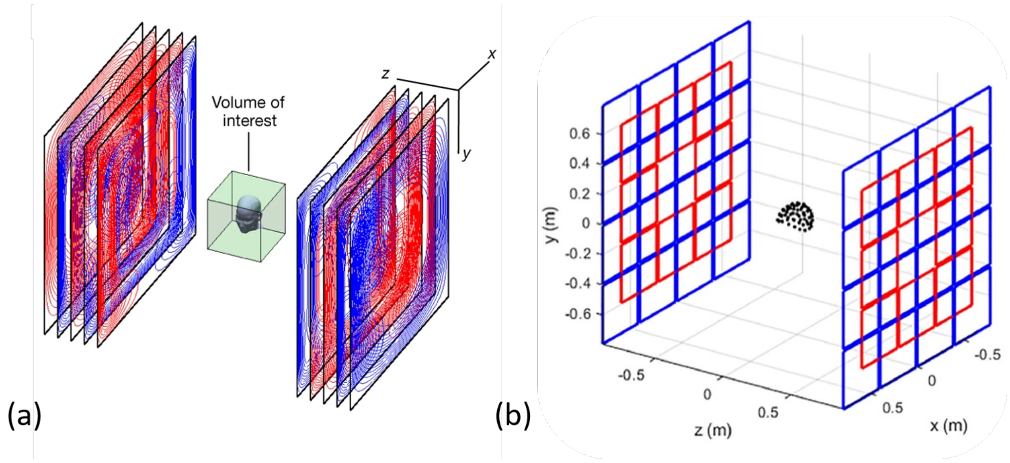

Figure 2.30: *Two different sets of biplanar coils used for OPM-MEG. (a) 'Fingerprint' coils made up of distributed windings (taken from Holmes et al. [2019]), . (b) 'Matrix' coils, which are made up of smaller independent unit coils (taken from Holmes et al. [2023a]).*

Reference sensors either side of the helmet were used to characterise the static and gradient magnetic fields across the OPM array (Holmes et al. [2018, 2019]), before currents were applied to the coils which canceled the measured field distributions before starting the experiment.

An example from Boto et al. [2018], which shows the $\frac{dB_x}{dz}$ background magnetic field distribution with and without nulling inside a MSR (two layers of MuMetal and 1 layer of aluminium), is shown in Figure 2.31.

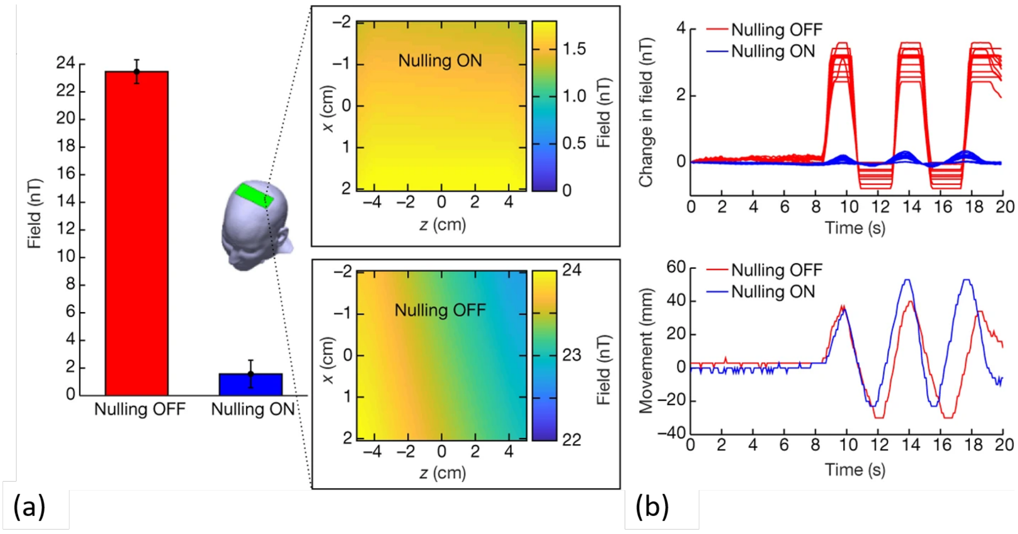

Figure 2.31: *An example of magnetic field nulling inside a magnetically shielded room using biplanar coils (adapted from Boto et al. [2018]). (a) Shows surface maps of the change in the* $\frac{dB_x}{dz}$ *magnetic field component over the head-mounted OPMs (green highlighted region) before and after nulling. (b) Shows the measured magnetic field as the OPMs move through the magnetic field gradient, with and without nulling.*

When nulling is off and the participant moves their head, the sensor array moves through the field gradient shown in the lower surface map in Figure 2.31a. As the field gradient takes the sensor outside its dynamic range the sensor becomes saturated (as shown by the flat red sensor outputs in Figure 2.31b). When nulling is switched on, the field gradient becomes smaller. Consequently, when the participant makes the same head movements, the sensors remain within their dynamic range and do not saturate (blue sensor outputs).

This means that participants can move their head inside the nulled volume throughout a MEG experiment. However, any movement outside of this fixed volume would cause the OPMs to saturate.

Further developments by Rea et al. [2021] showed that the magnetic field could be characterised more precisely by sampling the magnetic field using pitch, roll and yaw movements of the helmet-mounted OPMs, which enabled better field nulling to < 300 pT.

2.3.4.2.2 Matrix coils

Developments in biplanar ‘matrix’ coils- made up of 48 square ‘unit’ coils that can be individually controlled - have enabled the nulled region to be moved around the space between the coils (see Figure 2.30b). This means that the participant can be scanned whilst standing up, seated on a chair, and sitting on the floor. But, as was the case when using the fingerprint coils, head movements are limited to within the ‘zero field’ volume. The matrix coils also allow two people to be scanned together using two separate arrays of OPMs (‘hyperscanning’) by altering the current distributions through the unit coils so that there are two static boxes where the field is low (Holmes et al. [2023a]). When the first matrix coil experiments were carried out, the low field regions within the magnetically shielded room were static, which meant that head movements were confined to these regions.

2.3.4.2.3 Window coils

‘Window’ coils are square shaped coils that can be built into the walls of the MSR. The coils can be placed in the floor, mounted on walls/doors and placed around waveguides. They provide more flexibility in the placement and size of the nulled region and open up the scanning environment. Window coils were used in the design of the OPM-MEG suite at Young Epilepsy as shown in Figure 2.32(Holmes et al. [2022]).

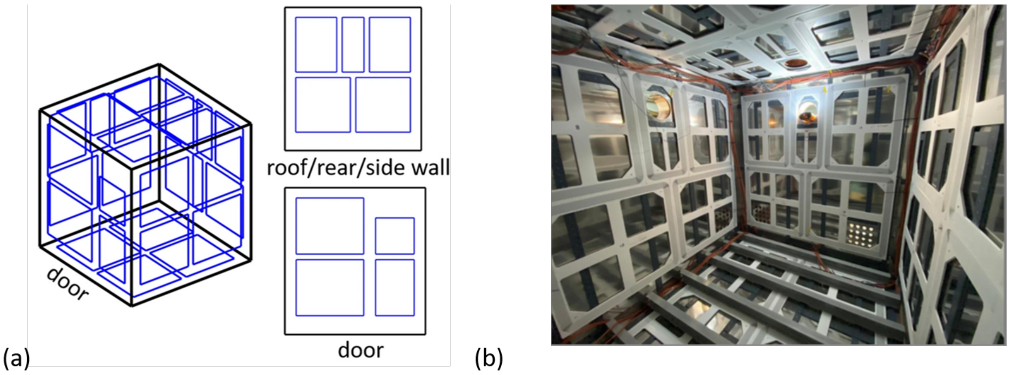

Figure 2.32: *The ‘window’ coil arrangement inside the OPM-MEG magnetically shielded room at Young Epilepsy. (a) A diagram showing the window coil configuration (taken from Holmes et al. [2022]). (b) A photograph showing the window coils inside the walls and floor of the MSR during installation (photograph courtesy of Magnetic Shields Limited).*

Like the matrix coils, whilst the placement of the nulled volume can be moved, the participant movement is restricted to the static nulled volume throughout the experiment.

Therefore to fully utilise the space afforded by wall mounted coils, a way to move the magnetically shielded volume during an experiment and allow more patient movement would be beneficial. In Chapter 5 a new method is demonstrated inside a small cubic shield which enables the continuous calibration and magnetic field nulling at the position of a moving fluxgate magnetometer.

2.3.5 Summary statement

It is clear that effective passive and active magnetic shielding is crucial for OPM operation and to detect the magnetic fields that arise from neural oscillations.

As we move towards scanning freely moving participants, electromagnetic nulling coils will need to become wall-mounted to open up the scanning environment. Furthermore, the use of window coils will also allow for flexibility in the position of the nulled region surrounding the OPM array.

However it is important that the interactions between the MuMetal walls of the MSR and the electromagnetic coils are well understood.

Techniques to enable the nulled volume to move with a freely moving participant during an OPM-MEG experiment need to be developed.

Finally, for OPM-MEG to become a more widely used brain imaging technique, lighter magnetic shields (with fewer layers of shielding material) will be needed for ease of construction and also affordability. Therefore techniques such as 'shaking' may be needed to enhance the shielding factor of lighter shields.

In the following experimental chapters these points will be investigated.

Chapter 3

MuMetal Interactions

Overview of chapter

In this chapter, the infinite plane model is introduced as a simple model to describe the interactions between a circular coil and an infinite plane of ferromagnetic material. The strength, spatial variation and the phase of the resulting magnetic field due to the presence of a material with high magnetic permeability is investigated. Furthermore, maps of the simulated magnetic field on the coil side of the plane are created to determine how these reflections compare to perfect reflections. Experiments to measure the interactions between a coil mounted to the inside face of a MuMetal box are described, and the results of these measurements are compared to infinite plane simulations.

3.1 Introduction

Electromagnetic coils are used to control the magnetic field inside magnetically shielded rooms in order to measure biomagnetic fields using optically pumped magnetometers. These coils are sometimes mounted onto the walls of the MSR to open up space inside the room (see Section 2.3.4). Therefore it is important to understand interactions between the magnetic fields produced by the coils and the ferromagnetic walls of the MSR. Previous work by Holmes et al. [2019] modelled the interactions between a set of biplanar coils and the MSR walls using a method of images approach, which treats the resulting magnetic field as a reflection. However, it is not clear whether this model can be used in real systems due to the properties of the MSR walls and the frequency of the interacting fields.

In this chapter interactions between electromagnetic coils and the walls of a magnetic shield are modelled as a planar coil interacting with an infinite sheet with a high magnetic permeability and conductivity- the *infinite plane model.*

3.2 Infinite plane model

A mathematical model describing the interactions between magnetic shielding materials and magnetic fields is shown. Specifically, the shielding material is represented as an infinite plane, which interacts with magnetic fields produced by a small circular electromagnetic coil.

3.2.1 Setting up the model

A schematic diagram of the infinite plane model is shown in Figure 3.1, with a circular coil of radius, R positioned a distance, a from an infinite plane. The coil carries a current, I. The plane is infinite in both x (into the page) and y, with a finite thickness, t in the z direction, where $t = b - a$.

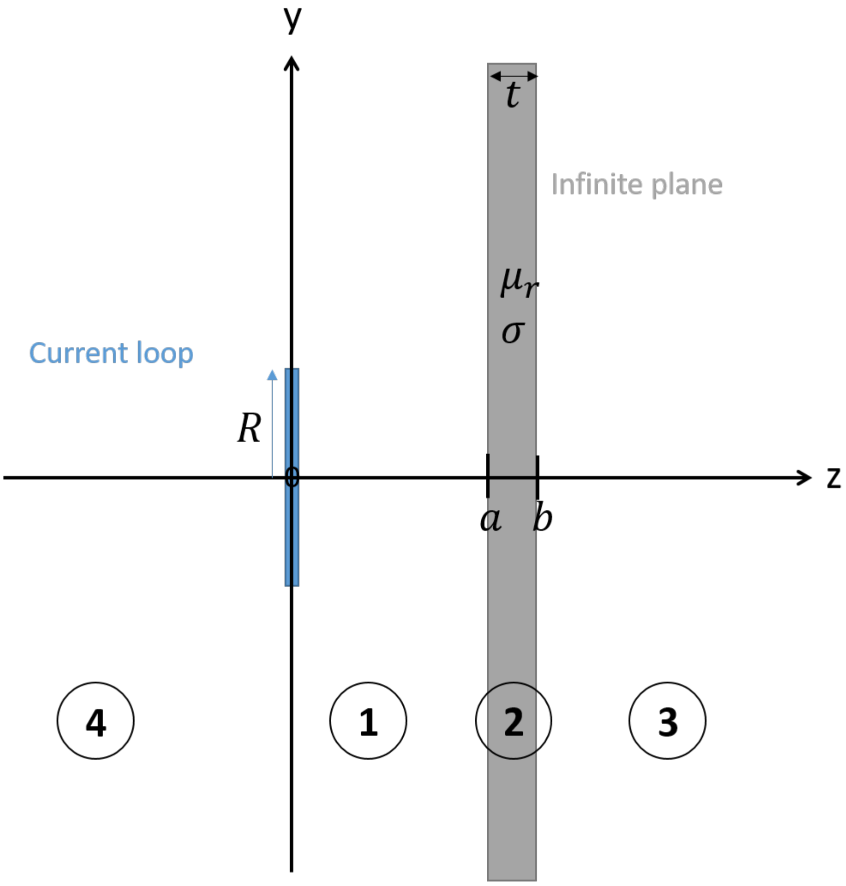

Figure 3.1: *A diagram outlining the infinite plane model. A circular coil of radius, R positioned at z=0 in the xy-plane is shown in blue. A plane, infinite in both x and y directions, but of a finite thickness, t in the z direction is shown in grey. The plane has a high relative permeability,* μ_r *and conductivity,* σ*. The coil is a distance a from the plane. Regions 1, 2, 3, and 4 are defined as* $0 < z < a$, $a < z < b$, $z > b$ *and* $z < 0$ *respectively, with b-a=t.*

The plane has a relative magnetic permeability, μ_r and an electrical conductivity, σ.

Using Maxwell's equations and setting up the boundary conditions (derived Section 2.2.2.3.1) between regions 1 and 2, and 2 and 3, the analytical solutions to the infinite plane model can be derived.

3.2.2 General solutions

One can write down the form of Maxwell's equations for each region shown in Figure 3.1; on the coil side of the plane (1 and 4), inside the plane (2), and on the opposite side of the plane to the coil (3) respectively.

In regions 1 and 3, where σ=0 and the magnetic field, $\vec{H}$ is propagating in free-space,

$$\nabla^2\vec{H} = 0. \tag{3.1}$$

In order to take into account the non-zero conductivity of the plane, the form of Maxwell's equation in region 2 can be written as

$$\nabla^2\vec{H} = \mu_r\mu_0(\sigma jw - \epsilon_r\epsilon_0 w^2)\vec{H}, \tag{3.2}$$

where w is the angular frequency of the applied magnetic field, ϵ_r is the relative permittivity of the plate, and ϵ_0 is the permittivity of free-space. μ_r is the relative permeability and μ_0 is the permeability of free space. j denotes the imaginary unit.

For magnetic shielding materials with a high conductivity such as MuMetal, it can be assumed that $\sigma >> \epsilon_r\epsilon_0 w$, at the frequencies of relevance for passive magnetic shielding in biomagnetism and hence Equation 3.2 can be simplified to

$$\nabla^2\vec{H} = \gamma^2\vec{H}, \tag{3.3}$$

where $\gamma = \frac{1+j}{\delta}$, and $\delta = \sqrt{\frac{2}{\sigma w\mu_r\mu_0}}$ is the skin depth.

Using Equation 3.1 and Equation 3.3, the general solutions for $\vec{H}$ can be found in each region (see Figure 3.1). For the purpose of this thesis only the H_z component will be shown, but both H_x and H_y are determined in a similar way.

In both regions 1 and 3, the field variation in z, H_z can be written as a Fourier series of spatial frequencies with ${k_r}^2$=${k_x}^2$+${k_y}^2$. Therefore

$$H_z(x,y,z) = H_0k_rcos(k_xx+\alpha)cos(k_yy+\beta)e^{\pm k_rz} \tag{3.4}$$

outside the high permeability sheet.

Similarly, inside the high permeability material (region 2), H_z can be written as

$$H_z(x,y,z) = H_0k_rcos(k_xx+\alpha)cos(k_yy+\beta)e^{\pm\lambda z}, \tag{3.5}$$

where $\lambda^2 = \gamma^2 + {k_r}^2$.

In order to take into account of the effects of interactions between the applied field and high permeability material on the field variation in each region, Equation 3.4 and Equation 3.5 need to be modified. It can be expected that in region 1 there will be reflections of the field due to the change in relative permeability between air and the ferromagnetic material, and hence Equation 3.4 can be rewritten as

$$H_{z1}(x, y, z) = H_0 k_r cos(k_x x + \alpha) cos(k_y y + \beta)(e^{-k_r z} + A e^{k_r z}). \tag{3.6}$$

In Equation 3.6, $e^{-k_r z}$ characterizes the decay of the applied field in the z direction away from the wall and the proceeding term, $Ae^{k_r z}$ characterizes the field variation due to the interaction with the plane. Here A is the reflection coefficient and describes the fraction of the field that is reflected from the plane. Hence when $A = 1$ the reflections are described as *perfect* reflections.

Similarly, coefficients C and D are introduced to describe the field variation in region 2:

$$H_{z2}(x, y, z) = H_0 k_r cos(k_x x + \alpha) cos(k_y y + \beta)(Ce^{-\lambda z} + De^{\lambda z}). \tag{3.7}$$

And finally in region 3, the field variation can be rewritten as

$$H_{z3}(x, y, z) = H_0 k_r cos(k_x x + \alpha) cos(k_y y + \beta) E e^{-\lambda z}, \tag{3.8}$$

where E characterizes the attenuation of the magnetic field after it has passed through the sheet.

Equivalent expressions can be found for both H_x and H_y allowing one to solve for analytical expressions of A and E. This is done using the boundary conditions, $\mu_{r_1} H_{norm_1} = \mu_{r_2} H_{norm_2}$ (Equation 2.20) and $H_{tan_1} - H_{tan_2} = 0$ (Equation 2.22), and equating the field components of $\vec{H}$ that are continuous across each boundary (between 1 and 2; 2 and 3). As a result the reflection coefficient can be found,

$$A = e^{-2k_r a}\left(1 - 2\frac{\lambda}{k_r}\left(\frac{(\mu_r + \frac{\lambda}{k_r}) + (\mu_r - \frac{\lambda}{k_r})e^{-2\lambda t}}{\left(\mu_r + \frac{\lambda}{k_r}\right)^2 - \left(\mu_r - \frac{\lambda}{k_r}\right)^2 e^{-2\lambda t}}\right)\right) \tag{3.9}$$

and the attenuation coefficient,

$$E = \frac{4\frac{\lambda}{k_r}\mu_r e^{-(\lambda-k_r)t}}{\left(\mu_r+\frac{\lambda}{k_r}\right)^2-\left(\mu_r-\frac{\lambda}{k_r}\right)^2 e^{-2\lambda t}}. \tag{3.10}$$

As an aside, the coefficients A and E can be simplified at low frequency for the case of a coil next to a MuMetal plate if it is estimated that $\mu_r \sim 10^5$ and $\frac{w}{2\pi} \ll 1$ Hz, then with $\frac{\lambda}{\mu_r k_r} \ll 1$ and $\lambda t \ll 1$,

$$A = e^{-2k_r a}\left(1-\frac{2}{\mu_r k_r t}\right), \tag{3.11}$$

and

$$E = \frac{2}{\mu_r k_r t}. \tag{3.12}$$

Equation 3.11 suggests that any deviations from perfect reflections occur on the order of $\frac{1}{\mu_r k_r t}$.

3.2.3 Solutions for a circular coil

The form of the field produced by a small circular coil must be determined in order to obtain solutions specific to the problem outlined in Figure 3.1.

Transforming from Cartesian to cylindrical coordinates and weighting the values of k_r accordingly, the form of the field produced by a circular coil of radius, R carrying a current, I is found to be,

$$H_z = \frac{-IR}{2}\int_0^\infty dk_r k_r J_1(k_r R) J_0(k_r r) e^{-k_r z}, \tag{3.13}$$

and

$$H_r = \frac{-IR}{2}\int_0^\infty dk_r k_r J_1(k_r R) J_1(k_r r) e^{-k_r z}, \tag{3.14}$$

where J_1 and J_0 are Bessel functions of the first kind.

3.2.3.1 Region 1

Taking into account reflections of the field from the coil at the plane, the field in region 1 can be written as

$$B_{z1} = \frac{-\mu_0 IR}{2} \int_0^{\infty} dk_r k_r J_1(k_r R) J_0(k_r r)(e^{-k_r z} + A(k_r)e^{k_r(z-2a)}), \tag{3.15}$$

where the reflection coefficient A has been simplified to

$$A(k_r) = 1 - 2\frac{\lambda}{k_r}\left(\frac{(\mu_r + \frac{\lambda}{k_r}) + (\mu_r - \frac{\lambda}{k_r})e^{-2\lambda t}}{\left(\mu_r + \frac{\lambda}{k_r}\right)^2 - \left(\mu_r - \frac{\lambda}{k_r}\right)^2 e^{-2\lambda t}}\right). \tag{3.16}$$

The radial component of the field, B_r can be written as

$$B_{r1} = \frac{-\mu_0 IR}{2} \int_0^{\infty} dk_r k_r J_1(k_r R) J_1(k_r r)(e^{-k_r z} - A(k_r)e^{k_r(z-2a)}). \tag{3.17}$$

3.2.3.2 Region 4

Using Equations 3.15 and 3.17, the components of the magnetic field in region 4 where z$<$ 0 can be written as

$$B_{z4} = \frac{-\mu_0 IR}{2} \int_0^{\infty} dk_r k_r J_1(k_r R) J_0(k_r r)(e^{k_r z} + A(k_r)e^{k_r(z-2a)}), \tag{3.18}$$

and

$$B_{r4} = \frac{\mu_0 IR}{2} \int_0^{\infty} dk_r k_r J_1(k_r R) J_1(k_r r)(e^{k_r z} + A(k_r)e^{k_r(z-2a)}). \tag{3.19}$$

Expressions describing the attenuated field in region 3 can also be derived, but for the purpose of this thesis only the solutions on the coil side of the plate are shown, since it is the fields produced by coils located inside the MSR that are of interest.

3.3 Reflection simulations

The field variation on the coil side of the infinite plane ($z < 0$) was simulated using MATLAB (The Mathworks Inc). The aims of the simulations were to compare the simulated reflected field to a “perfect” reflection and investigate whether the reflections were frequency-dependent over the range of frequencies to be used in coil calibration and magnetic field nulling. Experimental measurements were then carried out to determine whether perfect reflections could be used to describe the interactions of a small coil mounted on the inside of a MuMetal box. The measurements were compared to the simulations.

3.3.1 Simplifying the analytical expressions

To ensure that the integral limits were independent of the coil radius, Equations 3.18 and 3.19 were rewritten as functions of the dimensionless variable, χ where $\chi= k_r R$. After applying the substitution, Equation 3.18 can be written as,

$$B_{z4} = \frac{-\mu_0 I}{2R}\int_0^\infty d\chi\chi J_1(\chi)J_0(\chi r/R)(e^{\chi z/R} + A(\chi)e^{\chi(z-2a)/R}). \tag{3.20}$$

Similarly, Equation 3.19 can be rewritten as

$$B_{r4} = \frac{\mu_0 I}{2R}\int_0^\infty d\chi\chi J_1(\chi)J_0(\chi r/R)(e^{\chi z/R} + A(\chi)e^{\chi(z-2a)/R}). \tag{3.21}$$

The reflection coefficient, A must be scaled accordingly such that

$$A(\chi) = 1 - \frac{2L}{\chi}\left(\frac{(\mu_p + \mu_n e^{-2Lt/R}}{\mu_p^2 + \mu_n^2 e^{-2Lt/R}}\right), \tag{3.22}$$

where $L = \lambda R$, $\mu_p = \mu_r + L/\chi$, and $\mu_n = \mu_r - L/\chi$.

3.3.2 Simulation parameters

The parameters for the simulations were chosen so that they could be compared to the experimental measurements described in Section 3.4.

3.3.2.1 Plane variables

The relative permeability and thickness of the plane were chosen to reflect the properties of a 1.5 mm single layer, 55 × 55 × 55 cm^3 MuMetal box (later used for experiments). Consequently, the relative permeability of the plane was scaled such that μ_r=80,000 and the thickness of the plate was set to t=1.5 mm.

The distance between the plane and the coil was set to a=0 cm (see Figure 3.1), due to the fact that the coil was mounted directly onto the MuMetal in the experimental set up.

3.3.2.2 Coil variables

The coil radius was set to R= 4.35 cm to match the radius of the coil used in the measurements. The coil was positioned at the origin (Figure 3.1). The current, I through the loop was set to 1 A and scaled by the number of turns, N which was set to 5.

3.3.2.3 Frequency

The frequency of the magnetic field, f was varied such that f= 0.1 Hz, 10 Hz, 110 Hz. These values lie within the bandwidth of a QZFM (described in Section 2.3.3).

3.3.3 Methods

Simulations of frequency-dependent reflections were carried out using Equations 3.20 and 3.21, where A was described by Equation 3.22. Simulations were implemented for 50 equally spaced z values between 0.35 cm and 17.75 cm, and 50 equally spaced r values between 0 cm and 17.40 cm. Due to symmetry, the space was sampled over one half of r and reflected across the axis of the coil to plot the magnetic field variation from the entire space. The magnetic field components B_z and B_r were calculated by summing over 10,000 equally spaced values of χ between 0 and 1,000, in calculating the integrals in Equations 3.20 and 3.21. All other variables including the thickness of the plane, t, the relative permeability of the MuMetal, μ_r, and the radius of the coil, R were set as described in Section 3.3.2. Finally, the total field, B_{tot} was calculated such that ${B_{tot}}^2 = {B_z}^2 + {B_r}^2$.

The frequency-dependent simulations were compared to simulated “perfect” reflections, i.e. when the reflection coefficient, $A = 1$. A comparison was made by calculating the ratio between B_{tot} and the total field when $A = 1$. Surface maps showing $|\frac{B_{tot}}{B_{A=1}}|$ at each frequency were plotted, where values close to 1 indicate a near-perfect reflection.

3.3.4 Results

The surface maps in Figure 3.2 show that the ratio between B_{tot} and $B_{A=1}$ is ≈1. This suggests that for low frequencies, the magnitude of a reflection can be considered to be effectively frequency-independent.

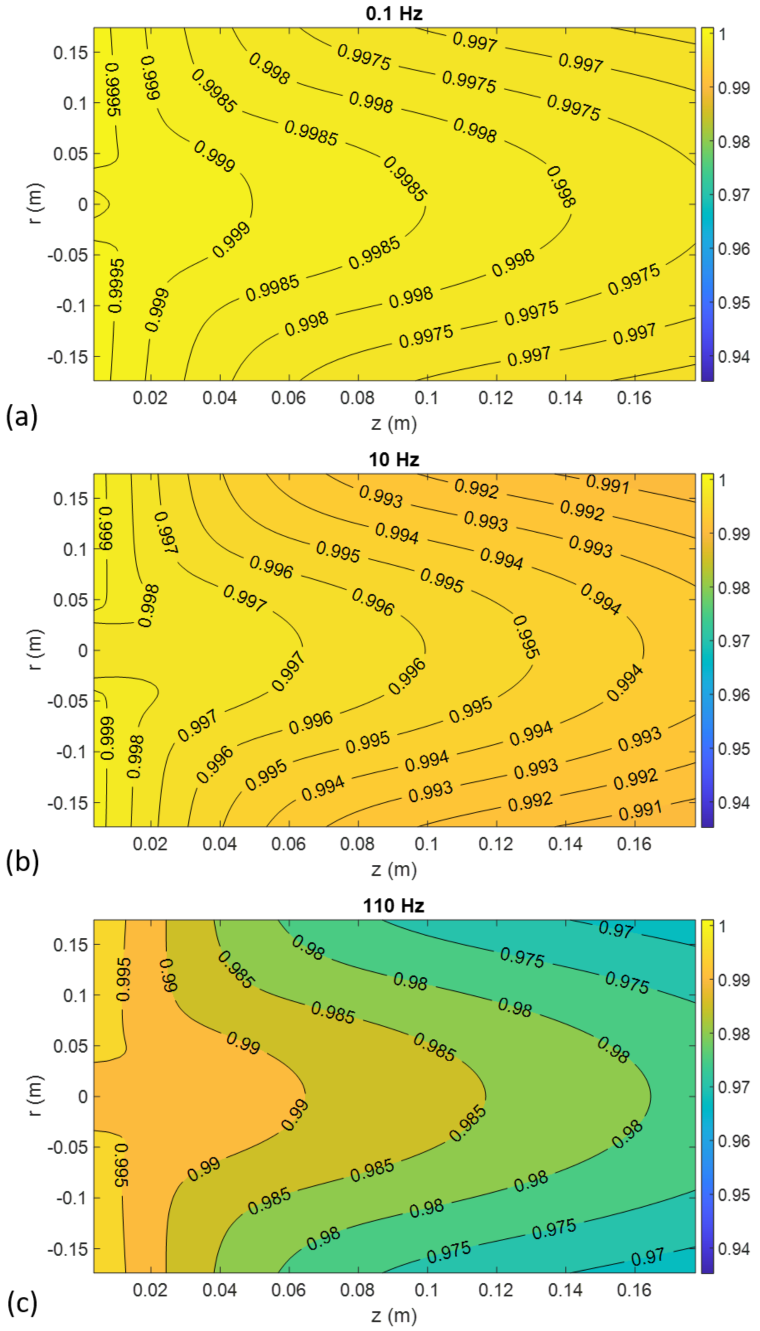

Figure 3.2: *Field maps displaying the effects of the simulated interactions between a MuMetal infinite plane and a coil of radius,* $R = 4.35\text{cm}$*, positioned at* $r = 0$*,* $z = 0$*. Each map shows the magnitude of the ratio of the frequency-dependent, total reflected field,* B_{tot} *and a perfectly reflected field,* $B_{A=1}$*. Plots at each three different frequencies are shown where: (a) 0.1 Hz, (b) 10 Hz, and (c) 110 Hz.*

Whilst the total reflected field, B_{tot} is only a fraction smaller than the perfect reflected field, B_{tot} becomes less perfect moving further away from the plate and as the frequency of the magnetic field interacting with the MuMetal plane increases.

3.4 Experimental measurements

Measurements were carried out to verify whether the infinite plane model can be used to describe how magnetic fields, produced by an electromagnetic coil, interact when the coil is mounted onto a wall inside a MuMetal box.

3.4.1 Equipment

3.4.1.1 MuMetal box

Measurements were carried out inside a single layer, 55 × 55 × 55 cm^3 MuMetal box, also known as “the MuBin”, (Magnetic Shields Ltd, Staplehurst, Kent) which is shown in Figure 3.3. The thickness of the MuMetal was 1.5 mm. The inside of the box could be accessed through the latched lid and also through a small 4 cm diameter hole at the centre of the left-hand face.

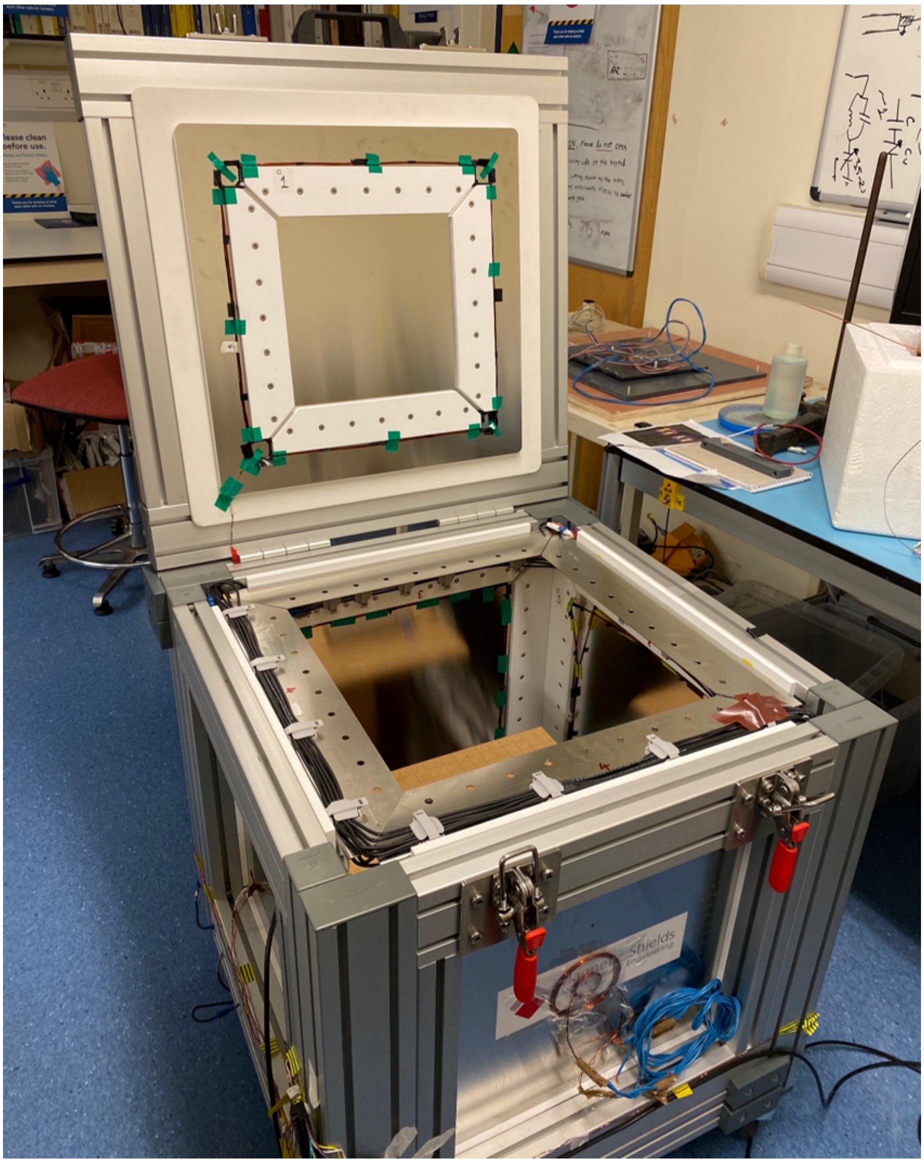

Figure 3.3: *A photograph of the "MuBin" magnetic shield. A single layer 55 × 55 × 55 cm*^{3} *MuMetal box with the lid open.*

3.4.1.2 Coil

A circular coil of radius, R= 4.35 cm (5 turns) was mounted on the inside of the MuMetal box in the centre of face 2. The coil is indicated by a yellow arrow in Figure 3.6. The coil circuit is shown in Figure 3.4. The coil waveforms were output to the coil through a NI USB 6225 Multifunction I/O Device (National Instruments (NI) Corporation, Austin, TX) interfaced with a custom NI LabVIEW program. The voltage was amplified using an amplifier made in-house. The coil was connected in series to a 10 Ω resistor. The voltage across the resistor was measured to determine the current through the coil, which was ∼ 1 mA.

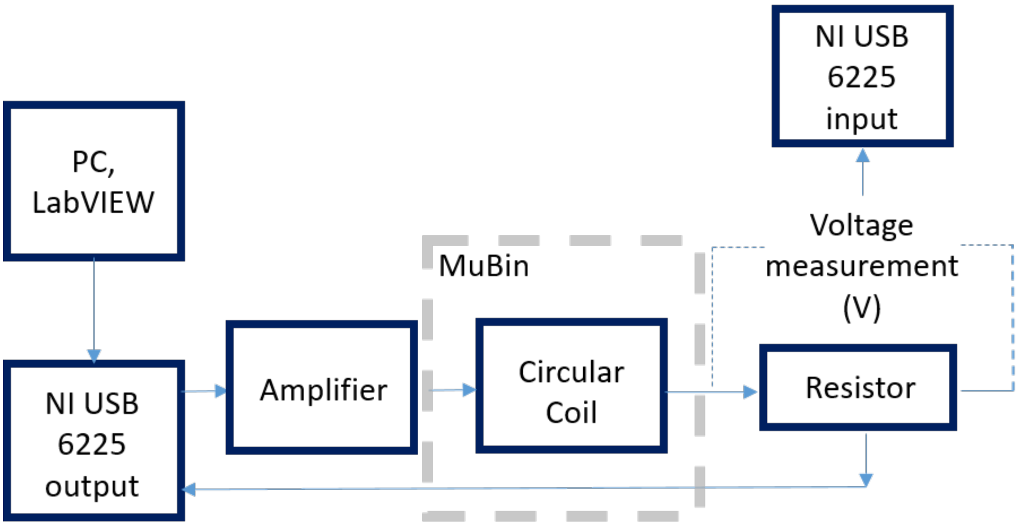

Figure 3.4: *A circuit diagram for the circular coil set-up, showing the coil inside the MuBin (indicated by the grey dashed lines). The current to the coil was output through a NI device interfaced with LabVIEW before passing through an amplifier to the coil. The voltage across an in-series resistor was measured using the same NI device in order to calculate the current in the circuit.*

3.4.1.3 Magnetic field sensor

The magnetic field components, B_x, B_y, and B_z were measured using a SENSYS FGM3D-100 (SENSYS Magnetometers and Survey Solutions, Bad Saarow, Germany) three-axis fluxgate magnetometer (see Figure 3.5). The sensor's dynamic range is ± 100 μT; the noise is 15 pT rms/$\sqrt{Hz}$ (at 0.1 Hz to 10 Hz); the bandwidth is 2 kHz; the sensitivity of the sensor is 0.1 V/μT. The sensor was positioned at the centre of the MuMetal box on a wooden board that was raised half way between the top and bottom face. The sensor measurements were recorded using the NI USB 6225.

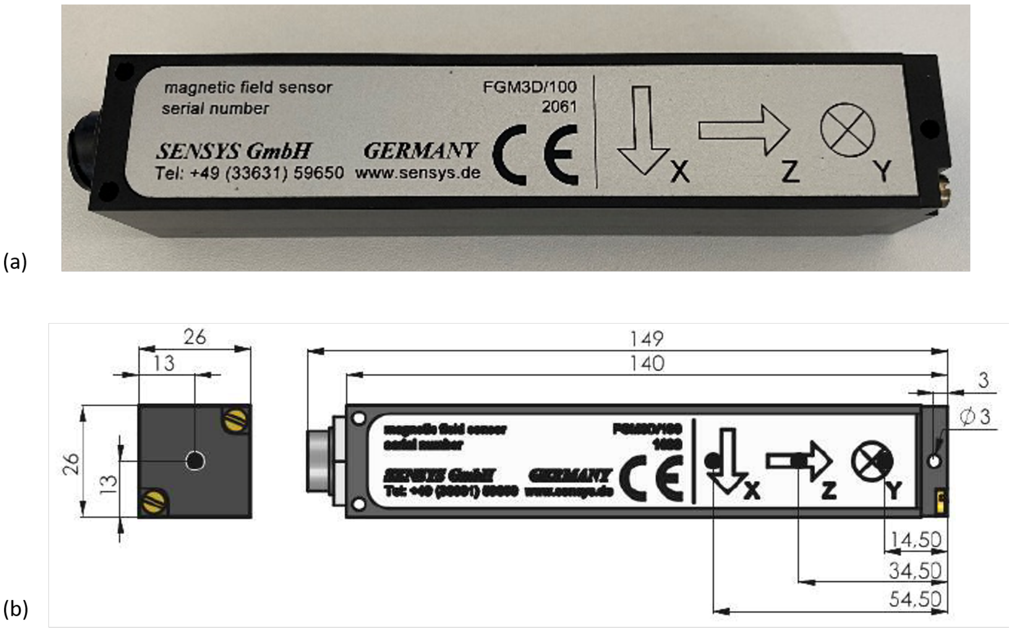

Figure 3.5: *The three-axis fluxgate magnetometer, SENSYS FGM3D-100. (a) A photograph of the sensor. The large arrows on the sensor indicate the positions of the three different FGMs which measure the x, y, and z components of the magnetic field. (b) A scale diagram (in mm) of the sensor, courtesy of SENSYS Magnetometers and Survey Solutions.*

Note that the sensitive elements of the SENSYS, B_x, B_y, and B_z, are offset from the end of the sensor by 54.50 mm, 14.50 mm, and 34.50 mm respectively, as shown in Figure 3.5.

3.4.2 Methods

A grid made up of 2×2 cm^2 squares was marked out on the wooden board and centred along the axis of the coil as shown in Figure 3.6. For reference, the grid axis r points in the radial direction of the coil (labelled from 1R to 11R) and the grid axis z is parallel to the axis of the coil (labelled A to J). Measurements were taken at the co-ordinates: 1R 2R 3R 4R 5R 6R 7R 8R 9R 10R, along each row: B, D, F, H, J. Assuming that the B_z/B_r field was symmetric/antisymmetric in r, the field was only mapped over half of the space (enclosed in the red square in Figure 3.6).

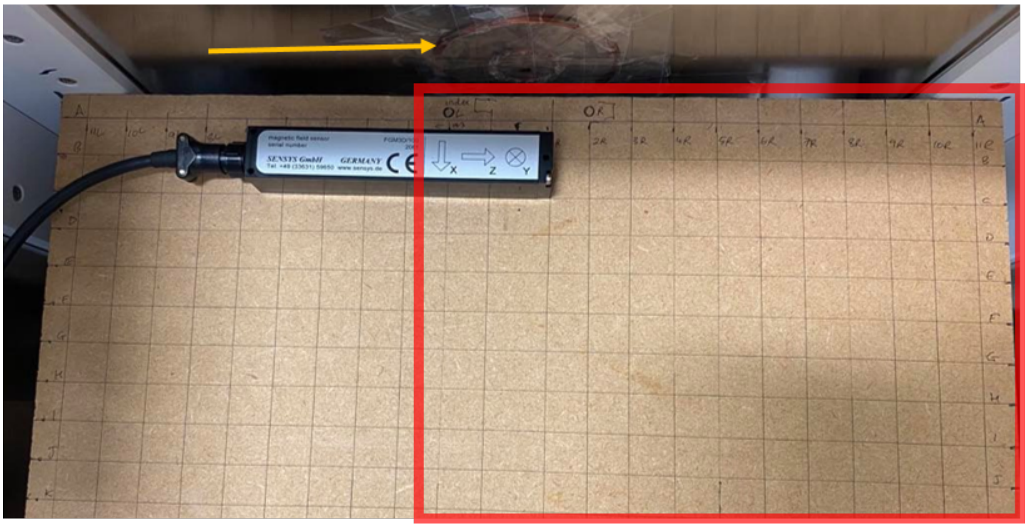

Figure 3.6: *A photograph of the grid inside the MuBin, marked with 2 × 2 cm^2 squares and labelled with a coordinate system. The grid was used to map the magnetic field inside the MuMetal box using the SENSYS magnetometer which is shown in the picture. The yellow arrow indicates the position of the coil on the inside face of the MuBin. The mapping region is indicated by the red box. The centre of the grid was aligned with the centre of the coil.*

The sensor was aligned at each position such that the bottom right corner of the SENSYS was at the desired coordinate. (For example, in Figure 3.6, the sensor is at coordinate (1R,C)).

A sinusoidal current of frequency, f was driven through the circular coil for 60 seconds and the resultant magnetic field was measured. The frequency was varied in successive experiments such that the magnetic field was mapped at $f=$ 0.1 Hz, 10 Hz, and 110 Hz to mirror the simulation study. The voltage across the in-series resistor was also measured. The sensor was then moved to the next position.

3.4.3 Analysis

The voltages recorded by the SENSYS were scaled by the gain of the sensor (0.1 V/μT) and the current through the coil was calculated using $I = \frac{V}{R}$. A Fast Fourier Transform (FFT) was taken of the magnetic field data and current data, for each frequency, at each position. The amplitude of the peak in the FFT at the frequency of interest was found and used to calculate the magnitude of the axial and radial field per unit current. Contour plots of the measured field per unit current were then compared to infinite plane simulations.

Finally the phase difference between the measured magnetic field and the current was found by taking the arctangent of the ratio between the complex value of the field and complex current at each frequency. The variation of the phase difference along a line close to the axis of the coil and along a line parallel to the coil was plotted.

3.4.4 Results

Figure 3.7 shows contour maps comparing the magnetic field per unit current to infinite plane simulations. Similarly, colour maps of the ratio between the simulations and measurements at each grid position are shown.

The measurements show good agreement with the simulations. The contour plots showing the ratio between the simulation and the measured results indicate that the measured results differ from the simulations up to a maximum of 20% for both B_z and B_r over the mapped region. There is little variation with increasing frequency, which agrees with the results of the theory shown in Figure 3.2.

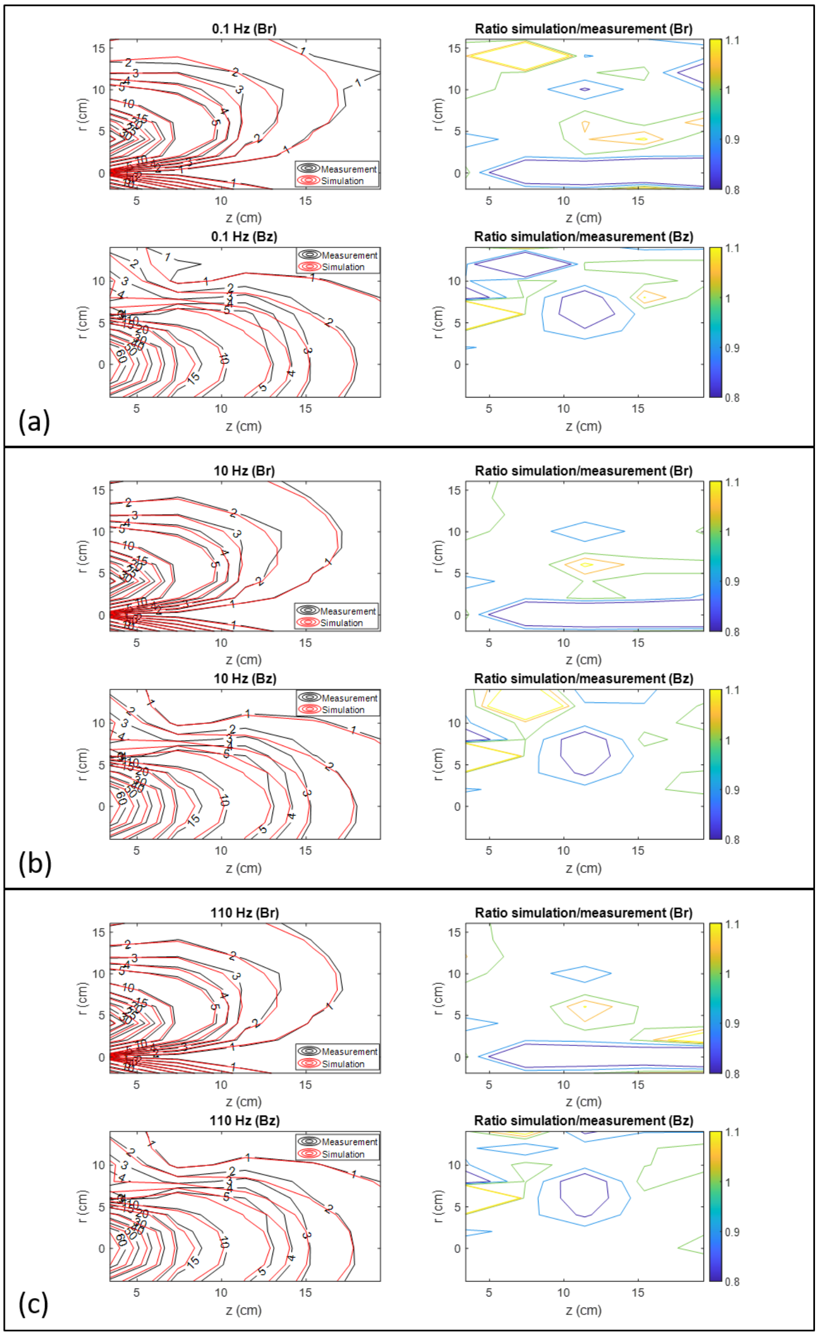

Figure 3.7: *Comparison between the measurements taken inside the MuBin and the infinite plane simulations. The B_z and B_r components of the magnetic field per unit current are shown for: (a) 0.1 Hz, (b) 10 Hz, (c) 110 Hz. Both simulation and measurement contours for B_r are plotted at 1, 2, 3, 4, 5, 10, 15, 20, 25, 30, 35, 40 $\mu T/A$; for B_z these are plotted at 1, 2, 3, 4, 5, 10, 15, 20, 30, 40, 50, 60 $\mu T/A$. The plots on the right hand side of each figure show the ratio between the simulated and measured magnetic field for both field components, B_z and B_r. These contours are plotted at 0.8, 0.9, 1, 1.05, 1.1.*

A closer inspection of the simulated and measured B_z field along a line closest to the axis of the coil is shown in Figure 3.8. The B_z field was closest to the axis of the coil when the SENSYS was positioned at the coordinates along the line 3R.

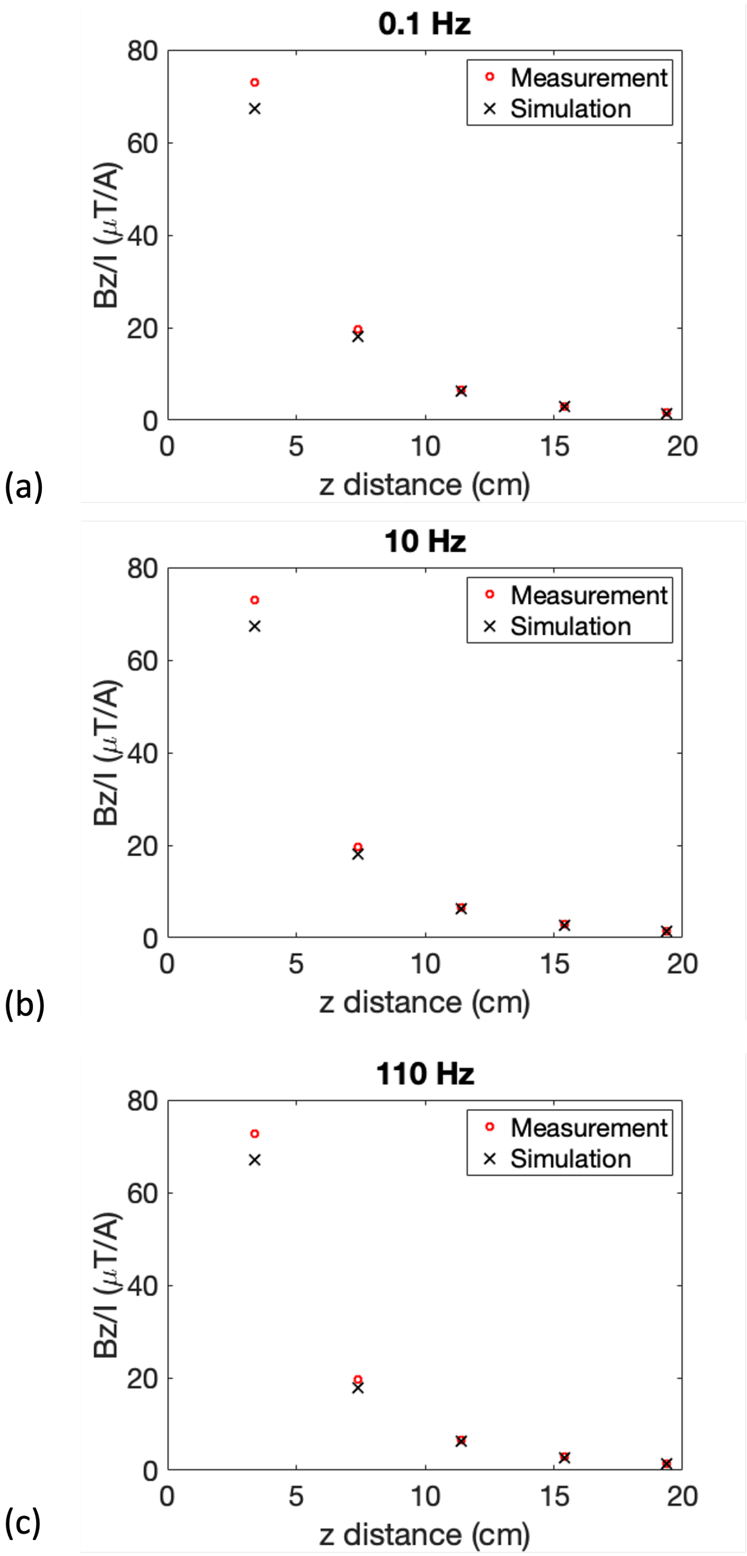

Figure 3.8: *A comparison between the measurements of a coil interacting with the walls of the MuMetal box (red) and the infinite plane simulations (black) along grid line 3R. Plots of the B_z field per unit current at: (a) 0.1 Hz, (b) 10 Hz, (c) 110 Hz are shown.*

The measured field and simulated field show good agreement. However, closer to the coil, especially at 4 cm, the difference between the measurement and the simulation is greater compared to the difference as we move further away from the coil. This could be due to the fact that closer to the coil the magnetic field is spatially decaying much faster and therefore any slight misalignment of the magnetometer will show a more significant difference between the measurement and the simulation closer to the coil. It would be interesting to capture the variation closer to the coil by sampling at smaller intervals along 3R. There is no significant variation with frequency, as expected.

The phase difference between B_z and the current through the coil is shown in Figure 3.9.

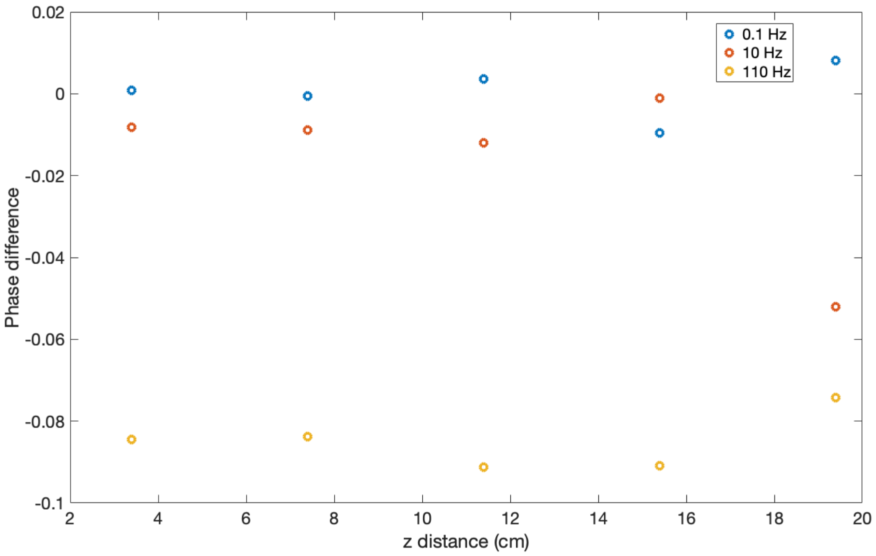

Figure 3.9: *The phase difference between the B_z field and coil current along grid line 3R at 0.1 Hz (blue), 10 Hz (red), and 110 Hz (yellow).*

The phase shows small changes with frequency which are not predicted by the theory. It is likely that these are due to the frequency response of the fluxgate magnetometer.

Plots of the magnitude of the B_r component of the field as the sensor moves along the line B, parallel to the coil, are shown in Figure 3.10.

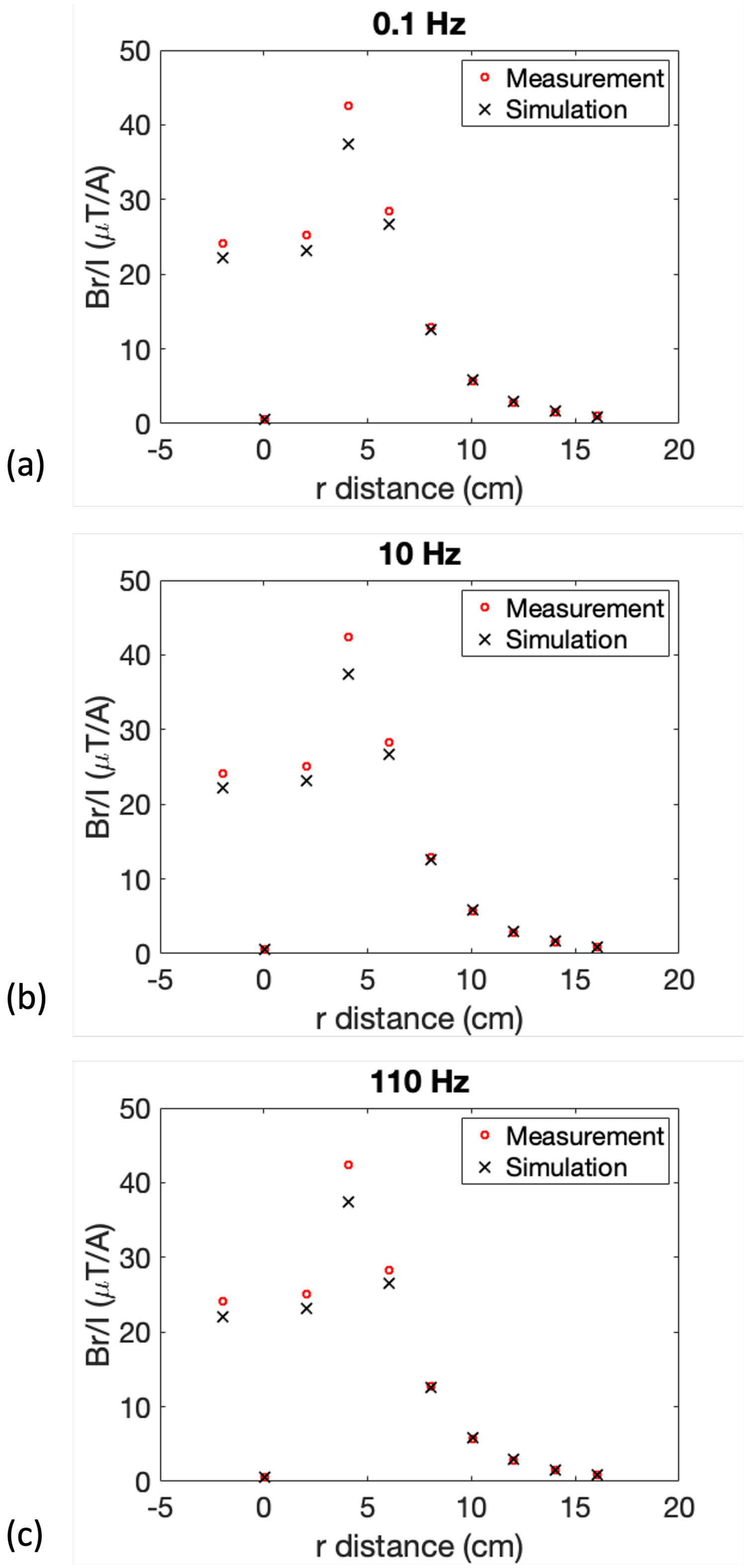

Figure 3.10: *A comparison between the measurements of a coil interacting with the walls of the MuMetal box (red) and the infinite plane simulations (black) along grid line B. Plots of the B_r field per unit current at: (a) 0.1 Hz, (b) 10 Hz, (c) 110 Hz are shown.*

The plots in Figure 3.10 show little variation with frequency and there is good agreement between the measurements and infinite plane simulation. As discussed previously, closer to the coil (r $<$ 6 cm) there is a greater difference between the measurement and the simulation compared to when r $>$ 6 cm. This may be due to not being able to accurately capture the quickly changing spatial field using the fluxgate magnetometer close to the coil.

The phase difference between B_r and the current through the coil are shown in Figure 3.11.

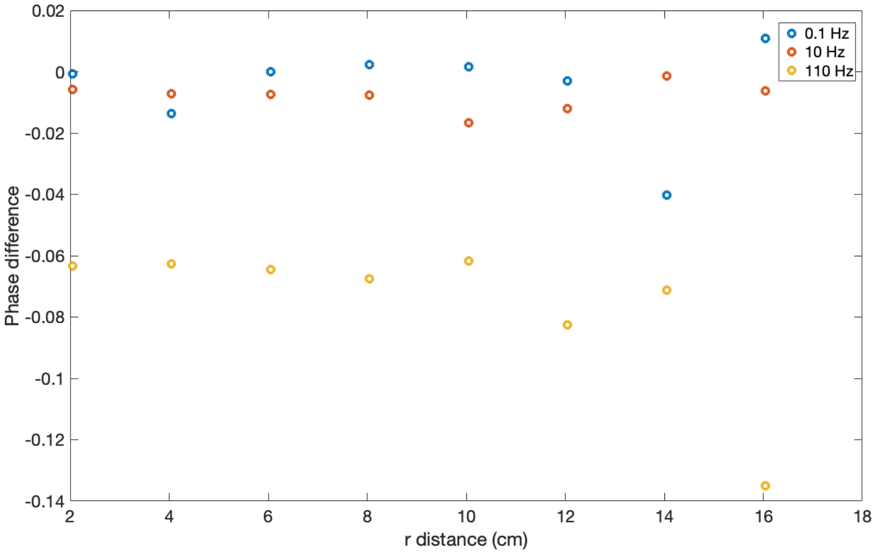

Figure 3.11: *The phase difference between the B_r field and coil current along grid line B for 0.1 Hz, 10 Hz, and 110 Hz.*

As seen in Figure 3.9, there are small variations with frequency, which are likely due to the frequency response of the sensor.

3.5 Discussion

For the frequencies shown in Figure 3.2, the reflections calculated using the infinite plane model are comparable to perfect reflections. The simulations show minimal frequency dependence, and hence it would be sensible, for the case of a coil close to an infinite plane, to reduce the reflection coefficient to $A = 1$.

Measurements inside the MuMetal box show that the interactions between a coil and the MuMetal are well described by the infinite plane model.

Perfect reflections can also be modelled using a ‘method of images’ approach. This method has been successfully used to model the interaction of coils with magnetic shields, including by Packer et al. [2020] to design coils to control magnetic fields inside a cylindrical magnetic shield with end caps, and Holmes et al. [2019], to model the resulting magnetic field of a set of bi-planar coils interacting with the MuMetal walls of a MSR.

As we move towards driving wall mounted coils with high frequency currents for continuous calibration (as explored in Chapter 5), it is important to understand how a coil will interact with MuMetal at different frequencies, and also useful to have an analytical model to describe these interactions.

3.6 Conclusions

In this chapter the infinite plane model was introduced and analytical solutions to Maxwell’s equations were shown for regions before and after the infinite plane.

Simulations of the field on the coil side of the plane showed that at frequencies up to and including 110 Hz, the interactions between a coil close to a MuMetal infinite plane could be modelled simply as reflections.

Simulations were then compared to measurements taken inside a MuMetal box. For a small coil mounted on the MuMetal and driven at 0.1 Hz, 10 Hz, and 110 Hz, the measurements showed a good match to theoretical predictions.

Chapter 4

Shaking

Overview of chapter

In this chapter, *shaking* is explored as a way to enhance the shielding factor of a MuMetal shield. Shaking involves driving a time-varying magnetic field at a constant amplitude through the shielding material during an experiment. Here the results of shaking experiments performed on a three-layer, MuMetal, cylindrical magnetic shield, are presented. Firstly, the shielding factor of the magnetic shield is found for twenty-two frequencies between 0.1 Hz and 105 Hz with the applied interference field along the axis of the magnetic shield. Then the effects of shaking on the magnetic shield are explored; first shaking the outer layer, followed by the middle layer, and then the outer and middle layer together. Effects of shaking frequency and shaking amplitude on the shielding factor are explored. The results of the investigation are presented and discussed. Finally the use of shaking as a practical shielding technique for OPM-MEG is discussed.

All experimental work in this chapter was carried out as part of an industrial placement at Magnetic Shields Limited in Kent.

4.1 Introduction

Alongside electromagnetic nulling coils (Section 2.2.3.1) and demagnetisation of the magnetic shield using ‘degaussing’ coils (Section 2.2.2.5.1), another technique that can be used to improve the shielding factor of a shield is called *shaking* (see Section 2.2.2.5.2). Shaking is the application of a time-varying magnetic field through coils (typically the degaussing coils) wound around the shielding material in such a way to drive the shaking flux through the shielding material (Kelhä et al. [1980]). Unlike degaussing which is carried out before an experiment, the shaking field is applied during an experiment.

In this chapter, shaking is applied to a three layer, MuMetal shield, formed of three nested cylinders.

4.2 Overview of experiments

Firstly, the shielding factor of the magnetic shield was determined over a range of frequencies, using a Helmholtz coil to generate the interference fields and a fluxgate magnetometer to measure the magnetic field inside the shield. Using degaussing coils wound around the length of each individual layer of the cylinder, a shaking field was applied to the MuMetal. Whilst shaking the shield, measurements of the interference field were repeated to determine if shaking improved the shielding efficiency of the shield. Different parameters were varied to see if this improved the effectiveness of shaking. Applying different shaking current amplitudes, different shaking frequencies, and also shaking single layers and a combination of multiple layers were investigated.

4.3 Equipment

4.3.1 Multi-layer magnetic shield

The shielding efficiency was found for a commercially available multi-layer magnetic shield, the Zero Gauss Chamber, with and without shaking. The magnetic shield consisted of three nested, co-axial, MuMetal cylinders (see Figure 4.1). Each cylinder had a notched endcap to allow for the easy winding of the degaussing coils around the MuMetal along the length of the cylinder. Each endcap also contained a hole to allow for sensor access. The cylinders were separated using nylon rings.

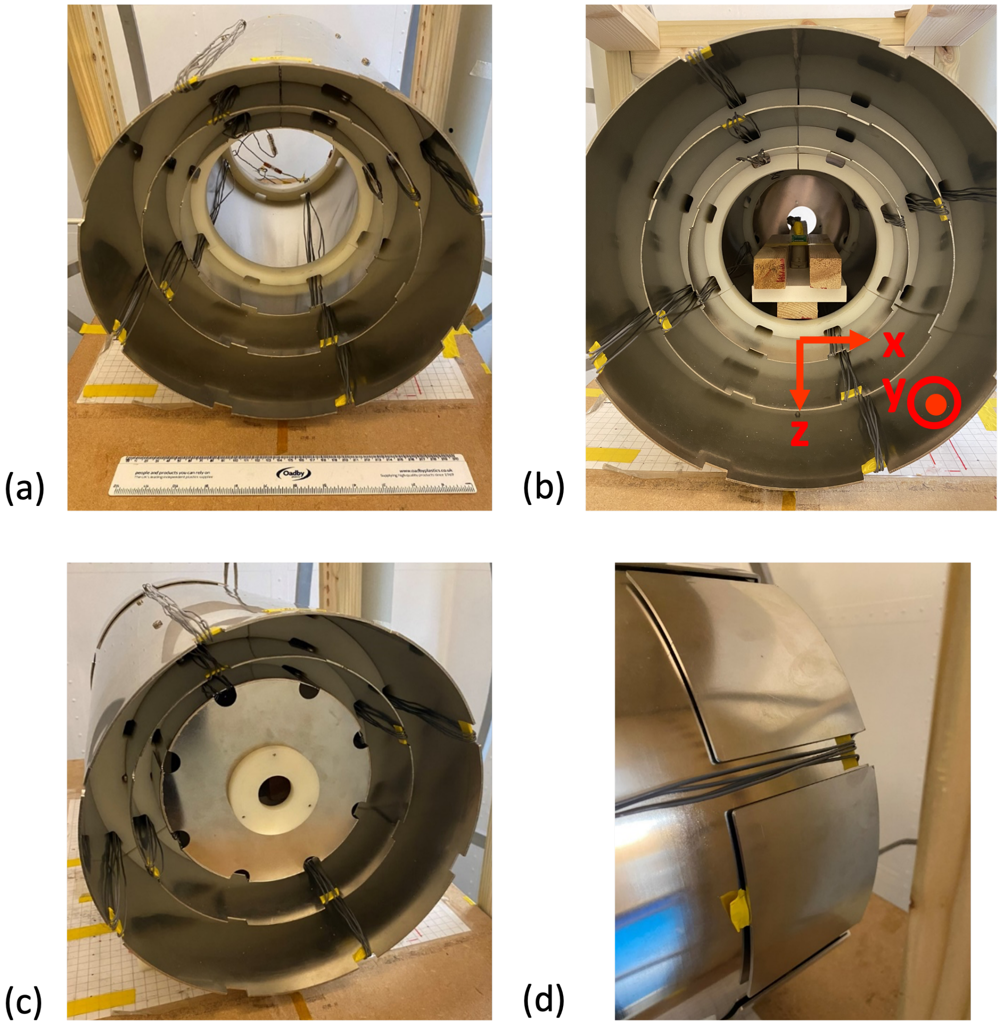

Figure 4.1: *Photographs of the Zero Gauss Chamber- a three layer, cylindrical MuMetal magnetic shield. The outer layer has a length of 580 mm and a diameter of 307 mm. The MuMetal thickness of the outer layer is 1 mm. (a) A photograph of the shield without endcaps. Degaussing coils are wrapped around the length of each of the shields. (b) A photograph of a Bartington fluxgate magnetometer in a wooden mount positioned at the centre of the shield. The sensor axes are shown in red. (c) A photograph showing one of the endcaps on the the inner layer. The notches in the end cap enable degaussing coils to be wound around the length of the cylinders. (d) A photograph showing the notches in the endcap and the overlap of the endcap with the outer layer of the shield.*

The dimensions and measurements of each layer are shown in Table 4.1. Inside the inner cylinder, a wooden sensor mount was used to hold a magnetometer at a fixed position (see Figure 4.1).

4.3.2 Shaking coils

Degaussing coils were used to implement shaking and the circuit could be reconfigured in order to shake each layer independently, or shake multiple layers simultaneously.

Layer	Outer diameter (mm)	Length (mm)	MuMetal thickness (mm)
Inner	190 mm	402 mm	1.0 mm
Middle	240 mm	475 mm	1.575 mm
Outer	307 mm	580 mm	2.0 mm

Table 4.1: Zero Gauss Chamber dimensions. The dimensions of the inner, middle, and outer cylindrical layers are shown. All measurements were taken without endcaps.

Four sets of degaussing coils were wound along the length of each cylinder, each set consisting of 4 turns (see Figure 4.1). The coils on an individual cylinder were connected in series (such that the total inductance was greater than the sum of the inductance of the individual coils) to ensure that the maximum amount of flux was being driven through the MuMetal (see Figure 4.2).

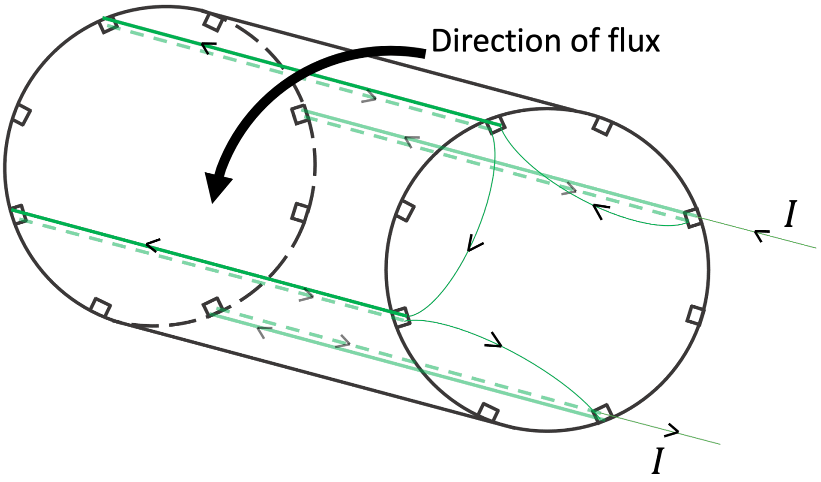

Figure 4.2: *A diagram showing the degaussing coil arrangement for an individual cylinder. The four individual loops are connected in series. The dashed green lines indicate where a wire is running inside the shield and a solid green line indicates where the wire is running outside the shield. The direction of the flux produced by a current flowing around the coils in one direction is shown by the solid black arrow.*

The degaussing circuit used to generate a shaking magnetic field is shown in Figure 4.3. The shaking waveform was generated using a LabVIEW (National Instruments (NI) Corporation, Austin, TX) program and output to the circuit using a 16 bit, NI-9264 C series voltage output module. All modules were mounted in an NI cDAQ-9174 CompactDAQ chassis. The voltage was amplified using an AE Techron 7224 power amplifier (AE Techron, Elkhart, IN) and a 1:1 transformer was used to ensure that any DC offset was removed. The degaussing coils were connected in series with a high-power resistive load ($\approx 0.6\ \Omega$).

The voltage was measured across an in-series high power resistor, V_2 and the current,

I_2 through the degaussing coils was also measured using a AC/DC 1146B current probe (Keysight, Santa Rosa, CA). V_2 and I_2 were recorded using an NI-9205 C series voltage input module.

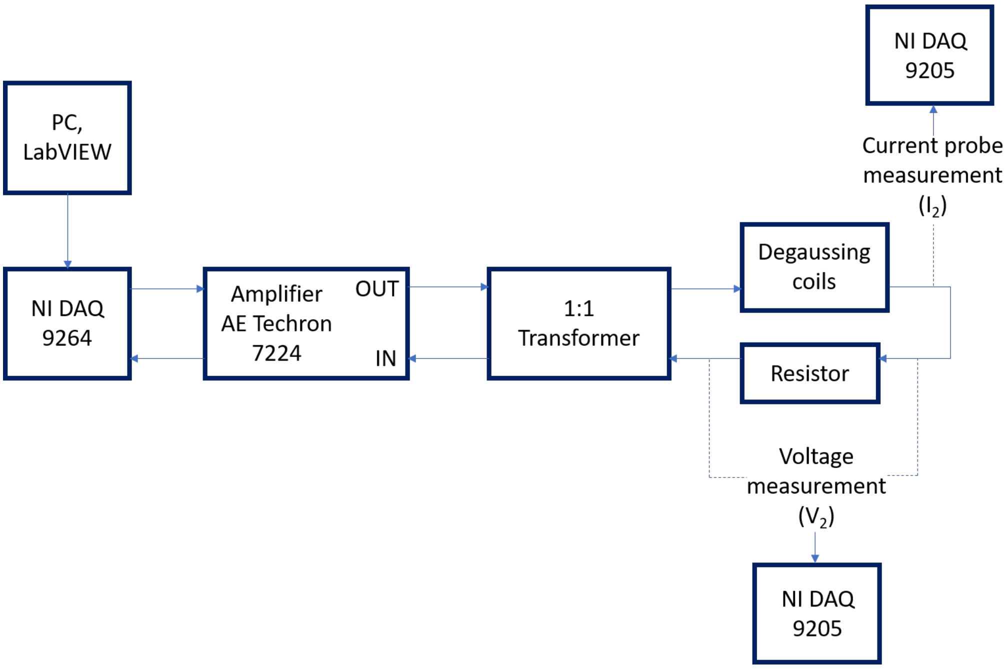

Figure 4.3: *A circuit diagram showing the set-up used to drive the shaking current through the degaussing coils. The shaking waveform was output from a NI DAQ 9264 interfaced with LabVIEW. The voltage was amplified using an AE Techron and a transformer was used to remove any DC offset. The voltage across an in-series resistor was measured using a NI DAQ 9205. A current probe was also used to monitor the current through the coil.*

4.3.3 MSR and Helmholtz coils

All experiments were carried out inside the on-site single layer, MuMetal ‘MuRoom’ at MSL. This provided a stable low-noise environment for the measurements. The remnant magnetic field inside the room was ≈ 250 nT. Inside the MuRoom were a set of circular three-axis 1300 mm Ferronato Helmholtz coils (Serviciencia SLU, Toledo, Spain) which generate uniform magnetic fields in x, y and z directions with a magnetic field homogeneity of $\pm$ 1 % within a sphere of diameter 404 mm centred within the coils (see Figure 4.4). The efficiency of the Helmholtz coils is 50.5 μT/A.

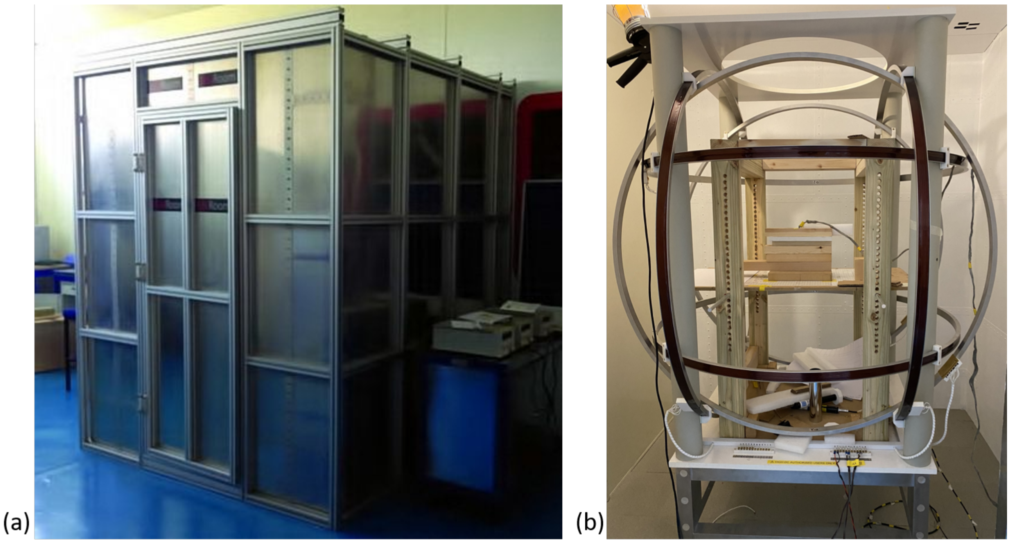

Figure 4.4: *(a) A photograph of the single layer magnetically shielded room (MSR) at Magnetic Shields Limited (Staplehurst, Kent) (Photograph courtsey of Magnetic Shields Limited). (b) A photograph showing the triaxial Helmholtz coils inside the MSR.*

The Helmholtz coils were used to generate interference fields (to calculate the shielding factor of the shield) and were driven using an AE Techron 7226 power amplifier, in-series with a high-power resistive load ($\approx 0.33\ \Omega$) as shown in Figure 4.5.

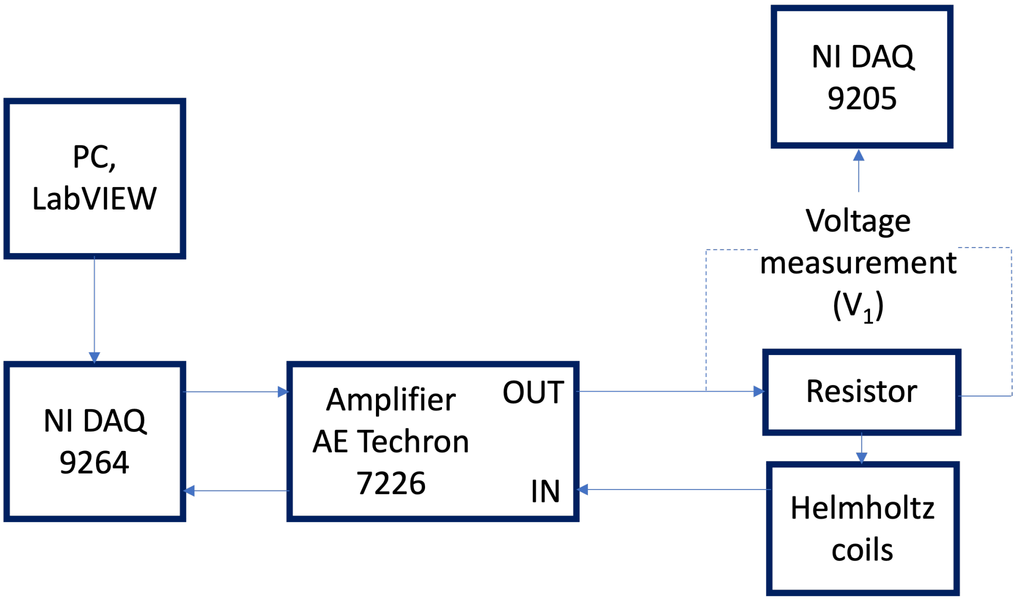

Figure 4.5: *A circuit diagram showing the set-up used to drive the Helmholtz coil currents. Voltage waveforms were output from a NI DAQ 9264 interfaced with LabVIEW. The voltage was amplified using an AE Techron amplifier. The voltage across an in-series resistor was measured using a NI DAQ 9205.*

The sinusoidal current waveforms were generated using a custom LabVIEW program and output to the Helmholtz coil using a 16 bit, NI-9264 C series voltage output module. The voltage output from the DAQ was amplified using an AE Techron 7226 power amplifier. The voltage across an in-series resistor, (V_1) was measured (see Figure 4.5) and used to calculate the current in the circuit during post processing using $I = V/R$. The voltage data were collected using a 16 bit, NI-9205 C series voltage input module.

4.3.4 Magnetometer

A triaxial, Mag-13 TPU100 Bartington fluxgate magnetometer (Bartington Instruments Limited, Witney, UK) was used to measure the interference magnetic field components, B_x, B_y, and B_z (see Figure 4.6). The sensor dynamic range is ± 100 μT; the noise level is $\leq$10 pT rms/$\sqrt{Hz}$ at 1 Hz; the bandwidth is 2,500 Hz. The sensitivity is 0.1 V/μT and the sensor data were sampled at 1250 Hz using a 24 bit NI-9252 C series voltage input module.

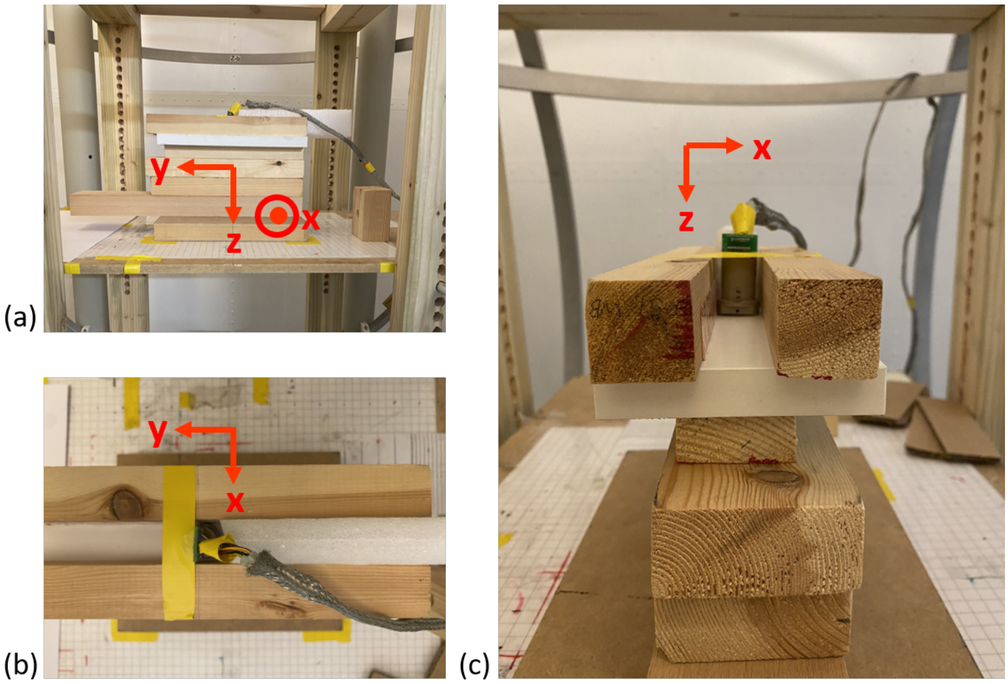

Figure 4.6: *Multiple images showing the position of a Bartington triaxial fluxgate magnetometer during measurements of the interference field without the Zero Gauss Chamber present. (a) The sensor was mounted in a wooden sensor holder and raised using wooden blocks to the same height as the sensor mount in the cylindrical magnetic shield shown in Figure 4.1b. The direction of the sensor axes are shown in red. (b) A bird's eye view of the sensor. Foam and electrical tape were used to keep the sensor in place. (c) Photograph showing the sensor head inside the sensor mount.*

4.4 Characterising the shielding factor of the shield

4.4.1 Experiment

The shielding factor along the axis of the three-layer cylinder (with end caps) was found by taking measurements of the interference field with and without the shield present (see Figure 4.7). The interference field was swept over a range of frequencies (f= 0.1, 0.2, 0.3, 0.4, 0.5, 1, 5, 10, 15, 20, 25, 30, 45, 55, 65, 75, 80, 85, 90, 95, 100, 105 Hz), using a Helmholtz coil producing a magnetic field along the axis of the shield (see Figure 4.7).

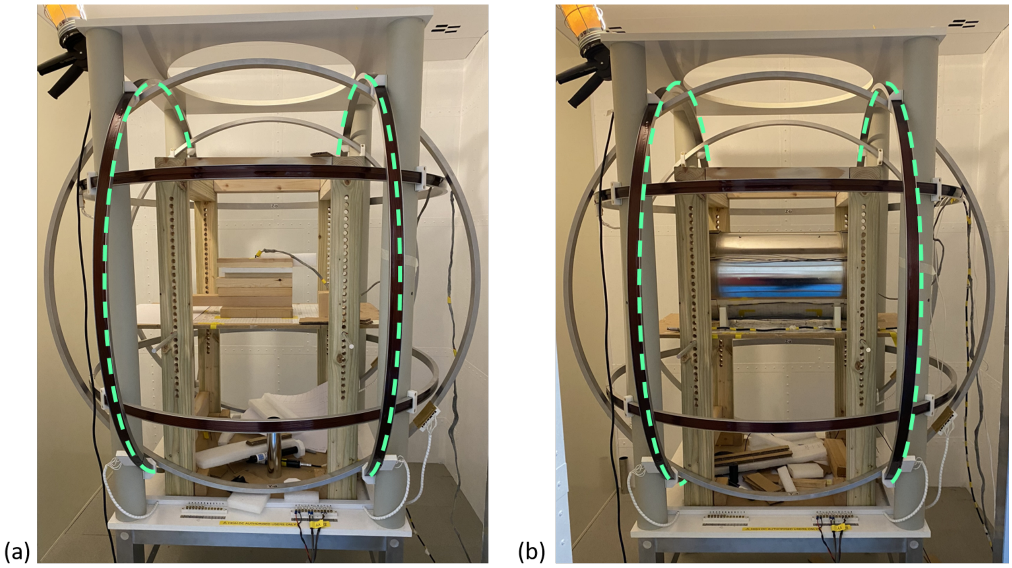

Figure 4.7: *Photographs of the experimental set-up inside the Helmholtz coil, which is marked with a green dashed line. The Helmholtz coil was used to generate interference fields along the axis of the Zero Gauss Chamber. (a) Shows the set up used to measure interference fields without the magnetic shield present. The sensor was mounted on wooden blocks in a sensor holder. (b) Shows the Zero Gauss Chamber positioned in the centre of the Helmholtz coil.*

As the frequency of the current through the interference circuit increased, the increasing inductive impedance of the Helmholtz coil meant that there was a decrease in the total current (and hence the magnitude of the interference field generated by the coils). Therefore, the voltages output from the DAQ were manually adjusted to ensure that the currents through the circuit remained constant as the interference frequency was changed. Figure 4.8a shows how the inductance of the Helmholtz coil affects the current through the coil. When the currents are matched, the current through the coil remains roughly constant as the frequency is varied (see Figure 4.8b). The currents shown in Figure 4.8 were calculated using the voltages measured across the resistor. With a constant current of approximately 1.74 A, the Helmholtz coil produced an interference field of around 88 μT.

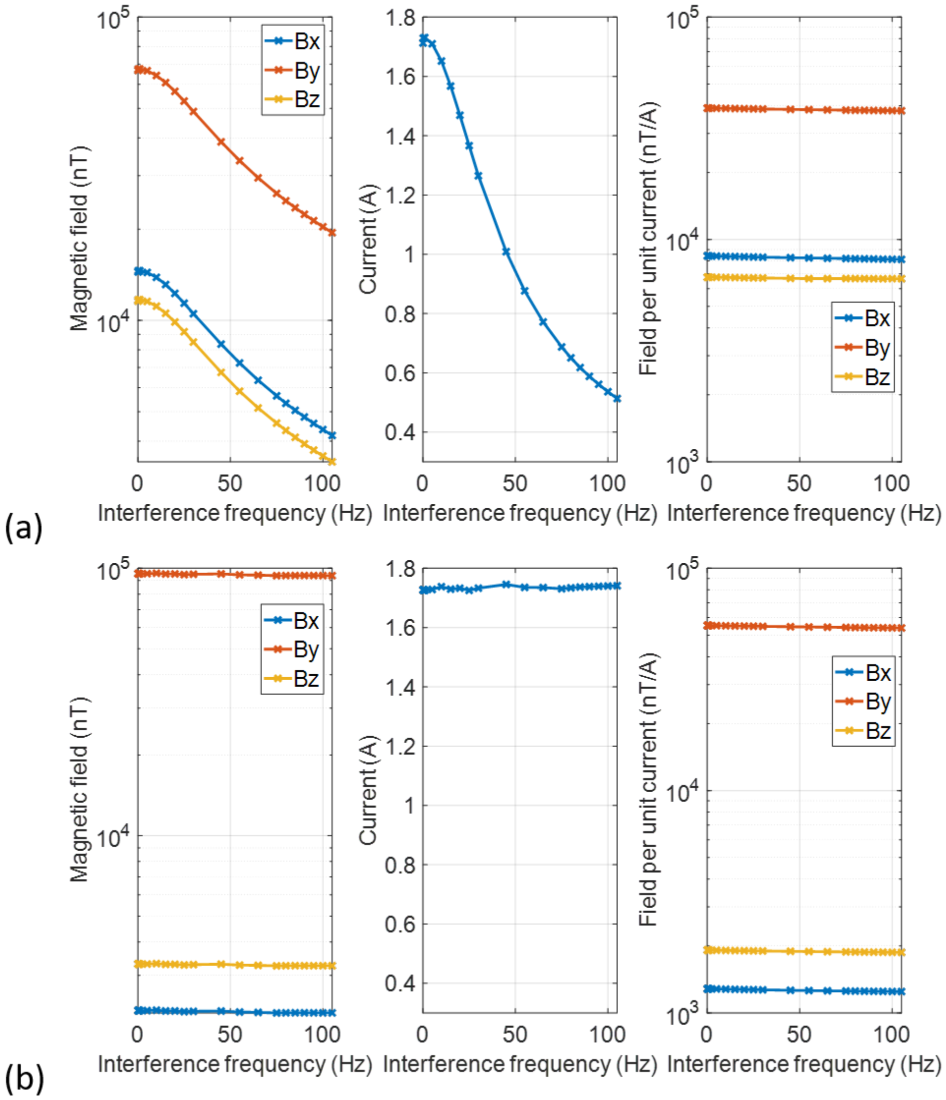

__Figure 4.8:__ Plots showing the variation of the interference field and current through the Helmholtz coils before and after current matching. From left to right the graphs show the variation with frequency of: the the amplitude of the interference field, current amplitude through the Helmholtz coil, and the field per unit current. The measured field components B_x, B_y, and B_z are plotted in blue, red, and yellow respectively. (a) Show the results before current matching. (b) Show the results after current matching. Current matching: adjusting the output voltage from the DAQ to match the Helmholtz current amplitudes across frequencies. Currents were matched to the values recorded without the shield present at the centre of the Helmholtz coil.

The Bartington magnetometer (see Section 4.3.4) was positioned between the Helmholtz coil in a sensor mount which was raised using wooden blocks to be the same level as the sensor height in the Zero Gauss Chamber, as shown in Figure 4.7a. The sensor was held in position using foam and electrical tape.

A sinusoidal waveform was applied to the Helmholtz coil at each interference frequency for 60 seconds. The resulting magnetic field was measured using the Bartington magnetometer along all three sensor axes and the current through the coils was also measured using the methods described in Section 4.3.3.

Before the experiment was repeated with the Zero Gauss Chamber in place (see Figure 4.7b), current matching with the shield within the Helmholtz coil was also repeated due to the MuMetal amplifying the effective inductance and thus further reducing the net current in the interference coils at higher frequencies.

Similar measurements of the shielding factor perpendicular to the axis of the shield were attempted but the very high transverse shielding factors of the nested cylinder, combined with the low sensitivity of the sensor meant that the interference field generated by the Helmholtz coil could not be resolved in this direction.

4.4.2 Data processing

The amplitude of the current across the Helmholtz coil and the amplitude of the interference field detected by the Bartington at each frequency of interest, f (units: Hz) was found by taking a Fast Fourier Transform (FFT) of the data and indexing the single-sided spectrum such that

$$index_f = \frac{2f(L-1))}{F_s} + 1, \tag{4.1}$$

where L is the number of bins in the spectrum, $L = F_s T$. F_s is the sampling frequency (1,250 Hz) and T is the length of the data (50 s).

The complex value was then used to determine the amplitude and phase of the waveform of interest. The amplitude was found by taking the complex magnitude. The phase of the waveform was calculated by finding the complex angle.

4.4.2.1 Calculating the shielding factor

For each frequency sweep, an FFT of the first 50 seconds of the magnetic field data and the current data (calculated from the voltage measured across the in-series resistor) was taken. The amplitude of the peak at the relevant interference frequency was found for both the current and interference fields. The magnitude of the magnetic field components per unit current (nT/A) were then found (see Figure 4.9), with and without the magnetic shield, and finally the shielding factor, SF of the shield was calculated for each interference frequency, where

$$SF = \frac{\text{Field per unit current without shield}}{\text{Field per unit current with shield}}. \tag{4.2}$$

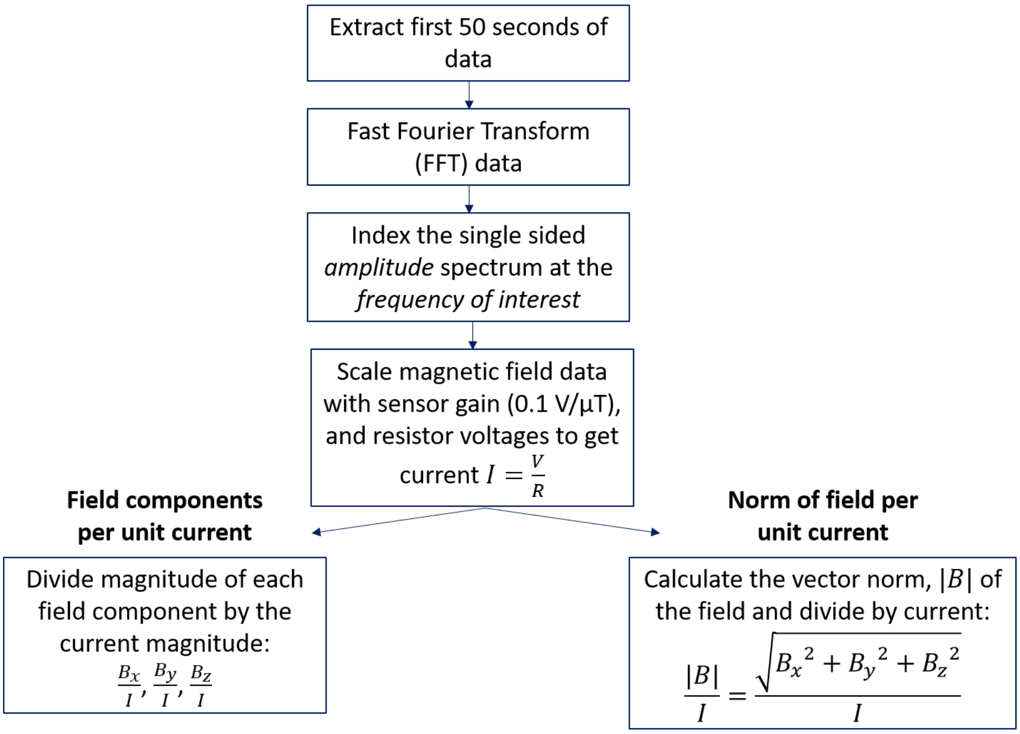

Figure 4.9: *A flow chart outlining the analysis pipeline to calculate the magnitude of the interference field per unit current at each interference frequency.*

4.4.2.2 Phase difference

The phase difference between the current and the magnetic field was found by taking the ratio of the complex maxima of the peaks in the FFT for I and B, and then finding the arctangent of the ratio of the imaginary and real parts of the complex ratio (see Figure 4.10).

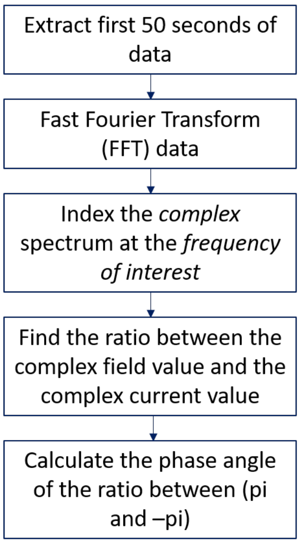

Figure 4.10: *A flow chart outlining the analysis pipeline to calculate the phase difference between the magnetic interference field and the current through the Helmholtz coil.*

4.4.3 Results

Graphs showing how the shielding factor of the Zero Gauss Chamber varies with frequency, and also how the phase difference between the magnetic field along the axis of the shield, B_y and the current through the Helmholtz coil varies with frequency is shown in Figure 4.11. It was expected that without the magnetic shield present the phase should have been zero across all frequencies. However, as the phase difference without the shield was non-zero, the phase difference without the shield present was subtracted from the phase difference found with the shield in place.

The shielding factor at low frequencies, below 1 Hz, is roughly constant at around $4.4{\times}10^4$, and increases to a maximum of approximately $9{\times}10^4$ at around 20 Hz (see Figure 4.11a). The phase difference between the current through the Helmholtz coil and the interference field starts just above zero (see yellow line in Figure 4.11b). The phase difference decreases until turning over at 5 Hz, before increasing until 50 Hz. The phase difference then decreases as the interference frequency increases to 105 Hz.

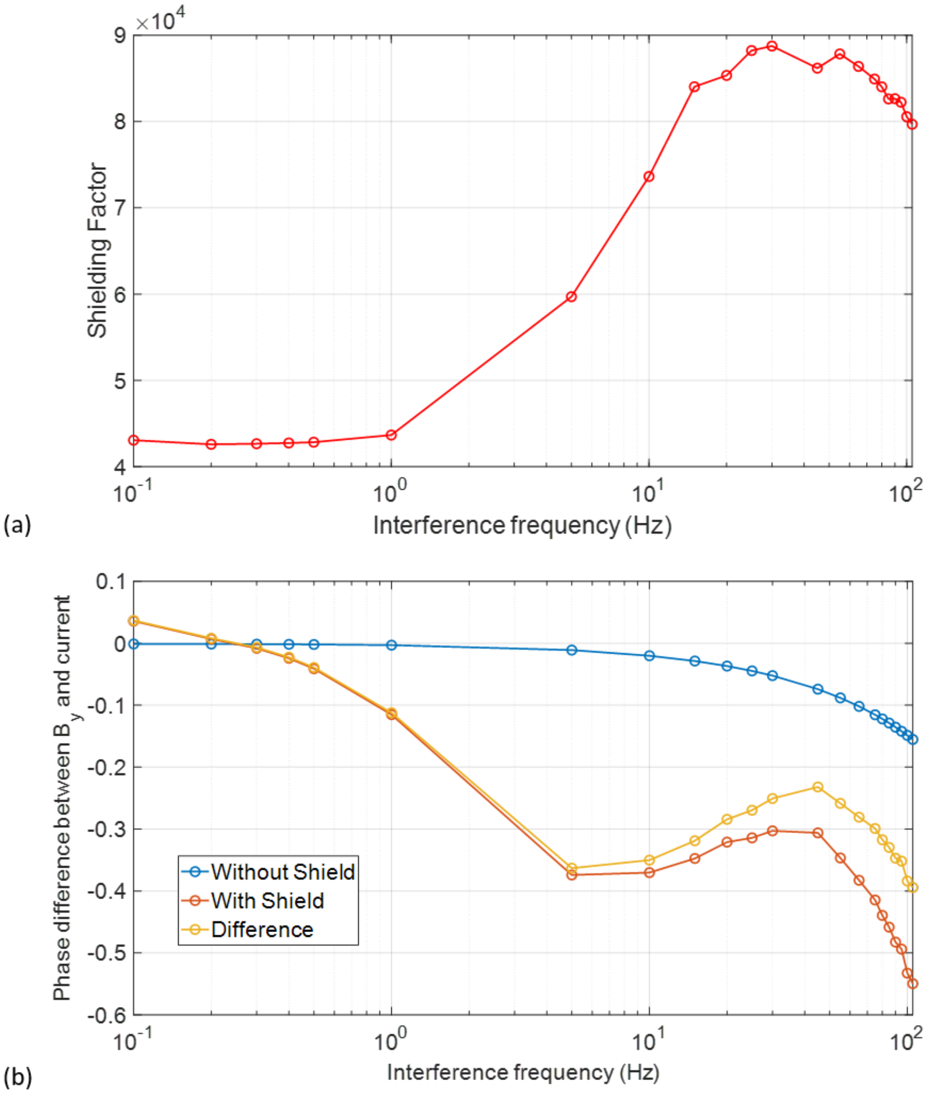

Figure 4.11: *Shielding factor and phase difference results for the Zero Gauss Chamber plotted over a frequency range from 0.1 Hz to 105 Hz. (a) The results of the on-axis interference shielding factors are shown. (b) The phase difference between the current and the component of the magnetic field along the axis of the cylinder is shown. The blue line shows the phase difference without the shield present and the red line shows the phase difference with the shield present. The yellow line is the corrected phase, produced by subtracting the blue from the red line.*

4.5 Shaking

The degaussing coils (described in section 4.3.2) were then used to 'shake' the layers of the Zero Gauss Chamber. The shaking circuit was set up alongside the interference circuit in order to test whether shaking increased the performance of the magnetic shield over the interference frequencies listed in Section 4.4.1.

4.5.1 Varying shaking current amplitude

4.5.1.1 Experiment

The first experiment involved shaking the outer layer of the shield at 51 Hz and investigating the effects of shaking on shielding for interference fields with low frequencies, $f =$ 0.1 Hz, 1 Hz, 5 Hz. The magnitude of the interference field generated by the Helmholtz coil inside the shield is approximately 2.4 nT. The amplitude of the shaking current was varied from 0 A to 1.7 A to determine an optimum current amplitude for shaking.

	Layer	Current (A)	Frequency (Hz)
Shaking	Outer	0 A to 1.7 A	51 Hz
Interference	N/A	$\approx$ 1.74 A	0.1 Hz, 1 Hz, 5 Hz

Table 4.2: A summary of the currents and frequencies used for the shaking and interference fields. The shaking layer is also shown.

4.5.1.2 Data analysis

The data were analysed as described in Section 4.4.2. The field per unit current at each interference frequency was calculated and the shielding factor with shaking, SF_{shake} was calculated where,

$$SF_{shake} = \frac{\text{Field per unit current without shield}}{\text{Field per unit current with shield and shaking}}. \tag{4.3}$$

The ‘gain’ or ‘improvement’ of the shielding factor with shaking was found by dividing SF_{shake} by SF,

$$Gain = \frac{SF_{shake}}{SF}. \tag{4.4}$$

4.5.1.3 Results

A graph showing how the shielding efficiency varied with the shaking current amplitude is shown in Figure 4.12, for several low frequency interference values. The gain in shielding is also shown- the ratio between the shielding factor with shaking and the shielding factor without shaking.

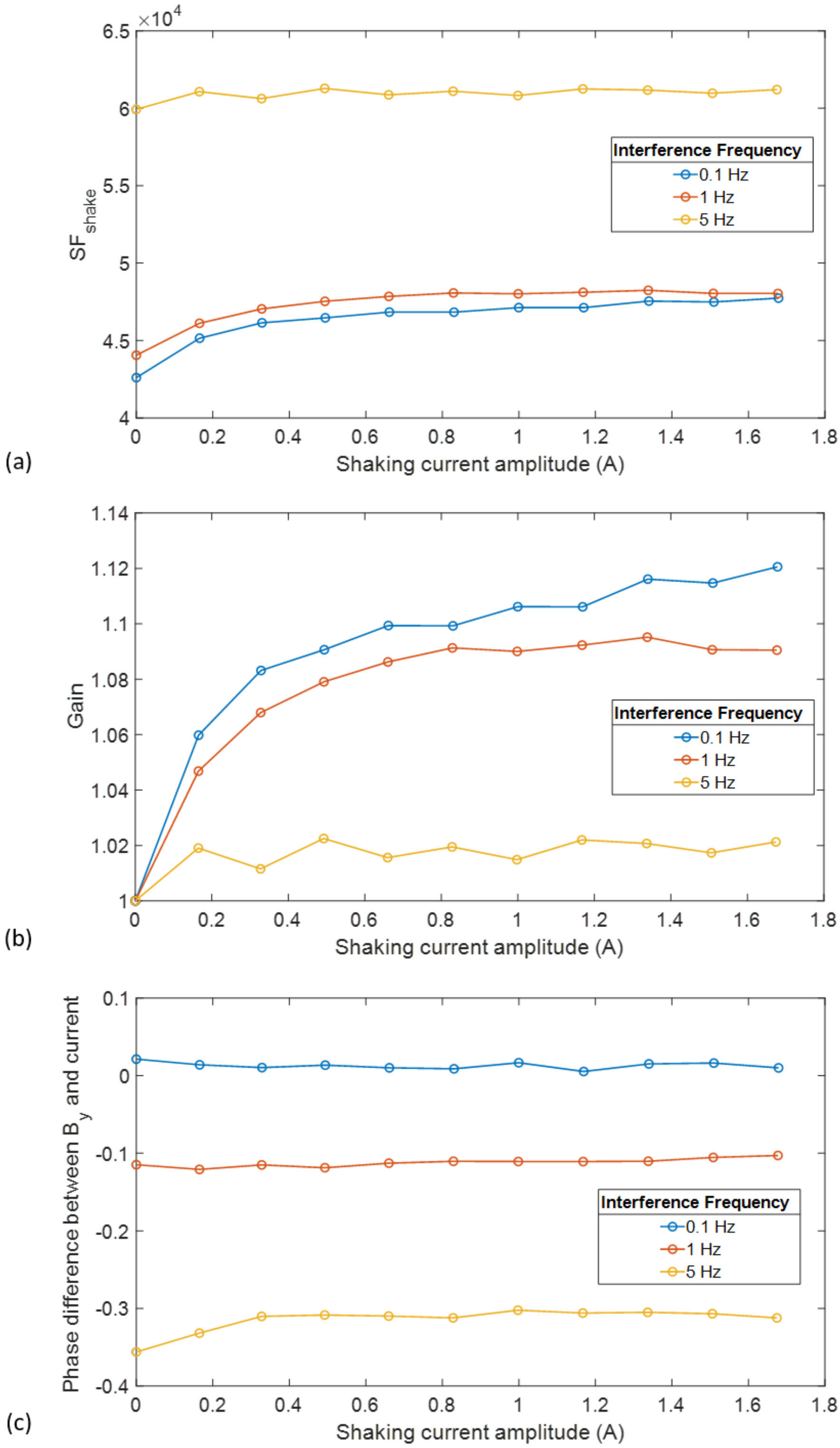

Figure 4.12: *Varying the shaking current amplitude- shielding factor results for when shaking is applied to the outer cylinder of the Zero Gauss Chamber at 51 Hz. The shaking current amplitude was varied between 0 A and 1.7 A. The shielding factors were measured for 0.1 Hz (blue), 1 Hz (red), and 5 Hz (yellow) interference fields. (a) Shows how the shielding efficiency of the cylinder at each interference frequency changed as the current through the shaking coils was increased. (b) The 'gain' or improvement of the shielding factor at each interference frequency with shaking is shown. (c) The phase difference between the interference field along the axis of the shield,* B_y *and the current through the Helmholtz coil is plotted.*

As the shaking current amplitude increases we can see that there is an increase in the shielding factor (see Figure 4.12b). At 5 Hz interference, shaking does not have much effect, even with increasing shaking current amplitude. At very low interference frequencies, 0.1 Hz and 1.0 Hz, the gain is higher but plateaus at higher shaking currents, at around 1.5 A. Shaking the outer cylinder only, at 51 Hz, improved the shielding by a factor of approximately 1.12 ($\approx$ 10 %) for a 0.1 Hz interference frequency at a shaking current of 1.7 A. As there was no decrease in the shielding effectiveness at 1.5 A for a 5 Hz interference field (see Figure 4.12), a shaking current of 1.5 A was chosen for the subsequent experiments. Figure 4.12c shows that there is very little change in the phase difference between the interference field and the interference current as the shaking current amplitude is increased. The phase difference becomes more negative as the interference frequency increases, which agrees with the phase plots shown in Figure 4.11b.

4.5.2 Varying the shaking frequency

4.5.2.1 Experiment

The shaking current amplitude was set at 1.5 A based on Figure 4.12 and the effects of shaking the outer layer only at frequencies 21 Hz, 51 Hz, and 71 Hz were investigated over an interference sweep. Each interference frequency was pulsed for 60 seconds with an interference current amplitude of $\approx$ 1.74 A (current matched). This was to ensure that comparisons could be made between the shielding factors calculated in Section 4.4.1.

	Layer	Current (A)	Frequency (Hz)
Shaking	Outer	1.5 A	21 Hz, 51 Hz, 71 Hz
Interference	N/A	$\approx$ 1.74 A	0.1 Hz to 105 Hz

Table 4.3: A summary of the current amplitudes and frequencies used to generate an interference field and also shake the outer layer of the Zero Gauss Chamber.

4.5.2.2 Results

A graph of how the shielding factor changes over an interference sweep for different shaking frequencies is shown in Figure 4.13. The purple dashed plot shows the shielding factor without shaking. With shaking, there is an improvement in the shielding factor at low interference frequencies up until an interference frequency of 5 Hz, after which there is no improvement in the shielding factor.

The phase difference between the interference field and current through the Helmholtz coils increases up until 5 Hz where the phase turns over. The phase difference then increases as the interference frequency increases.

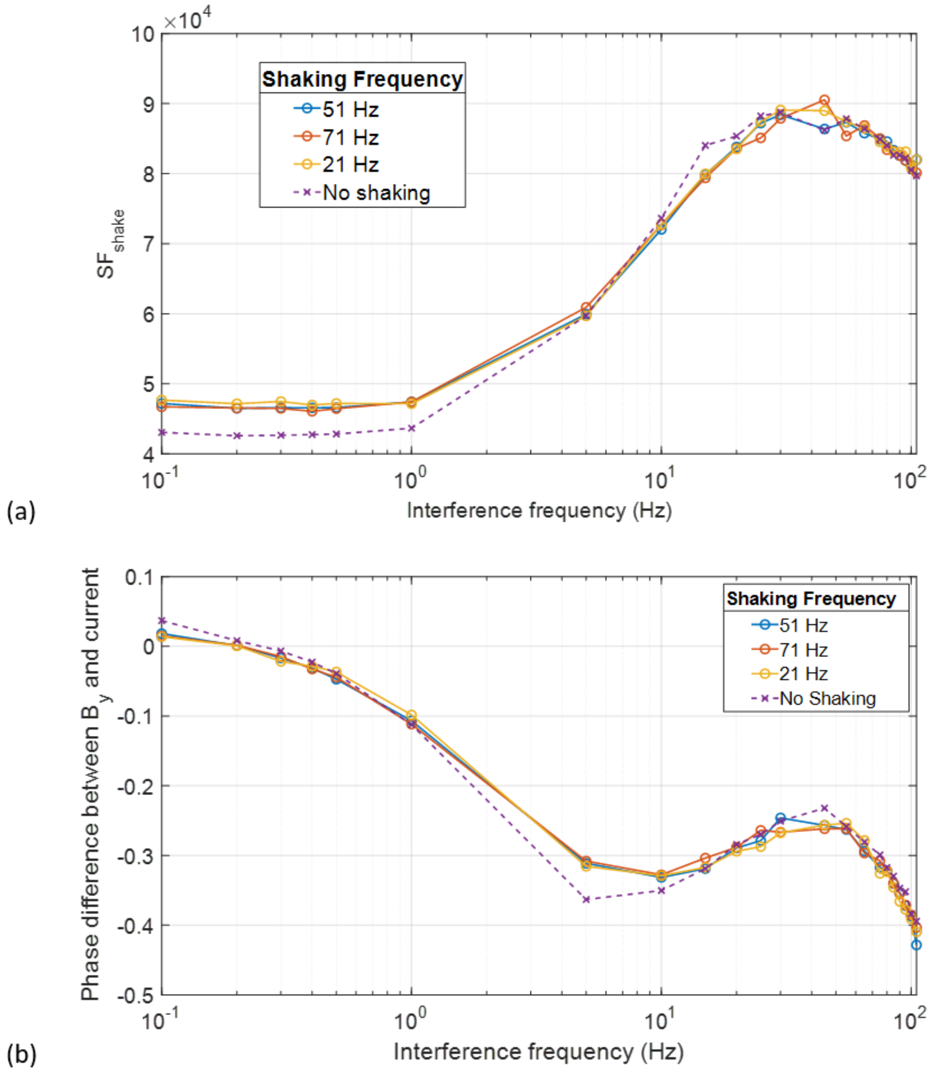

Figure 4.13: *Varying the shaking frequency- Results showing how changing the shaking frequency effects the shielding factor of the Zero Gauss Chamber at different interference frequencies ($f = 0.1, 0.2, 0.3, 0.4, 0.5, 1, 5, 10, 15, 20, 25, 30, 45, 55, 65, 75, 80, 85, 90, 95, 100, 105$ Hz). Shaking was applied to the outer layer at three different frequencies: 21 Hz (yellow), 51 Hz (blue), 71 Hz (red). The shaking current amplitude was set to 1.5 A. The shielding factor when no shaking was applied is shown for comparison (purple dashed). (a) Shows how the shielding factor varies at each interference frequency, when the shaking frequency is set to 21 Hz, 51 Hz, and 71 Hz. (b) Shows how the phase difference between the on-axis magnetic field, B_y and the current through the Helmholtz coil changes over the interference sweep for each shaking frequency.*

The improvement in the shielding factor with shaking over the interference sweep (gain) is shown in Figure 4.14. Results show most improvement in shielding at low frequencies, which steadily declines with increasing interference frequency until around 5 Hz where the effects of shaking have either no impact (1) or negative impact (<1) on the shielding efficiency.

It is interesting to note that there are some positive effects are seen at an interference frequency of 40 Hz for 21 Hz and 71 Hz shaking. However, it is likely that given the opportunity for repeat measurements, the variations seen at high frequency (in both the shielding factor measurements with and without shaking) would average out over the repeats.

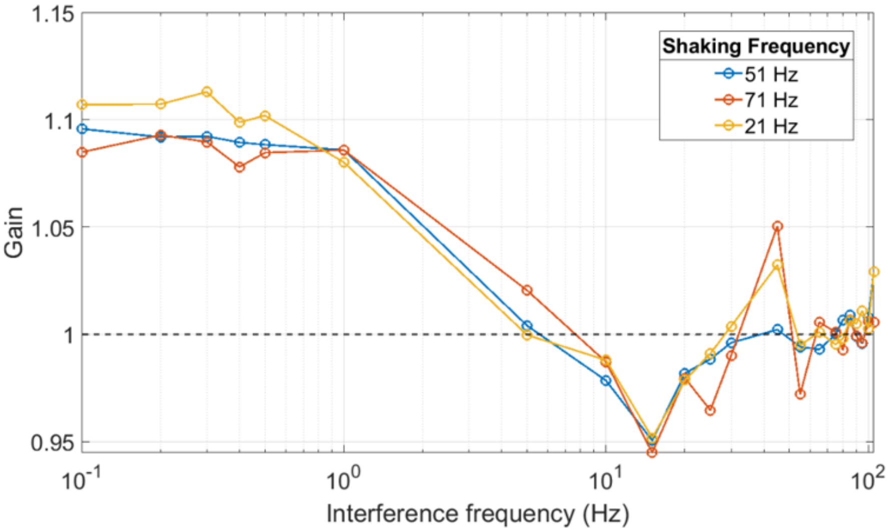

Figure 4.14: *The gain or improvement in the shielding factor of the Zero Gauss Chamber over an interference sweep (f = 0.1, 0.2, 0.3, 0.4, 0.5, 1, 5, 10, 15, 20, 25, 30, 45, 55, 65, 75, 80, 85, 90, 95, 100, 105 Hz) when shaking at 21 Hz (yellow), 51 Hz (blue), and 71 Hz (red). The plot shows how the improvement in the shielding factor with shaking varies with the interference frequency. A dashed black line where the gain is equal to 1 is plotted for clarity- where the gain is less than one there is no improvement in the shielding factor with shaking, and vice versa.*

4.5.3 Shaking different layers- varying current amplitude

4.5.3.1 Experiment

To see how shaking different layers effected the shielding factor of the Zero Gauss Chamber, shaking of the outer layer and then the middle layer was carried out at 51 Hz for a 0.1 Hz interference frequency. The amplitude of the shaking current was swept between 0 A and 3 A in order to determine the optimum shaking current amplitude. The shielding efficiency was calculated for each current amplitude.

The degaussing coils for the outer and middle layer were then connected in series and the experiment described for the middle layer was repeated. The shielding efficiency and

	Layer	Current (A)	Frequency (Hz)
Shaking	Outer	0 A to 2.7 A	51 Hz
	Middle	0 A to 2.5 A	51 Hz
	Both middle and outer	0 A to 2.3 A	51 Hz
Interference	N/A	≈ 1.7 A	0.1 Hz

Table 4.4: A summary of the currents amplitudes and frequencies used to shake the outer layer, middle layer, and both outer and middle layers together.

the effective gain in the shielding factor with shaking was calculated.

The shielding efficiency when shaking each individual layer and shaking the layers in series was compared. The optimum shaking current amplitudes were found and used to inform the current amplitude in later experiments (see Section 4.5.4).

4.5.3.2 Results

Figure 4.15 shows that shaking the middle and outer layer in series improves the shielding efficiency more than shaking the individual layers. Shaking the middle layer improves the gain in shielding factor until a plateau at higher shaking current amplitudes (≈ 2.5 A) is reached.

Not unlike the analytical expression for the shielding factor of a multi-layer spherical shield (see Equation 2.26), the expression for a multi-layer cylinder shows that the shielding factor varies as a product of the individual layers (Mager [1970]). Therefore the product of individual outer and middle gains is also plotted to compare to the gain obtained when shaking both layers. Whilst these plots are similar in magnitude, further investigation into the relationship between the shielding factors of individual layers and the shielding factor of the entire shield is needed before any conclusions can be drawn. Calculating the gain when shaking the middle and outer cylinders individually *and* simultaneously at their own optimal shaking current amplitudes (rather than wiring the cylinders in series) may show better agreement with the calculation of the product.

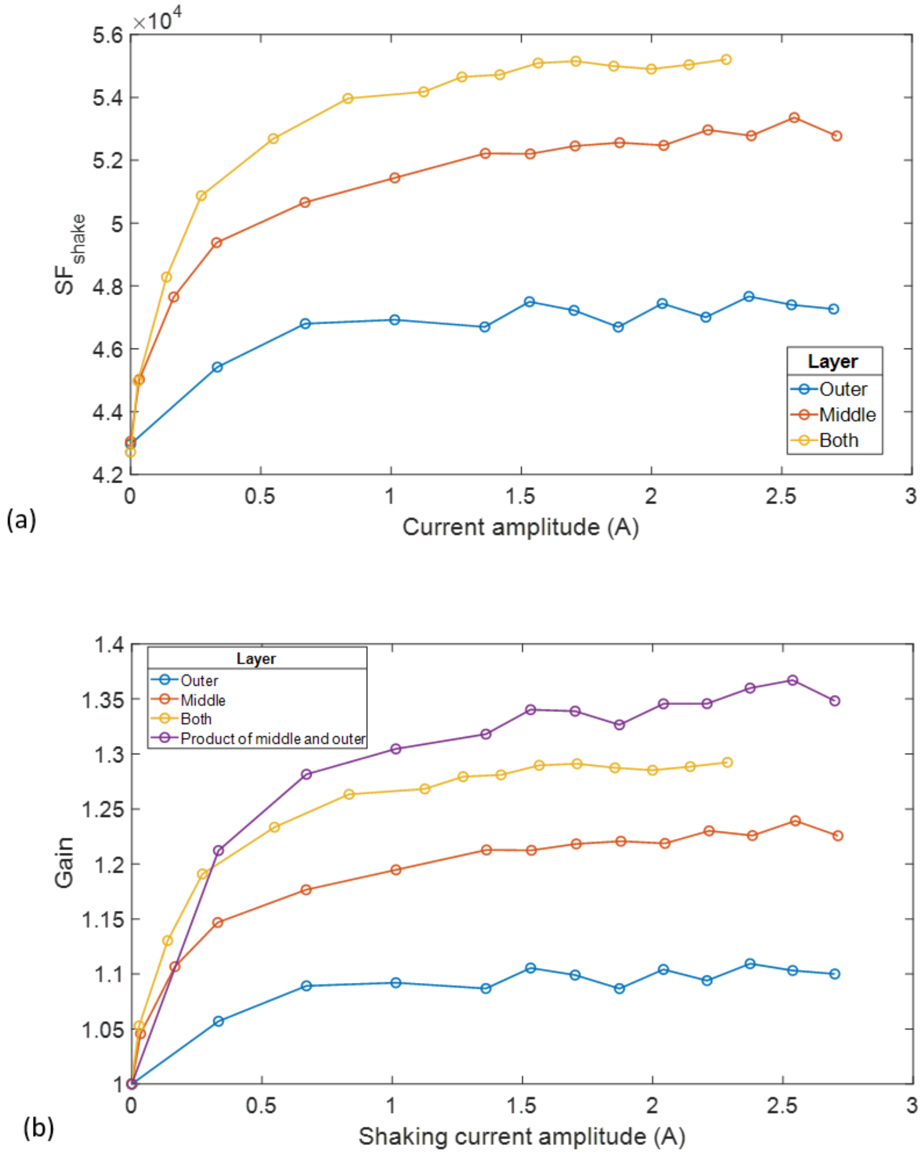

Figure 4.15: *Shaking the different layers of the Zero Gauss Chamber with a varying shaking current amplitude- results showing the affects on the shielding factor at 0.1 Hz of shaking the outer layer (blue), middle layer (red), and finally the middle and outer layer wired in series (yellow). The shaking frequency was 51 Hz, and the shaking current amplitude was varied between 0 A and 2.7 A. (a) Shows how varying the shaking current amplitude affected the shielding efficiency of the shield at 0.1 Hz. (b) Shows the resulting gain in the shielding factor of the Zero Gauss Chamber at 0.1 Hz when shaking each layer. The product of the measured middle and outer gains is also shown (purple).*

4.5.4 Shaking different layers- varying the interference frequency

4.5.4.1 Experiment

A frequency sweep of the interference field was carried out whilst shaking the middle layer and outer layer. The sweep was carried out with 51 Hz shaking at the optimum shaking current amplitudes for each layer described in Section 4.5.3.2 the previous experiment.

	Layer	Current (A)	Frequency (Hz)
Shaking	Outer	1.5 A	51 Hz
	Middle	2.5 A	51 Hz
Interference	N/A	≈ 1.74 A	0.1 Hz to 105 Hz

Table 4.5: A summary of the shaking current and frequency for an interference frequency sweep

The shielding efficiencies and associated gain in the shielding factor were calculated for each layer over the frequency sweep.

4.5.4.2 Results

The effects of shaking the outer layer and middle layer during an interference sweep are shown in Figure 4.16. At low frequencies (below 10 Hz) there is an improvement in the shielding factor with shaking. This effect is most prominent at frequencies below 1 Hz. It can be seen that shaking the middle layer improves the shielding factor the most.

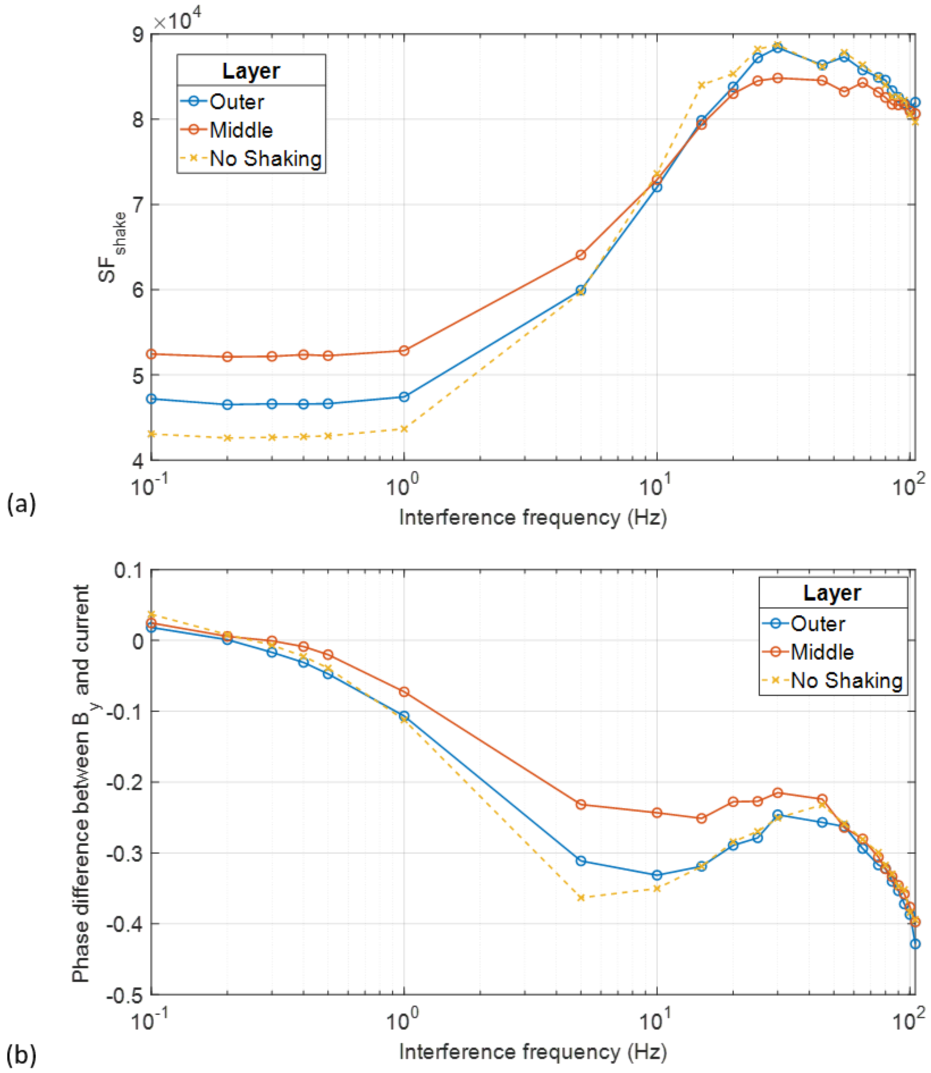

Figure 4.16: *Shaking the different layers of the Zero Gauss Chamber over an interference sweep- results showing the affects on the shielding factor over an interference sweep (f= 0.1, 0.2, 0.3, 0.4, 0.5, 1, 5, 10, 15, 20, 25, 30, 45, 55, 65, 75, 80, 85, 90, 95, 100, 105 Hz) when shaking the outer and middle layer at 51 Hz. A shaking current amplitude of 1.5 A and 2.5 A were used when shaking the outer and middle layer respectively. (a) Shows how the shielding factor changes over an interference sweep when shaking the outer layer (blue) and the middle layer (red). The results when no shaking was applied are plotted for reference (yellow). (b) Shows how the phase difference between the current through the Helmholtz coil and the magnetic field along the axis of the cylinder,* B_y *changed with interference frequency when shaking each layer.*

Figure 4.17 shows the gain, or improvement in the shielding factor with shaking for different interference frequencies. Shaking the middle layer shows a much greater gain in the shielding factor compared to shaking the outer layer, 20% gain compared to 10% gain respectively. The plots show little to no improvement in the shielding factor with shaking at higher frequencies where the gain is less than 1. However, it can be seen that as the interference frequency approaches 100 Hz the gain starts to improve.

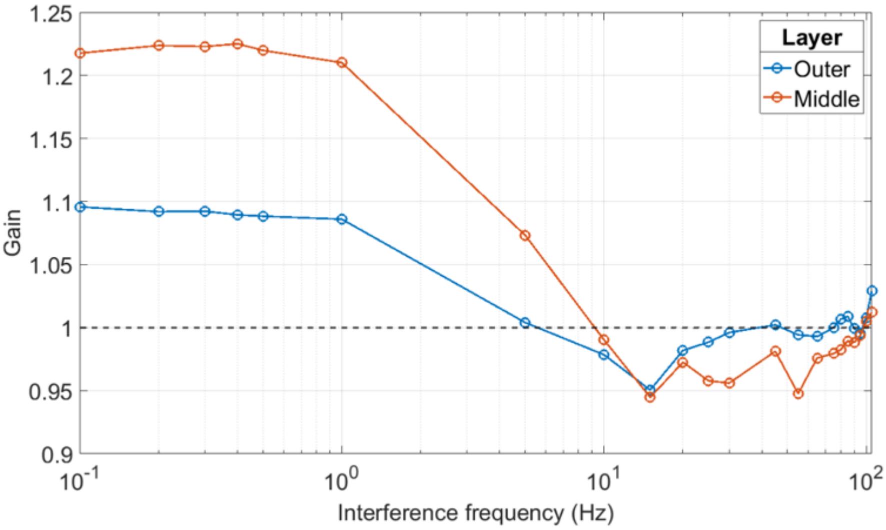

Figure 4.17: *Results showing the resulting gain or improvement in the shielding factor of the Zero Gauss Chamber over an interference sweep (f = 0.1, 0.2, 0.3, 0.4, 0.5, 1, 5, 10, 15, 20, 25, 30, 45, 55, 65, 75, 80, 85, 90, 95, 100, 105 Hz) when shaking the outer (blue) and middle (red) layer at 51 Hz. A shaking current amplitude of 1.5 A and 2.5 A were used when shaking the outer and middle layer respectively. A dashed black line where the gain is equal to 1 is plotted for clarity- where the gain is less than one there is no improvement in the shielding factor with shaking, and vice versa.*

4.6 Discussion of results

4.6.1 Shielding factor measurements

The Zero Gauss Chamber is a highly efficient magnetic shield along the axis of the shield with a shielding factor $\approx 4.4\times10^4$ for low interference frequencies below 1 Hz (see Figure 4.11a). The SF peaks at $\approx 9\times10^4$ at around 30 Hz before decreasing as the interference approaches 105 Hz. The general increase in shielding factor can be explained by an increase in the eddy current shielding mechanism as the interference frequency increases. The general shape of the plots shown in Figure 4.11a is comparable to cylindrical shield measurements previously reported in the literature (Kittel [2010]). Whilst it is uncertain what causes the SF to decrease after the peak at 30 Hz, one could hypothesise that a disruption of eddy current flow at the joins in the MuMetal means that there is an upper limit to the shielding effectiveness. There is also an upper limit on the shielding efficiency due to flux leakage through holes and gaps in the shield.

At high frequencies, especially around 30 Hz and 40 Hz, the plots in Figure 4.11 are not smooth and show quite a lot of variation. Due to the complexity and length of time needed to carry out the shielding factor experiments, including making measurements of the shielding factor with shaking, each set of measurements was carried out only once. It is thought that given more time and repeats, that an averaging effect would reduce the variation that can be seen in the shielding factor plots.

4.6.2 Shaking

4.6.2.1 Shaking current amplitude

Initial shaking measurements shown in Figure 4.12 show that shaking the outer layer of the shield is effective in increasing the shielding effects of the Zero Gauss Chamber at low frequencies ≤ 1 Hz up to a maximum gain of 1.12. No matter how much the shaking current amplitude is increased, there is at most a 2% increase in SF with shaking at interference frequencies above 5 Hz. This can also be seen in Figures 4.13 and 4.14.

Increasing the amplitude of the shaking current improves the shielding effect of the cylinder. This is seen when shaking both the outer and middle layers independently, and shaking both layers together (see Figure 4.15). However, an increase in SF_{shake} is only seen at lower currents (< 1 A) before there is a plateau, and any further increase in the shaking current amplitude does not significantly improve SF_{shake}. Shaking the outer and middle layers together improves shielding up to around 30% at lower shaking current amplitudes compared to shaking just the outer layer, where more current is needed to see a maximum shielding effect of less than 10% (see Figure 4.15b). It was also observed that the gains calculated when shaking both layers together were found to be similar to the product of the gain of the two individual layers (purple trace).

4.6.2.2 Shaking frequency

The improvement in the shielding factor with shaking is similar across each of the shaking frequencies used in these experiments at the optimised shaking current amplitude (see Figure 4.17).

4.6.2.3 Methods

Due to the very efficient magnetic shielding perpendicular to the axis of the shield, only on-axis SF and SF_{shake} measurements were taken. Future experiments should include measuring the shielding factor perpendicular to the axis of the shield. This would need to be done using a more sensitive magnetic field sensor, such as an optically pumped magnetometer.

Shaking of the inner layer could be carried out to see how much the shielding factor increases. However, in practice, shaking the inner layer may be unpractical, as the shaking field is more likely to interfere with measurements inside the inner shield.

Similar to measurements taken by Kelhä et al. [1980], shaking could be carried out at different points in the hysteresis cycle. Depending on where the MuMetal is in the hysteresis cycle, the shield may respond differently to shaking. Whilst the hysteresis measurements performed by Kelhä et al. [1980] were carried out on a toroid, they showed that when the ring was at zero magnetisation, shaking created the largest change in the permeability.

Using Ampere's law (Equation 2.1) to estimate the amplitude of the applied shaking field, H and comparing this to the B-H curve for MuMetal in Figure 2.9, an approximation of the position of the state of the MuMetal on the hysteresis curve can be made. For a shaking current amplitude of 1.5 A and 16 turns of the shaking coils, the outer shell, with a radius, R=0.15 m, H can be estimated to be $\approx$ 25 A/m, placing it close to the point of saturation on the hysteresis curve. Therefore it can be predicted that if the cylinders were degaussed before the experiments (bringing the state of the shield on the hysteresis curve closer to zero magnetisation) then the effects of shaking would be larger than those measured in this chapter.

Hence, any future experiments should include a degaussing cycle before shaking measurements. This is something that was not done in the experiments described in this chapter. Theoretically, after the shield is degaussed, a greater shielding effect would be seen with shaking and therefore larger gains.

The Zero Gauss Chamber was not degaussed before carrying out shielding factor and shaking measurements. Ideally, any remnant magnetisation is reduced with degaussing to improve the shielding factors. Another avenue of investigation is optimising the degaussing of nested cylinders. This may involve degaussing layers sequentially or simultaneously and looking at how the sequence that the layers are degaussed affects the remnant magnetic field in the shield.

4.6.3 Shaking in practice

Shaking is not widely used as a shielding technique. The enhancement in the shielding factor is entirely dependent on the design of the magnetic shield and the shaking parameters (frequency and amplitude of the shaking current). There does not seem to be a "universal" shaking method, and different parameters are used across the literature. Many studies use shaking frequencies close to the mains frequencies (50 Hz/ 60 Hz) or a shaking frequency as high as 1 kHz. However, a recent study of a new three layer magnetically shielded room for ^{3}He / ^{129}Xe magnetometer measurements carried out by Allmendinger et al. [2023], identified an optimum shaking frequency of 0.2 Hz (1 A) based on eddy-current simulations. The group saw an improvement of a factor of ≈ 4 when shaking the outer layer of the MSR, which had a MuMetal thickness of 3 mm.

4.6.4 Shaking and OPM-MEG

As long as the magnitude of the shaking field leaking into the shielded room does not take the OPMs out of their working dynamic range (see Figure 2.28), and shaking is done at a frequency outside any neural oscillations of interest (see Section 2.3.1), then shaking has the potential of being a useful shielding enhancement technique for OPM-MEG. Furthermore, if low shaking frequencies were chosen (such as at 0.2 Hz demonstrated by Allmendinger et al. [2023]), it may be possible to actively screen the shaking field using active magnetic shielding using wall mounted electromagnetic coils (described in Section 2.3.4.2) and a feedback controller (see Section 2.2.3.2).

In this chapter, at the optimum shaking current amplitudes, the magnitude of the shaking field measured by the magnetometer was approximately 0.4 nT when shaking the outer layer, and 31 nT when shaking the middle layer. For shaking to be a viable method in enhancing the shielding factor of an OPM-MEG MSR, the shaking field leaking into the shield would need to be much smaller. However, as the OPM-MEG MSR is degaussed prior to an experiment, the shaking currents needed to obtain a useful SE gain may not need to be as large as the currents needed to enhance the SE of a MSR that is not degaussed.

Typically the distance of the OPMs from the walls of the MSR is also much larger than the distance of the sensor from the cylinders shown in this work (see Figure 4.1b). Therefore if shaking were to be used during an OPM-MEG experiment the magnitude of the shaking field would have decayed more before being measured by the OPM.

Lighter magnetically shielded rooms, using fewer layers of MuMetal, whilst more affordable and easier to build, are usually not as efficient as MSRs with more shielding layers and would hence benefit from the improvement in the shielding factor afforded by shaking. Shaking at lower currents and also shaking the outer layers of the MSR may reduce the impact of any residual shaking field on the OPMs.

Many magnetically shielded rooms, such as the OPM-optimised shield in the Sir Peter Mansfield Imaging Centre at the University of Nottingham, are fitted with degaussing coils in order to minimize the remnant magnetisation in the MuMetal before a MEG experiment. Therefore the effects of shaking would be maximised, as discussed in Section 4.6.2.3.

4.6.5 Physical mechanisms

It is clear from the literature that whilst it is known that shaking improves the shielding factor, researchers do not understand the physical mechanisms that underpin shaking. What is happening at a magnetic domain or crystal lattice level? Is it possible to find a mathematical model that explains these observations? For now, a qualitative description will have to do, but further investigation is needed.

4.7 Conclusions

The shielding factor for a three layer MuMetal cylindrical magnetic shield was found over a range of on-axis interference frequencies between 0.1 Hz and 105 Hz. Between 0.1 Hz and 1 Hz the SF was $\approx$ 44,000. The shielding factor increased to a maximum of $\approx$ 90,000 at 20 Hz interference.

An increase in the shaking current amplitude saw a plateau in the gain of SF_{shake}. The gain in shielding did not vary significantly with varying shaking frequency.

The largest gain in the shielding factor with shaking was seen for low interference frequencies- below 1 Hz the gain was 10% when shaking the outer layer. Shaking the middle layer, or the outer and middle layer together, produced gains of more than 20%.

Chapter 5

Continuous Calibration

Overview

In this chapter a new continuous calibration and field cancellation technique is developed and implemented for a freely moving magnetometer inside a 55 × 55 × 55 cm^3 MuMetal box. Six square electromagnetic coils mounted on the inside walls of the box are driven with sinusoidal currents in order to characterise the magnetic field produced by each coil at the instantaneous position of a fluxgate magnetometer during an experiment. These results are then used to inform the currents needed to null the magnetic field measured by the sensor as the sensor freely translates and rotates.

5.1 Introduction

Head-mounted optically pumped magnetometers have enabled the development of wearable magnetoencephalography (MEG), allowing participants to move whilst being scanned (Boto et al. [2018]). However, large movements through non-zero magnetic fields induce artefacts which can send OPMs outside of their narrow operational dynamic range (± 5 nT) (as described in Section 2.3.3).

Magnetic field control, using electromagnetic coils, can be used to reduce the magnetic field around the sensor array. Previous work has shown that field cancellation carried out prior to scanning, where the coil currents remain fixed throughout an experiment, allow participant head movements whilst keeping the sensors in range (Holmes et al. [2018]). However, movements of the participants are limited to within a $40 \times 40 \times 40$ cm^3 nulled volume whilst measurements take place (Section 2.3.4.2.1).

These limitations arise because of the way that the nulling currents are set at the start of the experiment with any small field drifts within this volume compensated by using dynamic nulling, where coil currents are continuously updated during an experiment (Holmes et al. [2019], Rea et al. [2021]). Before scanning, a change in field generated by each coil, using a known current, is measured to characterise the field change per unit current at the fixed position of the sensors. The field is then nulled by measuring the background magnetic field experienced by each sensor in the OPM array and identifying a set of coil currents from the calibration measurement to reduce the static field at all the sensors to zero.

However, as the sensors translate and rotate away from the compensated region, the background magnetic field experienced by the sensors will change, requiring a new set of currents to be applied through the coils to null the new background field. The change in position of the sensor means that in order to calculate the new coil currents, a new set of coil calibration values will also need to be calculated. Hence, recalibration is required to keep the magnetic field nulled throughout an experiment. To ensure the system remains stable, the recalibration process needs to be fast (accounting for likely participant movements) and continuous.

In this chapter, a new approach is described that could allow continuous monitoring of the field per current generated at the sensors by each coil, with these values then being used to update the currents required to null the field over a sensor array. This involves driving each coil with a current varying at a unique frequency and then monitoring the field produced at the relevant set of frequency values.

Development of this technique was carried out in the large, 55 × 55 × 55 cm^3, MuMetal box using a single three-axis fluxgate magnetometer, with the prospect that this approach might be scaled up to be used to continuously null the magnetic field over a moving OPM array during an MEG experiment. In principle this would enable greater participant movement around the MSR.

5.2 Active magnetic field cancellation

Electromagnetic coils can be used to null remnant magnetic fields, $\boldsymbol{b_0}$ inside a magnetic shield. In simple terms, the coils produce a magnetic field, $\boldsymbol{b_c}$ that is equal in magnitude and opposite in direction to the measured, remnant field,

$$\boldsymbol{b_c} = -\boldsymbol{b_0}, \tag{5.1}$$

effectively creating a net zero magnetic field,

$$\boldsymbol{b_0} + \boldsymbol{b_c} = 0. \tag{5.2}$$

The strength and spatial variation of $\boldsymbol{b_0}$ and the coil field, $\boldsymbol{b_c}$ must be known so that currents applied to the coils will create the exact, equal and opposite magnetic field. The currents can be calculated by measuring the magnetic field to be nulled, $\boldsymbol{b_0}$ where

$$\boldsymbol{b_0} = \begin{bmatrix} b_{x0} \\ b_{y0} \\ b_{z0} \end{bmatrix}, \tag{5.3}$$

and knowing the field per unit current generated by each coil at the position of the sensor.

The magnetic field per unit current, a_{MN} generated by each coil at the sensor can be can be represented by an $M \times N$ matrix, $\boldsymbol{A}$ called the *calibration matrix*,

$$\boldsymbol{A} = \begin{bmatrix} a_{11} & \dots & a_{1N} \\ \vdots & \ddots & \vdots \\ a_{M1} & \dots & a_{MN} \end{bmatrix} \tag{5.4}$$

where M is the number of magnetic field components measured by the sensor, and N is the number of coils in the system.

Using the calibration matrix, $\boldsymbol{A}$ and the static field measurements, $\boldsymbol{b_0}$, the coil currents, $\boldsymbol{I}$ needed to null the remnant field can be calculated.

The current vector, $\boldsymbol{I}$ can be written such that

$$\boldsymbol{I} = \begin{bmatrix} I_1 \\ \vdots \\ I_N \end{bmatrix}, \tag{5.5}$$

where I_1 to I_N are the currents applied to each coil in the system respectively.

By expressing the problem as a linear matrix equation where,

$$\boldsymbol{AI} = \boldsymbol{b_c} \tag{5.6}$$

Equation 5.6 can be rearranged such that

$$\boldsymbol{I} = \boldsymbol{A}^{-1}\boldsymbol{b_c}. \tag{5.7}$$

As the system is underdetermined ($M < N$), only a best approximation of the coil currents, $\hat{\boldsymbol{I}}$ can be found. This can be done by inverting the coil calibration matrix $\boldsymbol{A}$ using a Moore-Penrose pseudo inverse, $\boldsymbol{A}^+ = (\boldsymbol{A}^T\boldsymbol{A})^{-1}\boldsymbol{A}^T$ and rewriting Equation 5.7 so that

$$\hat{\boldsymbol{I}} = \boldsymbol{A}^+\boldsymbol{b_c}. \tag{5.8}$$

If $\boldsymbol{b_c}$ = - $\boldsymbol{b_0}$ then,

$$\hat{\boldsymbol{I}} = -\boldsymbol{A}^{+}\boldsymbol{b_0}. \tag{5.9}$$

By applying $\hat{\boldsymbol{I}}$ to the coils the magnetic field $\boldsymbol{b_0}$ at the position of the sensor can be cancelled.

5.3 Proportional feedback controller

If the background magnetic field changes over time, the coil currents needed to cancel these magnetic fields will also need to change. To maintain the magnetic field around a set-point (i.e. zero field), a *feedback controller* can be used to control the currents (see Section 2.2.3.2 for further details on feedback controllers).

For a change in field, $\Delta\boldsymbol{b_c}$ the currents needed to null this change, $\Delta\hat{\boldsymbol{I}}$ can be calculated using Equation 5.9, such that

$$\Delta\hat{\boldsymbol{I}} = -\boldsymbol{A}^{+}\Delta\boldsymbol{b_c}. \tag{5.10}$$

A *proportional* feedback controller requires that the calculated current is scaled by a variable called the proportional gain, K_p which can be tuned to ensure that the system responds quickly and efficiently.

If the gain is too large then the system will become unstable. If the gain is too small then the response of the controller will be too slow.

The current output to the coils from the feedback controller also takes into account any previously applied current, and so the current fed back to the coils after the ith iteration of the feedback loop, $\boldsymbol{I_{applied}}$ can be written as

$$\boldsymbol{I}^{i+1}_{\boldsymbol{applied}} = K_p\hat{\boldsymbol{I}}^{i} + \sum_{n=0}^{i}\boldsymbol{I}^{n}_{\boldsymbol{applied}}. \tag{5.11}$$

Substituting in Equation 5.10, Equation 5.11 becomes

$$\boldsymbol{I}^{i+1}_{\boldsymbol{applied}} = -K_p\boldsymbol{A}^{+}\boldsymbol{\Delta b}^{i}_{\boldsymbol{c}} + \sum_{n=0}^{i}\boldsymbol{I}^{n}_{\boldsymbol{applied}}. \tag{5.12}$$

If the sensor is moving, this means that the calibration matrix, $\boldsymbol{A}$ will also change and this will need to be taken into account when updating the currents using the feedback controller. Hence Equation 5.12 can be adjusted slightly such that

$$\boldsymbol{I}^{i+1}_{\boldsymbol{applied}} = -K_p \boldsymbol{A}^{+j} \boldsymbol{\Delta b}^{i}_{\boldsymbol{c}} + \sum_{n=0}^{i} \boldsymbol{I}^{n}_{\boldsymbol{applied}}, \tag{5.13}$$

where the superscript j indicates that $\boldsymbol{A}^{+}$ is changing if the sensor is moving and was updated at the jth timestep.

5.4 Hardware

5.4.1 Magnetic shield

A 55 × 55 × 55 cm^3 box formed from a single 1.5 mm thick layer of MuMetal (the "MuBin") as introduced in Chapter 3 was used to develop and test the continuous calibration technique (Figure 5.1a).

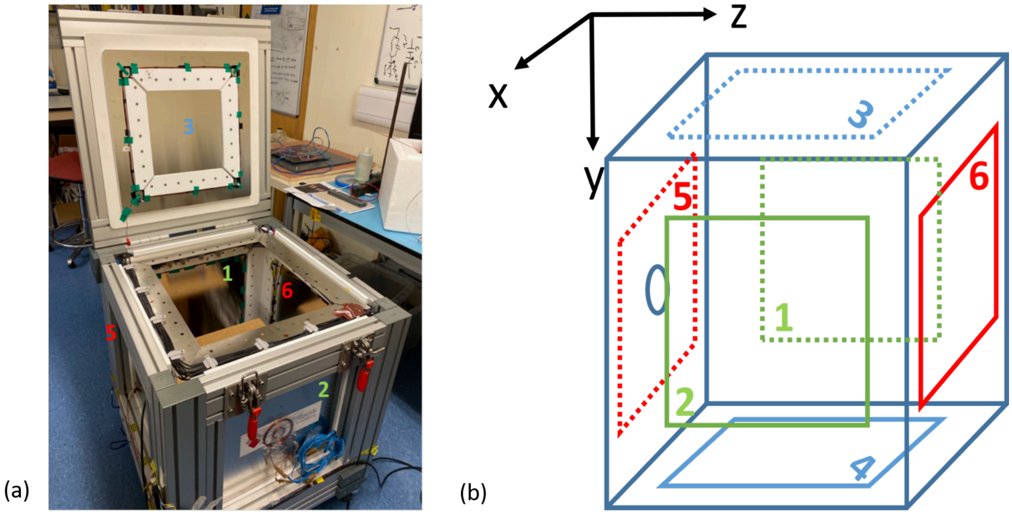

Figure 5.1: *A single layer, MuMetal magnetically shielded box, the "MuBin", which was introduced in Chapter 3, with square electromagnetic coils mounted to the inside faces. (a) A photograph showing the MuBin. Each face is labelled from 1 to 6. 37 × 37 cm^2 square coils (each formed from 10 turns) are mounted to the inside faces of the box. (b) A schematic diagram showing the positions of the coils, each labelled 1 to 6 according to the box face. Coils 1 and 2, in green, lie along the x axis of the box. Coils 3 and 4, in blue, lie along the y axis of the box. Coils 5 and 6, in red, lie along the z axis of the box. The position of the hole in the side of the MuBin lies along the x axis.*

A small 4 cm diameter hole at the centre of face 5 was used to access the sensor in the box.

5.4.2 Electromagnetic coils

Six 37 × 37 cm^2 square coils (each formed from 10 turns of 0.56 mm diameter, enamelled copper wire) were mounted onto the inside faces of the MuBin.

The positions of the coils, labelled 1 to 6, are shown in Figure 5.1b. The main axes of the coils are: (x) coils 1 and 2; (y) coils 3 and 4; (z) coils 5 and 6.

Each coil was connected to a low-noise coil driver (QuSpin Inc, Louisville, CO). The coil driver output is ±5 V; the bandwidth is 0-70 Hz; and the noise floor is < 25 nV/$\sqrt{Hz}$ at 2 Hz. The coil currents were controlled using custom LabVIEW code (National Instruments (NI) Corporation, Austin, TX) interfaced with a 16 bit, NI-9264 C series voltage output module in a NI-9174 cDAQ chassis. Each coil was wired in series to a 10 Ω resistor and the voltage across the resistor for each coil, V_N (N =1 to 6) was measured using a 16 bit, NI-9205 C series voltage input module.

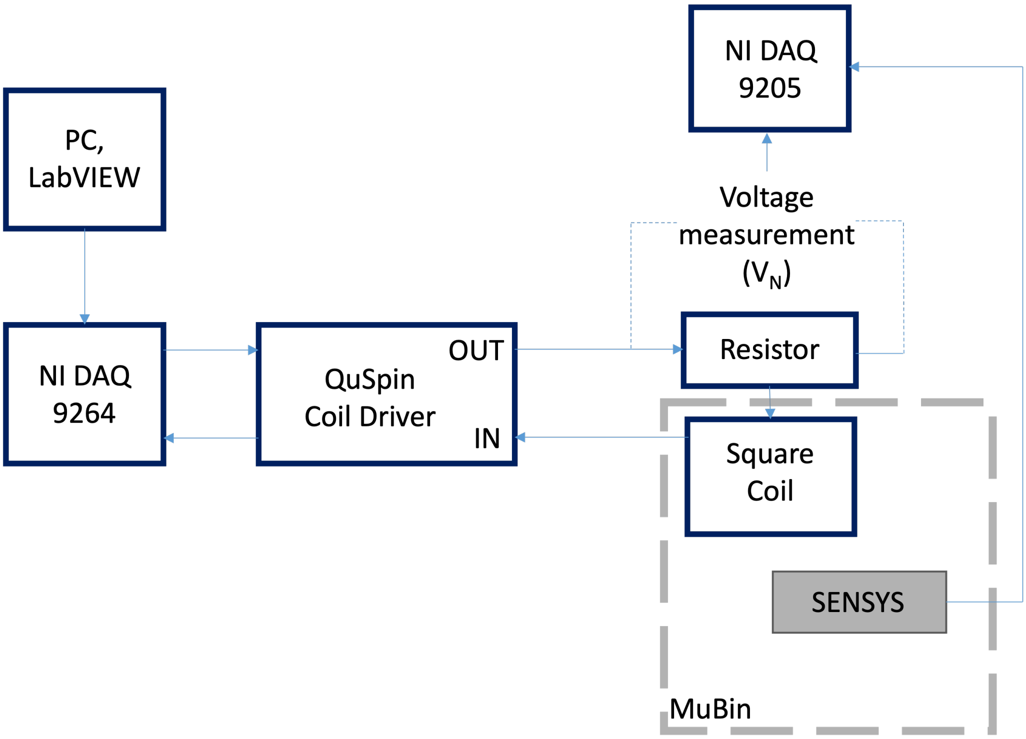

Figure 5.2: *A circuit diagram showing the wiring of an individual electromagnetic nulling coil inside the MuBin. Each of the six coils is connected in series to a 10 Ω resistor, and driven using a low-noise coil driver. Voltage waveforms were output to the coils using a NI DAQ 9264 interfaced with LabVIEW. A NI DAQ 9205 was used to measure the voltage across the in-series resistors in order to calculate the current through each coil. The output of a SENSYS fluxgate magnetometer positioned inside the MuBin was measured using the same NI DAQ module.*

5.4.3 Magnetic field sensor

The SENSYS FGM3D-100 three-axis fluxgate magnetometer, which was described in Section 3.4.1.3, was used to measure the magnetic field inside the box. The sensor measurements were collected using the same NI-9205 input module (see Figure 5.2).

5.5 Calibration

5.5.1 Driving the coils

In order to calculate the calibration matrix (Equation 5.4), the six electromagnetic coils were driven simultaneously with sinusoidal waveforms, $I_{calibration}$, with each coil being driven at a unique frequency, f_n (where n=1, . . . , 6 for N coils).

Whilst driving the coils, the magnetic field and the voltage across each in-series resistor was simultaneously sampled (see circuit diagram in Figure 5.2). The voltage across the resistor was converted to current through the circuit (using $I = \frac{V}{R}$) and the sensor measurements were converted to microtesla using the sensor gain, 0.1 V/μT.

5.5.2 Finding the magnitude of the magnetic field and coil currents

Assuming that the coil frequencies were spaced at regular intervals, δf, the minimum sample time (in seconds) required to resolve each frequency with a Fast Fourier Transform (FFT) was $T_{min} = \frac{1}{\delta f}$ (see Figure 5.3).

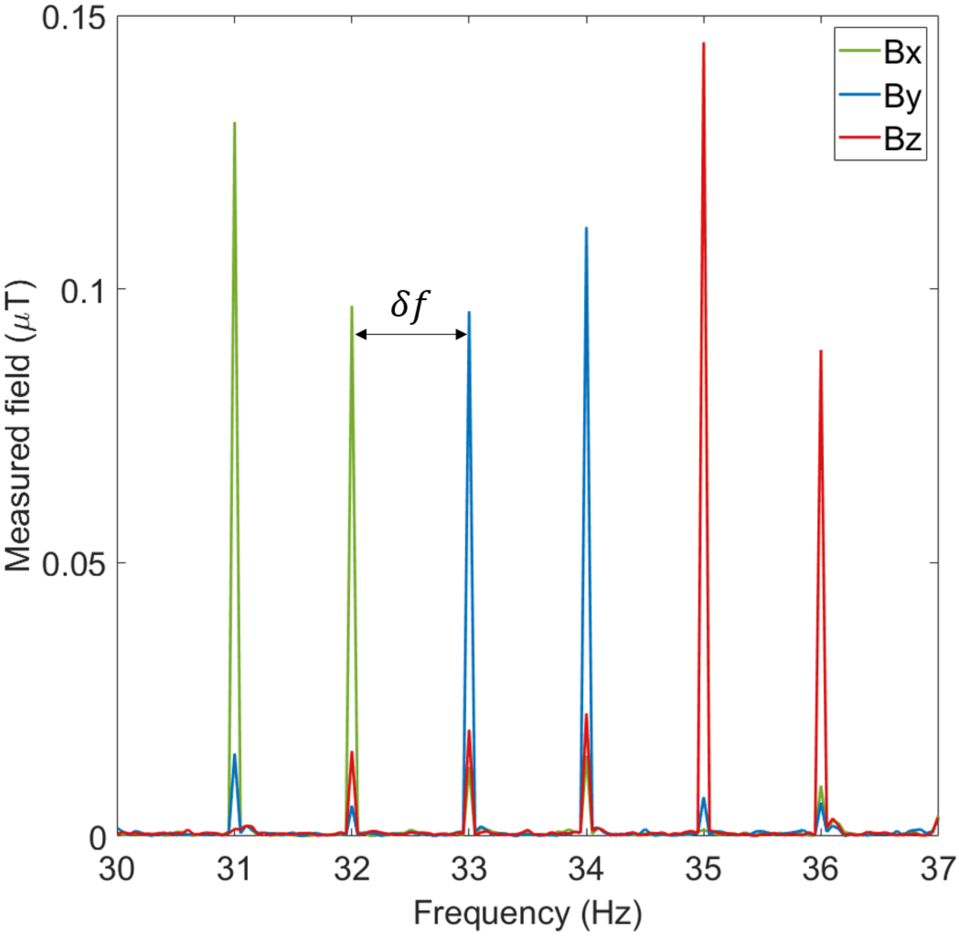

Figure 5.3: *A spectrum showing the Fast Fourier Transform of the magnetic field measured by a three-axis fluxgate magnetometer whilst the coils inside the MuBin were being driven at their unique frequency. The three components of the magnetic field,* B_x*,* B_y*, and* B_z *are shown in green, blue and red respectively. Each frequency corresponds to a single coil inside the MuMetal box. For coils 1 to 6 these frequencies correspond to 31 Hz, 32 Hz, 33 Hz, 34 Hz, 35 Hz, 36 Hz. The frequency interval,* δf *is shown. The minimum measurement time needed to resolve the peaks in this spectrum is 1 s (for the purpose of this figure, the time,* T *was 20 s).*

The magnetic field data and current data were then passed through an FFT, and the magnitude of the measurement at each frequency was obtained by finding the peaks in the spectrum (see Figure 5.3). The amplitude of each magnetic field component per unit current was then calculated.

Figure 5.3 shows the spectrum obtained when the magnetic field sensor was orientated such that the B_z axis of the sensor was pointing along the line between coils 5 and 6, B_y was pointing along the line between coils 3 and 4, and the B_x component was pointing along the line between coils 1 and 2.

5.5.3 Directional information

The next step was to determine the direction of the magnetic field per unit current produced by the coil, assuming no prior knowledge of the direction of the coil windings or the position and orientation of the magnetometer in the space between the coils. This was done by finding the phase difference between the measured magnetic field and the current for each coil. The phase difference was found by taking the ratio of the complex maxima of the magnetic field and current, and then finding the arctangent of the ratio.

If the phase difference was a factor of π or -π, the direction of the field per unit current was negative. If the phase difference was 0, then the direction was positive.

The magnitude and direction of the field per unit current for each of the three magnetic field components generated by each coil form the coil calibration matrix, $\boldsymbol{A}$ (see Equation 5.4).

5.5.4 Example

Examples of how the calibration matrix values change when a sensor is rotated anticlockwise by 180° are shown in Figure 5.4. The fluxgate magnetometer (described in Section 5.4.3) was placed on a flat wooden board, raised halfway between coils on the top and bottom faces at the centre of the MuBin (see coils 3 and 4 in Figure 5.1). The sensor was rotated as shown in Figure 5.4, and the calibration matrix was calculated at each position using a custom LabVIEW program which implemented the technique described in Section 5.5.3. At 0° the z axis of the sensor was pointing along the axis of coils 5 and 6, whilst at 90° it pointed along the axis of coils 1 and 2

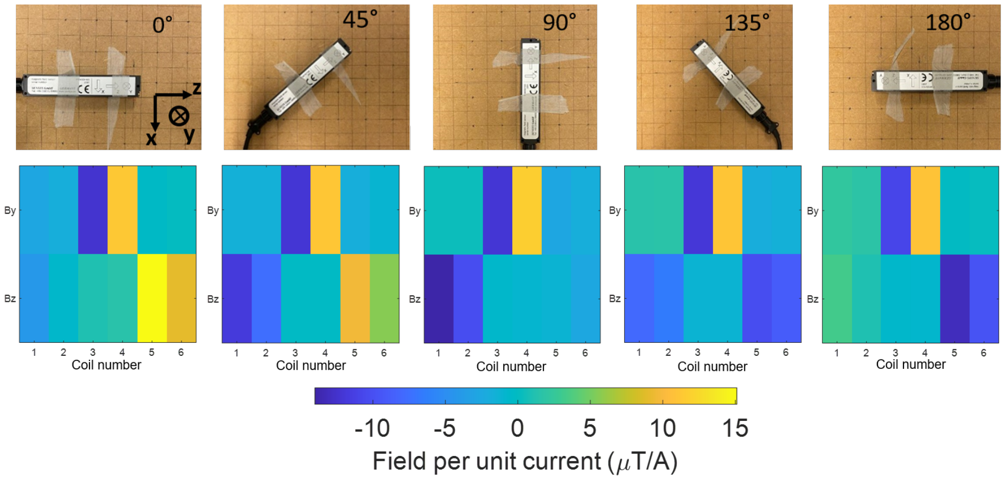

Figure 5.4: *(Top) Photographs showing the SENSYS magnetometer being rotated by 180°. At each position (0°, 45°, 90°, 135°, and 180°) the calibration matrix was calculated by sampling the magnetic field produced by the coils. The directions of the three sensitive axes of the magnetometer at 0° are shown. (Bottom) Shows the colour maps of the calibration matrix at each position. The x axis of the map is labelled with each coil number and the y axis of the map is labelled with two of the sensitive axes of the fluxgate magnetometer,* B_y *and* B_z*. The colour plots show the direction of the field per unit current produced by each coil.*

At each position, coils 1 to 6 were driven simultaneously at frequencies 31 Hz, 32 Hz, 33 Hz, 34 Hz, 35 Hz, and 36 Hz respectively. To ensure that the peaks at each frequency in the FFT could be resolved, the magnetic field and current data were sampled for $T_{min} = 1$ second at 1,200 Hz.

The field component per unit current for each coil is shown in Figure 5.5. As the sensor axes were not changing relative to the sensitive axes of coils 3 and 4, the field contribution from coils 3 and 4 remains roughly constant. The contribution of the magnetic field from a coil is largest when a sensitive axis of the magnetometer is aligned along the axis of a coil. This can be seen clearly for coils 1 and 2. When the z axis of the magnetometer is at 90° the magnitude of the field per unit current is largest.

In the rotation example shown in Figures 5.4 and 5.5, the B_x sensitive axis of the magnetometer was not recording, therefore only the B_y and B_z components are shown. However, had the channel been recording, this axis would demonstrate similar behaviour to the B_z components of the calibration matrix.

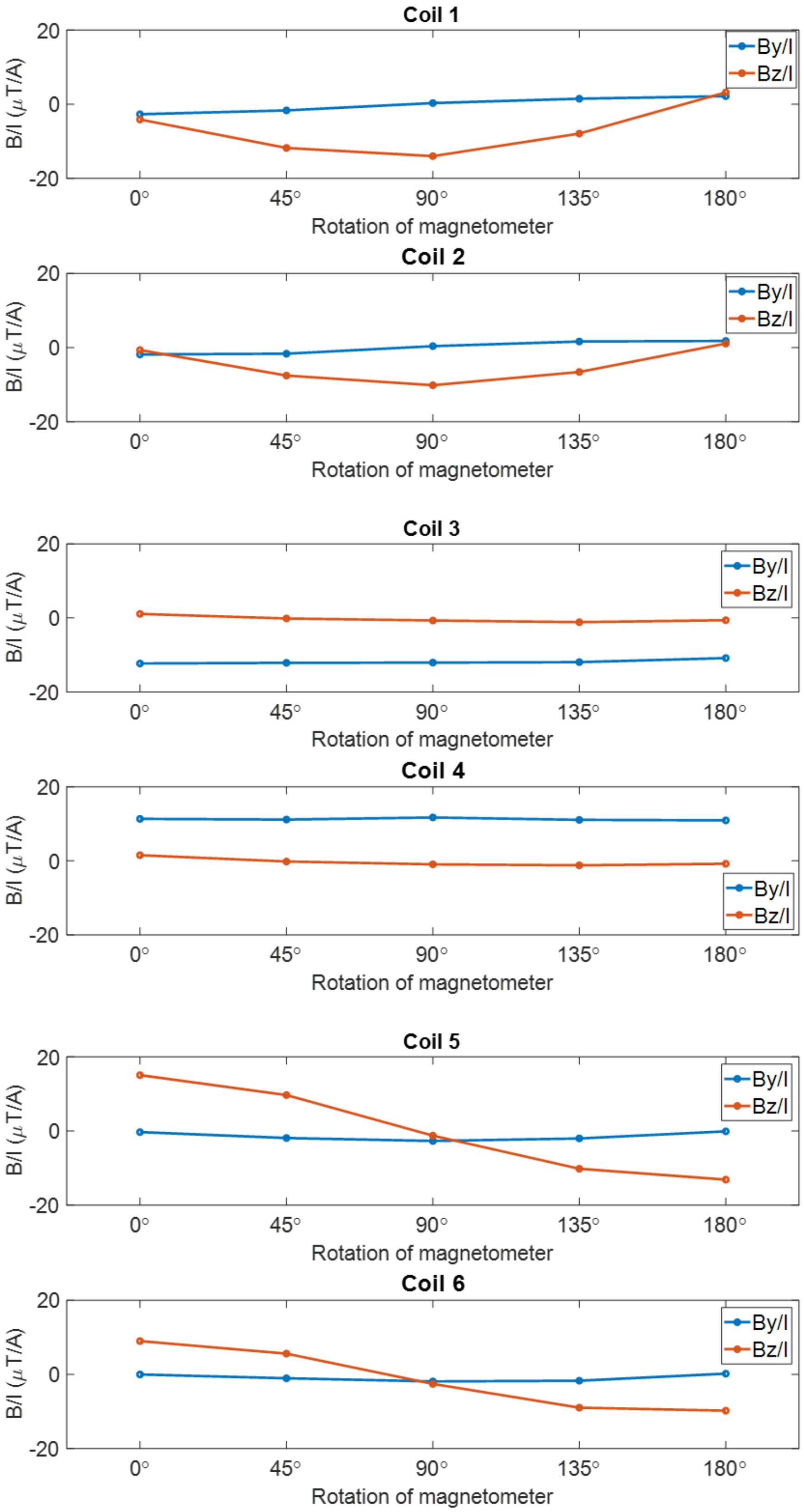

Figure 5.5: *The magnetic field per unit current ($\mu T/A$) generated by each coil during a rotation of the fluxgate magnetometer. The field per unit current produced by each coil, 1 to 6 (top to bottom) is shown as a line plot for the B_y and B_z magnetic field components as the sensor rotates through 180°. B_y/I and B_z/I are plotted in blue and red respectively.*

It can be seen from Figure 5.5 that in order to null the magnetic field, the calibration matrix must be updated when the sensor rotates and translates.

5.6 LabVIEW program development

5.6.1 Overview

A custom LabVIEW program was developed to perform continuous calibration and nulling of the background magnetic field with a moving triaxial fluxgate magnetometer in the MuBin. The currents through six square coils (see Figure 5.1) were updated to null the low frequency variation in the three components of the background magnetic field measured by the sensor. The program implemented the calibration technique described in Section 5.5, to account for the changing contribution of the magnetic field of each coil due to sensor movement. A feedback controller was used to update the coil currents by monitoring the background magnetic field (see Section 5.3).

5.6.2 Process flow chart

A flow chart shown in Figure 5.6 introduces and outlines the calibration and nulling process, before a more detailed description of the LabVIEW program is presented in Section 5.6.3.

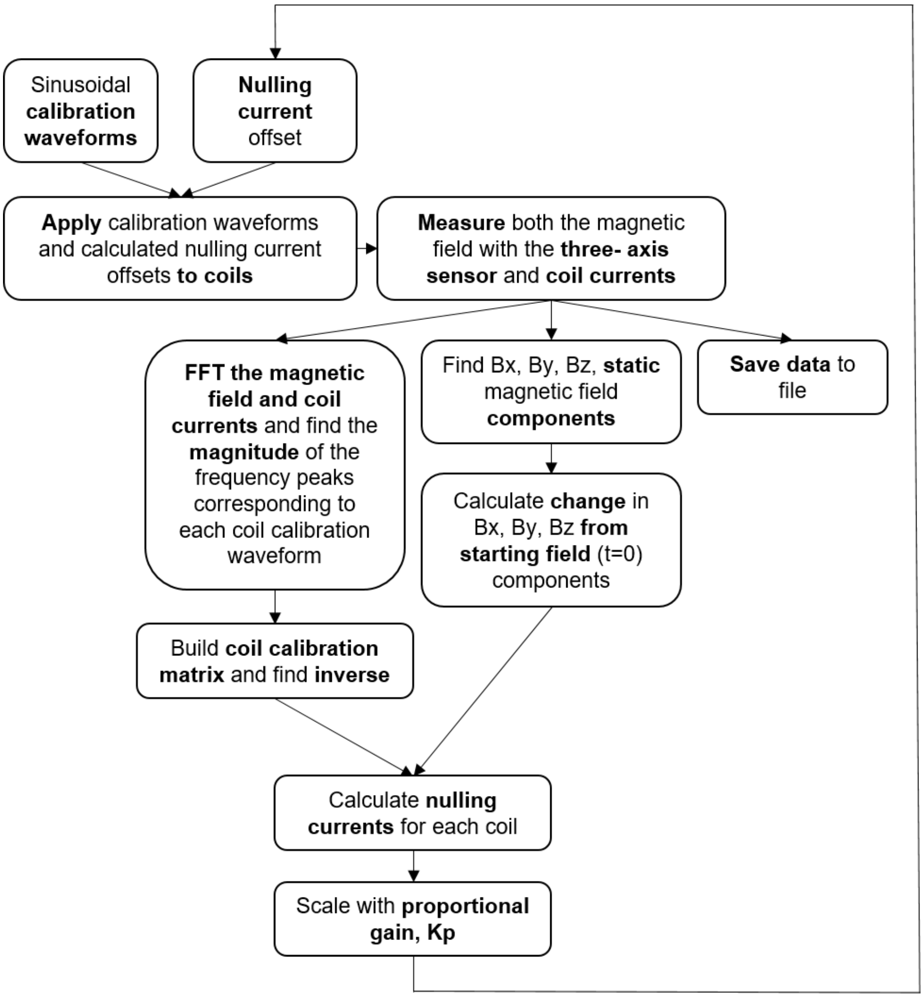

Figure 5.6: *A flow chart outlining the continuous calibration and nulling process to be implemented using LabVIEW.*

5.6.3 LabVIEW structure

The program consisted of six parallel while loops which ran simultaneously, with *Queue*[1] and *Notifier*[2] operators in place to allow data transfer between the loops. User interaction with the front panel, such as pressing buttons, were managed using an Event Handler. Screenshots of the front panel (Figure 6.1) and block diagrams (Figures 6.2 and 6.3) are included in Appendix A.

Each while loop executed a different task:

(I) Input Voltages

---

[1] Queues are first-in/first-out buffered lists, where data elements are 'enqueued' into a buffer and 'dequeued' out of the buffer.

[2] Notifiers are used to communicate between two parts of the same program (i.e. communication between two loops).

(II) Output Voltages

(III) Calculate Calibration Matrix

(IV) Calculate DC background field

(V) Proportional Controller

(VI) Save Data to File

as described in the following sections.

5.6.3.1 (I) Input Voltages

The voltages recorded by the DAQ input module were read into the program. The data included the voltages recorded by the fluxgate magnetometer and measurements of the voltage across the in-series resistors. The data were read with a sample rate, F_s and number of samples, N set specifically to ensure that for each iteration of (I) $T=\frac{1}{\delta f}$ seconds of data are measured and queued (see Section 5.5.2).

Sensor data enqueued to (III) and (IV) and (VI). Resistor data enqueued to (III) and (VI).

5.6.3.2 (II) Output Voltages

Notifier from (V) obtained for current offsets, $I_{applied}$.

The output voltages to each coil were formed of a sinusoidal waveform for calibration, $I_{calibration}$ (as described in Section 5.5), which was continuously output to each coil, and an additional DC offset to null the background field. The frequency, f_n of each calibration waveform could be set by the user. The currents to the coils were output as voltages via a DAQ output module.

5.6.3.3 (III) Calculate Calibration Matrix

Sensor data dequeued from (I). Resistor data dequeued from (I).

The calibration matrix was calculated as described in Section 5.5 using the most recent sensor measurements and resistor voltages. The inverse of the calibration matrix, $\boldsymbol{A}^{+}$ was found.

Inverse calibration matrix, $\boldsymbol{A}^{+}$ sent as notifier to (V). Calibration matrix, $\boldsymbol{A}$ sent as notifier to (VI).

5.6.3.4 (IV) Calculate DC Background Field

Sensor data dequeued from (I).

During the first iteration, the average magnetic field was calculated along each sensitive axis to find the initial DC field components, B_x, B_y, and B_z.

Initial field components, $\boldsymbol{b_0(t=0)}$ saved as a local variable.

On all other subsequent iterations, the average magnetic field was calculated and the change in field from $\boldsymbol{b_0(t=0)}$, $\Delta\boldsymbol{b}$ was found.

Change in magnetic field, $\Delta\boldsymbol{b}$ sent as notifier to (V).

5.6.3.5 (V) Proportional Controller

Notifier of inverse calibration matrix, $\boldsymbol{A}^+$ obtained from (III). Notifier of change in magnetic field, $\Delta\boldsymbol{b}$ obtained from (IV).

The nulling currents were calculated and scaled using a proportional gain, K_p (tuned by the user) as described in Section 5.3. Equation 5.13 describes the currents to be applied to null the change in field, $\Delta\boldsymbol{b}$. A constraint on the current was applied to ensure that the voltages output from the DAQ module did not exceed the working range of (± 10 V).

Current offsets, $\boldsymbol{I_{applied}}$ sent as notifier to (II).

5.6.3.6 (VI) Save data to file

Sensor data dequeued from (I). Resistor data dequeued from (I). Notifier of Calibration matrix data, $\boldsymbol{A}$ obtained from (III).

All sensor voltages and voltages measured across the in-series resistors were saved to a tdms[3] file. The calibration matrices calculated during the experiment were also saved to a separate tdms file.

---

[3] A tdms or 'technical data management solution' format where data and metadata are saved as a binary file. This enables high-speed processing compared to text file alternatives which have comparatively slow processing times.

5.6.4 Program table

LabVIEW PROGRAM - PROCESSING AND FIELD CONTROL

(I) Input Voltages

- Read $T = \frac{1}{\delta f}$ seconds of sensor and resistor voltage data from DAQ input module.
- Queue sensor data: (I) → (III)/(IV)/(VI).
- Queue resistor data: (I) → (III)/(VI).

See Section 5.6.3.1

(II) Output Voltages

- Obtain current offset notifier, $\boldsymbol{I_{applied}}$ from (V).
- Continuously output calibration waveforms, $\boldsymbol{I_{calibration}}$ to coils at chosen frequencies, f_n.
- Add additional DC offset, $\boldsymbol{I_{applied}}$ to $\boldsymbol{I_{calibration}}$.

See Section 5.6.3.2

(III) Calculate Calibration Matrix

- Dequeue sensor data from (I).
- Dequeue resistor data from (I).
- Calculate calibration matrix, $\boldsymbol{A}$ and inverse, $\boldsymbol{A}^+$.
- Send $\boldsymbol{A}$ notifier: (III) → (VI).
- Send $\boldsymbol{A}^+$ notifier: (III) → (V).

See Section 5.6.3.3

(IV) Calculate DC Background Field

- Dequeue sensor data from (I).
- First iteration: calculate the average DC field components, $\boldsymbol{b_0}$ and save as *local variable*.
- All other iterations: calculate the average DC field components and find change in field, $\Delta\boldsymbol{b}$ from $\boldsymbol{b_0}$.
- Send $\Delta\boldsymbol{b}$ notifier: (IV) → (V).

See Section 5.6.3.4

(V) Proportional Controller

- Obtain change in field notifier, $\Delta\boldsymbol{b}$ from (IV).
- Obtain inverse calibration matrix notifier, $\boldsymbol{A}^+$ (V).
- Calculate nulling currents, $\boldsymbol{I_{applied}}$.
- Send $\boldsymbol{I_{applied}}$ notifier: (V) → (II).

See Section 5.6.3.5

(VI) Save data to file

- Dequeue sensor data from (I).
- Dequeue resistor data from (I).
- Obtain calibration matrix notifier from (III).
- Save sensor data, resistor data, and calibration matrix data to tdms file.

See Section 5.6.3.6

5.7 Experiments

The LabVIEW program described in Section 5.6 was implemented and tested with two stationary sensor experiments and two moving sensor experiments. For a stationary sensor, the response of the system to a step change in the magnetic field and also a time varying magnetic field were investigated. The controller was also tuned in both cases by varying the proportional gain, K_p. Experiments in which the sensor was translated or rotated were also carried out and the ability of the system to null the change in magnetic field seen by the magnetometer during movement was shown.

For all of the experiments described below, the square electromagnetic coils were set up as described in Section 5.4. The coil calibration frequencies for coils, 1 to 6 were set at 10 Hz, 20 Hz, 30 Hz, 40 Hz, 50 Hz, 60 Hz respectively (δf=10 Hz and hence T_{min}=0.1 s) and the waveforms were output to the coils at a rate of 10,000 Hz. The sensor data and resistor data were sampled at 2,000 Hz.

5.7.1 Response to an applied field change

Firstly, the value of the proportional gain, K_p was varied in order to tune the proportional controller and determine for which K_p value the system was most stable. To test the stability of the controller, a DC step in the magnetic field was generated and the response of the controller to null the change in magnetic field was observed. For the system to be classed as stable, the change in magnetic field must be nulled quickly, with minimal overshoot of the magnetic field past zero.

5.7.1.1 Experiment

A 20 nT DC step in magnetic field was generated using a Tektronix AFG 3102 signal generator (Tektronix, Beaverton, OR) connected to a small circular coil mounted to the centre of face ‘2’ inside the MuBin (see Figure 5.1). A wooden board at approximately half the height of the box was used to position the sensor at the centre of the shield, such that the B_x sensitive axis was pointing along the axis of the small coil.

The proportional gain of the controller was varied such that K_p = 0, 0.15, 0.1, 0.09, 0.085, and 0.05. With the LabVIEW program running, the 20 nT step in the magnetic field was applied after around 10 seconds and the response of the controller, i.e. the magnetic field measured by the sensor, was recorded.

5.7.1.2 Results

The responses of the controller to the step in magnetic field for different K_p values are shown in Figure 5.7.

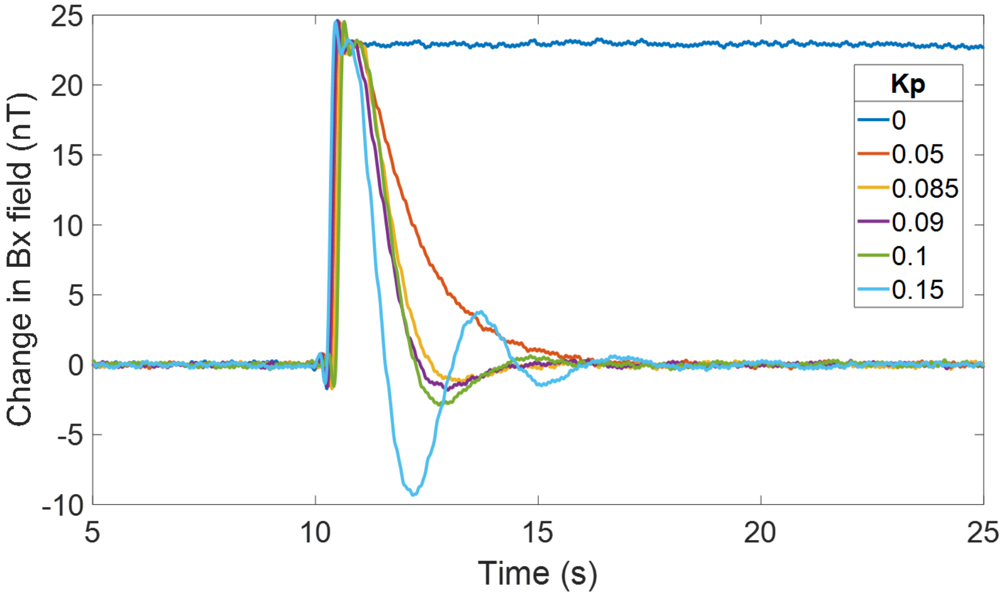

Figure 5.7: *A graph showing the response of the proportional controller over 20 seconds to a step change in the magnetic field for different values of the proportional gain,* K_p*, where* $K_p = 0$ *(dark blue), 0.05 (red), 0.085 (yellow), 0.09 (purple), 0.1 (green), 0.15 (light blue). Only the* B_x *component is shown. The step change in the magnetic field occurs at* $\approx$ *10 s, after this time the proportional controller works to reduce the change in magnetic field to zero.*

When $K_p = 0$, the proportion of the current being applied is 0, therefore no nulling currents are being applied to the coil. Subsequently, there is no magnetic field cancellation and the magnetic field remains at around 23 nT after the field change is applied. At lower gains, $K_p = 0.05$, the controller takes approximately 5 seconds to bring the change in magnetic field to 0 nT. As K_p increases, nulling gets faster but there is a slight undershoot. When the gain is too high ($K_p = 0.15$) the system becomes unstable and the magnetic field oscillates about 0 nT before stabilising to 0 nT after ~8 s.

5.7.1.3 Discussion

The controller responses to a DC step in the magnetic field show good comparisons to controller responses in the literature for different proportional gain values (Skogestad [2005]). When the feedback controller is tuned correctly, the step in magnetic field is nulled quickly with minimal overshoot of the field past the set point (in this case zero field). The response also has a quick settling time. The results from Figure 5.7

determined that a K_p value of around 0.09 should be used to tune the controller in subsequent experiments.

5.7.2 Response to an AC field

5.7.2.1 Experiment

The experiment described in Section 5.7.1 was repeated but with time-varying interference fields, with a narrower range of values of K_p informed from previous results. The frequency of the interference field was varied such that, f = 0.01 Hz, 0.05 Hz, 0.1 Hz, 0.2 Hz, and 0.5 Hz, while the amplitude of the interference field was $\approx$ 20 nT. K_p was set to 0, 0.09, 0.15, and 0.2 for each of the interference frequencies.

After setting the gain the LabVIEW program was switched on. After 10 seconds, the interference field was applied and the response of the controller was recorded for: 120 seconds for f = 0.01 Hz and 0.05 Hz, and 60 seconds for f = 0.1 Hz, 0.2 Hz, and 0.5 Hz.

5.7.2.2 Analysis

For each data set, a Fast Fourier Transform of the magnetic field data was taken and the magnitude of the interference field at each relevant frequency was found from the peaks in the FFT. The vector norm of the magnetic field without nulling ($K_p = 0$) and with nulling (K_p = 0.09, 0.15, and 0.2) was calculated. A shielding factor was then estimated for each interference frequency for the three different gains. Example data sets are included in Appendix B.

5.7.2.3 Results

Figure 5.8 shows how well the controller was able to null time-varying interference fields with frequencies between 0.01 Hz and 0.5 Hz. Shielding factors above the dashed red line show that the system is able to null the change in magnetic field. Shielding factors below the red dashed line, i.e. when SF $<$ 1, indicate that the field is not being nulled. The response of the system with different proportional gain values, K_p = 0.09, 0.15, and 0.2, are shown in blue, red, and yellow respectively.

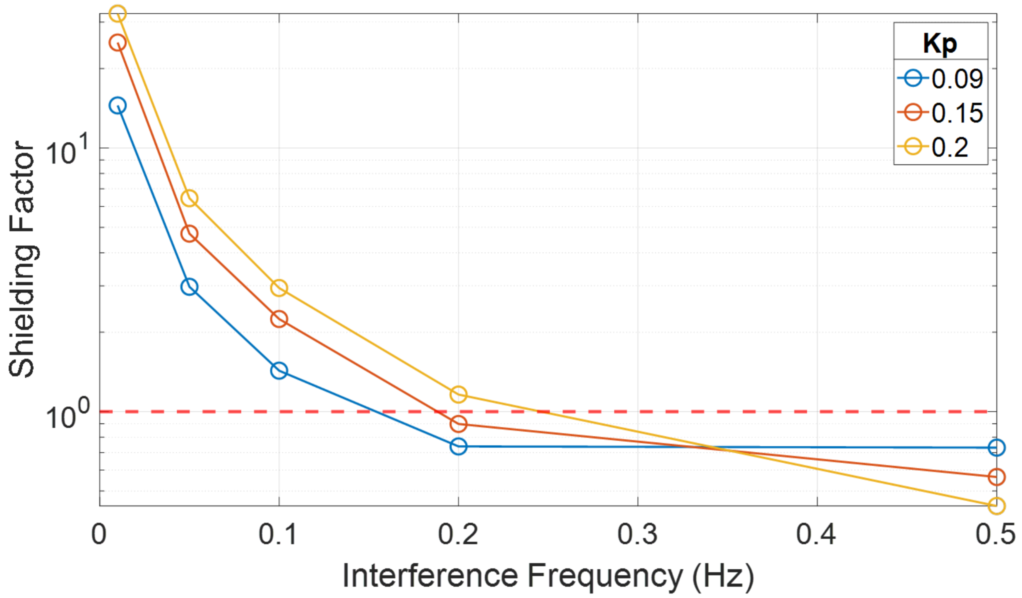

Figure 5.8: *A plot showing the shielding factors achieved using a proportional controller to null time-varying sinusoidal interference fields for* $f = 0.01$ *Hz, 0.05 Hz, 0.1 Hz, 0.2 Hz and 0.5 Hz. Different values of the proportional gain,* K_p *were used to check the stability of the system: 0.09 (blue), 0.15 (red), 0.2 (yellow). A red dashed line indicates a shielding factor of 1- below this line there is no improvement with nulling.*

The largest shielding factor achieved was ≈ 12, for interference fields of 0.01 Hz, with a proportional gain of 0.2 (yellow plot). The shielding factor decreases to ≈ 3 as the frequency of the interference field increases to 0.1 Hz. Above 0.2 Hz the shielding factors are less than 1 (red dashed line) showing that the controller is not nulling the interference field.

5.7.2.4 Discussion

For interference frequencies below 0.2 Hz the controller is able to null the changing magnetic field and hence the controller can be described as having a ‘bandwidth’ of less than 0.2 Hz. It can be seen that a proportional gain of 0.2 (yellow trace) is the most effective value of K_p for time-varying interference fields in the frequency range investigated here.

5.7.3 Response to sensor translation

Continuous magnetic field cancellation was then implemented over a moving fluxgate magnetometer. To enable repeatability, controlled movements of the sensor inside the MuMetal box were carried out. The experiment was repeated with different K_p values to tune the proportional controller and bring the change in magnetic field to zero quickly and with little overshoot.

5.7.3.1 Experiment

The magnetometer was taped to the end of a wooden metre ruler to allow movement of the sensor through the hole in the side of the box. A track made of sheets of perspex was used to help guide the ruler during movement (see track marked with green lines in Figure 5.9). The track, which ran between faces 5 and 6 of the MuBin (see Figure 5.1), was placed on the wooden platform as described in Section 5.5.4.

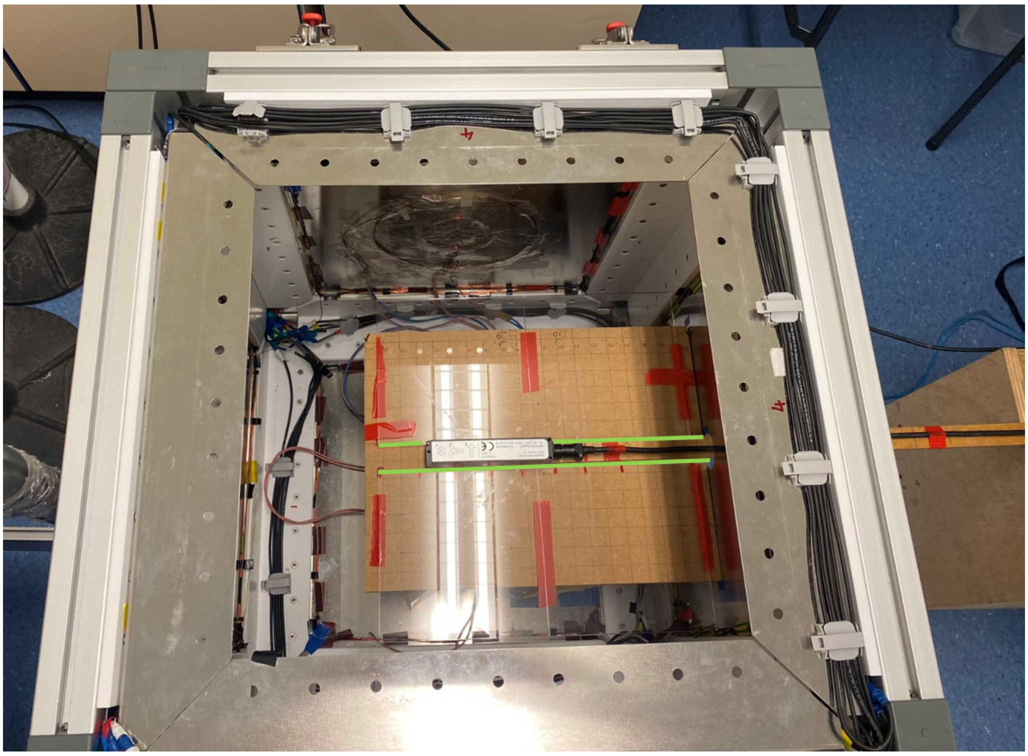

Figure 5.9: *A photograph showing the inside of the MuBin set up for a translation experiment. Perspex rectangles were fixed to a wooden board to create a track along a line between faces 5 and 6 of the MuBin (shown with green lines). The SENSYS was taped to a metre ruler which enabled it to slide along the track through the hole in the side of the MuBin. Markings on the ruler indicated how far the SENSYS was along the track. A schematic diagram of the set-up is shown in Figure 5.10.*

Each movement was a slow, steady, translation of 4cm along the track every 10 seconds. Electrical tape was used to mark out fixed positions every 4 cm along the meter ruler. These marks were used to indicate how far to move the sensor, by aligning the edge of the tape with the edge of the hole in the box. A diagram showing the positions of the sensor during the translation experiment are shown in Figure 5.10.

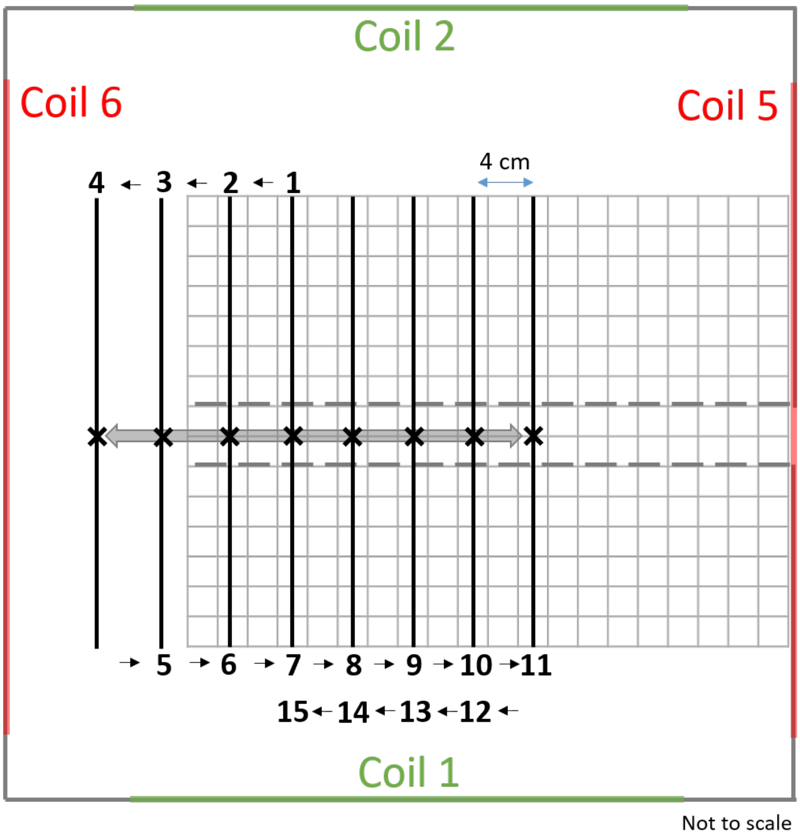

Figure 5.10: *A schematic diagram showing the positions of the sensor inside the MuBin during the translation experiment. The sensor could move forwards and backwards along the track (indicated by the grey dashed lines) between coils 5 and 6. The black crosses (separated by 4 cm) indicate the position of the sensor as it was translated- starting at position 1 and ending at position 15.*

A stopwatch was used to time the movements. A first experimenter used a verbal cue every 10 seconds to indicate to a second experimenter when to move the sensor. As soon as the next position was reached the experimenter stopped moving the sensor and waited for the next "Go". This process is outlined below:

1. "Go!"
2. Slowly move sensor (4 cm) to next position and stop
3. Wait for next indication to start moving
4. Repeat.

The sensor movements were: starting at the centre of the box (position 1, 0 cm), moving towards coil 6 (position 4, + 12 cm) and then backwards towards coil 5 (position 11, − 28 cm), and finally moving back towards the centre of the box (position 15, + 16 cm).

This experiment was repeated four times. Firstly with K_p=0, to measure the change in magnetic field without nulling, and further repeats with $K_p = 0.09$, 0.15, and 0.12 to see how well the program nulled the change in field during sensor movement.

Throughout the experiment, the magnetic field measured by the sensor and the voltage across the coil in-series resistors were recorded. The calibration matrices calculated by the LabVIEW program were also recorded.

5.7.3.2 Analysis

The sensor data were scaled using the sensor gain, (0.1 V/μT) and the resistor voltages were converted to current using $I = \frac{V}{R}$. Both the sensor and current data were low-pass filtered at 3 Hz to remove the high frequency waveforms used for calibration. The filtered data was then zero corrected to an average baseline taken in a window between 1 and 9 seconds before movement occurred.

The change in magnetic field was plotted for each sensor axis with nulling off (i.e. when K_p= 0) and with nulling on (i.e. when K_p= 0.09, 0.15, 0.12). The calibration matrix was calculated to show how it changed as the sensor moved along the track. The field per unit current for each coil over time was also calculated.

5.7.3.3 Results

The response of the controller to the change in magnetic field due to sensor movement is shown in Figure 5.11. Each plot shows how the B_x component of the magnetic field was nulled for different values of the proportional gain (red trace), compared to when no nulling currents were applied when K_p= 0 (blue trace). It can be seen that after the sensor was moved, (approximately every 10 seconds) the step in magnetic field was nulled and brought back down to zero for each case. However, comparing the response of each system, Figure 5.11a, where K_p= 0.09, shows the most effective nulling. The change in field is quickly brought back to zero with little to no overshoot, compared to Figures 5.11b and 5.11c, where the field overshoots and oscillates about zero field.

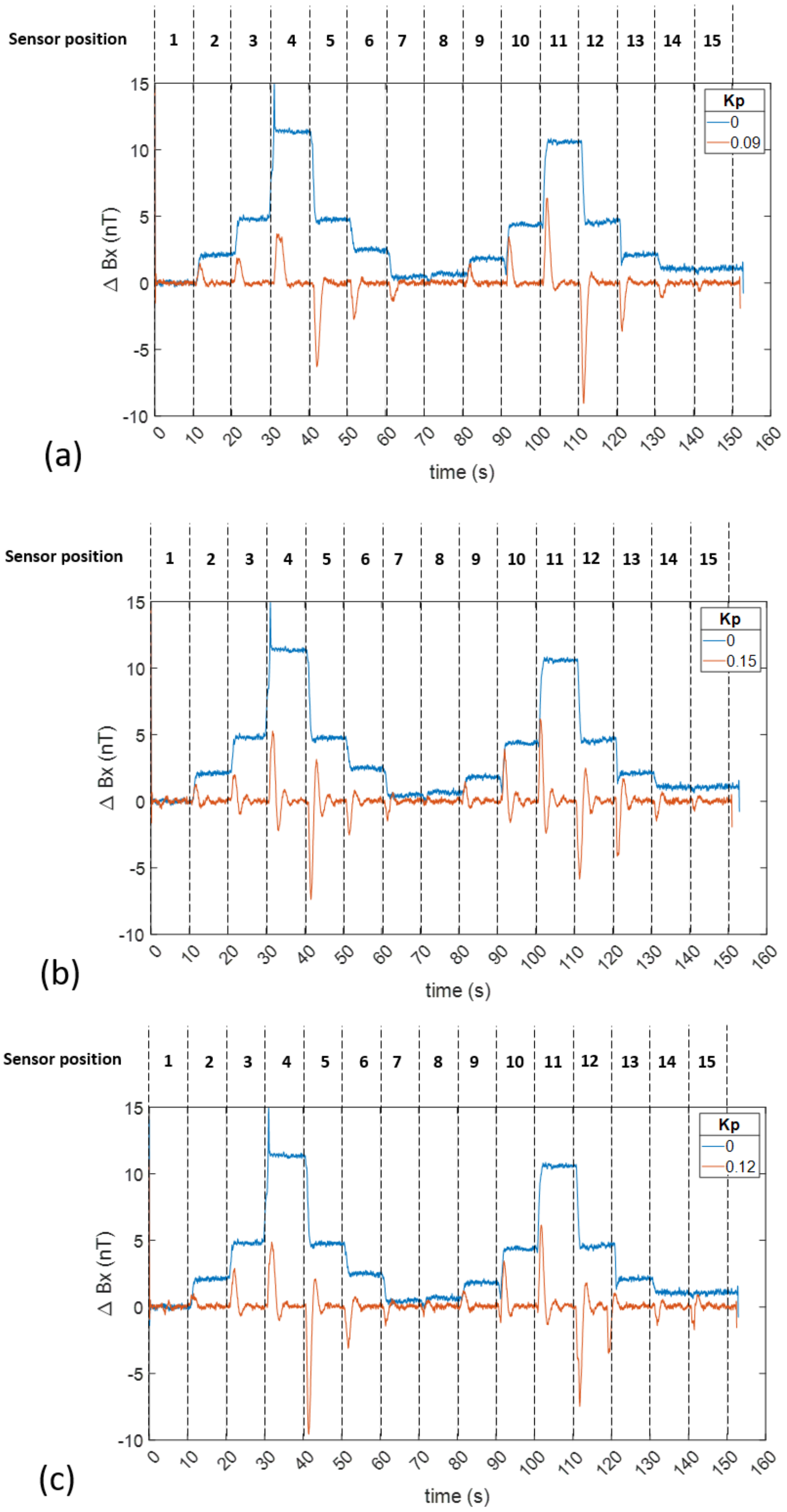

Figure 5.11: *Results of the translation experiment- nulling the magnetic field over a moving sensor with different proportional gains, K_p. The change in the B_x component of the magnetic field measured by the SENSYS is plotted. The movement of the sensor to a position on track is indicated by the grey dashed vertical lines imposed on the graph. See Figure 5.10 for a diagram of the sensor positions. The change in field during translation when the nulling is switched off or K_p=0 is shown in blue, and with the nulling on is shown in red. Each figure shows the change in field with nulling when: (a) K_p=0.09, (b) K_p=0.15, and (c) K_p=0.12.*

Figure 5.12 shows the response of the system when the controller is tuned with a gain of K_p=0.09 (nulling currents on). The evolution of the calibration matrices for K_p=0.09 is also shown. With nulling currents off (when K_p=0) there is a change in the magnetic field as the sensor moves, similar to a step in the magnetic field. The biggest change can be seen in the B_z component of the magnetic field (yellow trace)- along the axis of translation. When the currents are turned on (i.e. the controller gain is changed from 0 to 0.09), the magnetic field is brought back down to zero after each movement. However, there is still an artefact in the data after each movement due to the response of the controller.

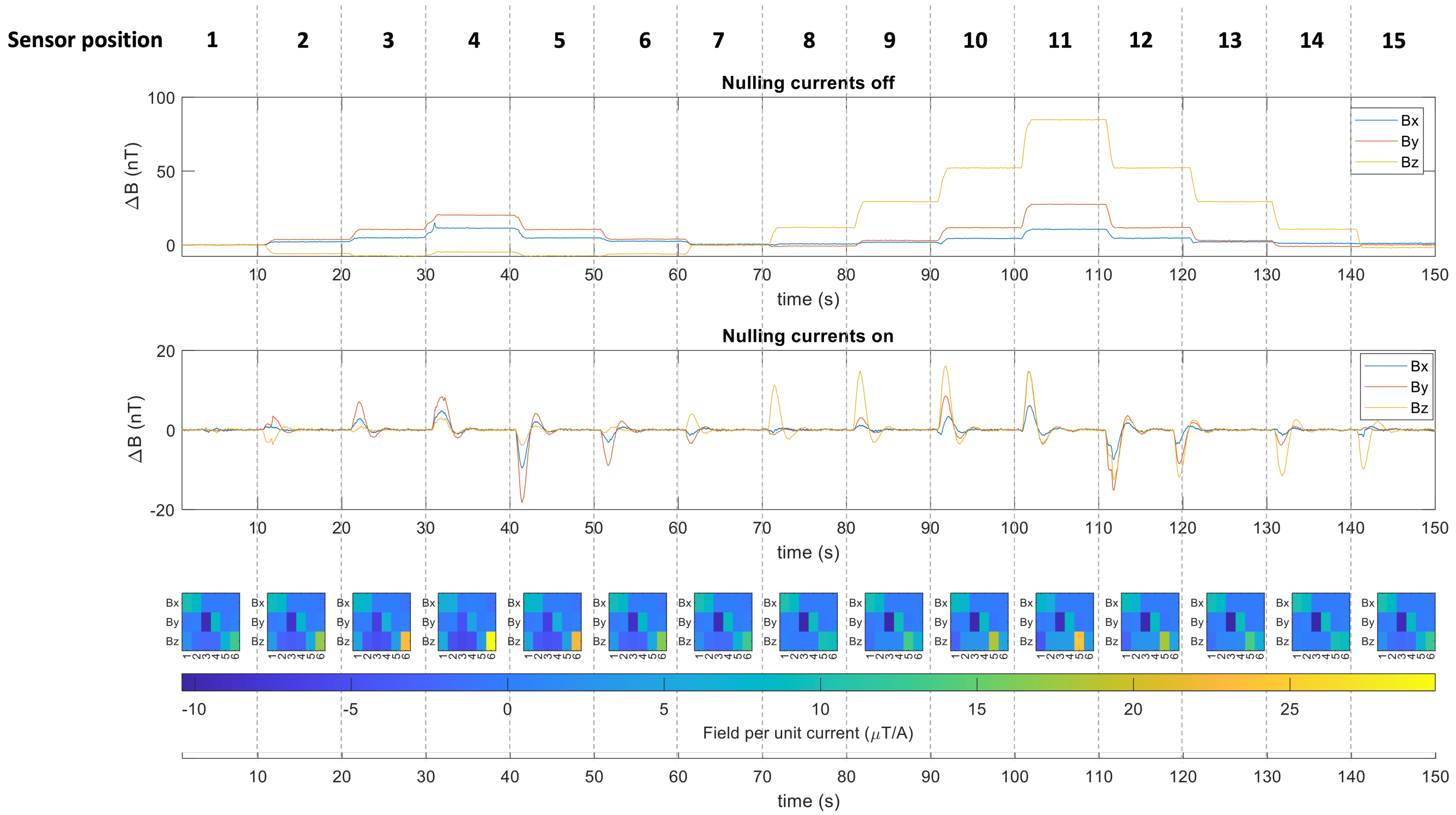

Figure 5.12: *Translation experiment results for K_p=0.09. Plots showing the change in magnetic field, ΔB when nulling is off (top) and nulling is on (middle) and also how the calibration matrix varies as the sensor translates (bottom). Each 10 second movement window is shown via the grey dashed vertical lines. The final sensor position (refer to Figure 5.10) during each movement window is labelled. The line graphs show the change in field with no nulling, compared to when the nulling currents are applied to the coils. The magnetic field components (nT) B_x, B_y, B_z are shown in blue, red and yellow, respectively. The calibration matrix values ($\mu T/A$) taken from the centre of each time window are plotted as colour maps.*

To show how the calibration matrix varies due to movement of the sensor in the experiment, the calibration matrix at the centre of each movement time window was plotted. Due to the symmetric nature of the system, and the alignment of sensitive axes of the sensor along axes between a pair of electromagnetic coils, the dominant field changes are produced by the coils that lie along the diagonal of the calibration matrix.

One can see that the biggest changes in the field per unit current are for (5, B_z) and (6, B_z), due to the sensor translating between coils 5 and 6, and the B_z component of the sensor pointing in the direction along the axis between the two coils. At the centre of the box (between 0 and 10 seconds) the contribution from the two coils is roughly equal. As the sensor moves towards coil 6 and away from coil 5, the contribution of the field per unit current from coil 6 increases (between 10 and 40 seconds). Between 60 and 70 seconds, as the sensor is pulled back towards the hole in the side of the box towards coil 5, the field per unit current is similar across coils as the sensor moves back through the centre. Between 90 and 100 seconds, the contribution from coil 5 begins to increase as the sensor moves closer to the coil before ending back at the centre of the box (140 and 150 seconds).

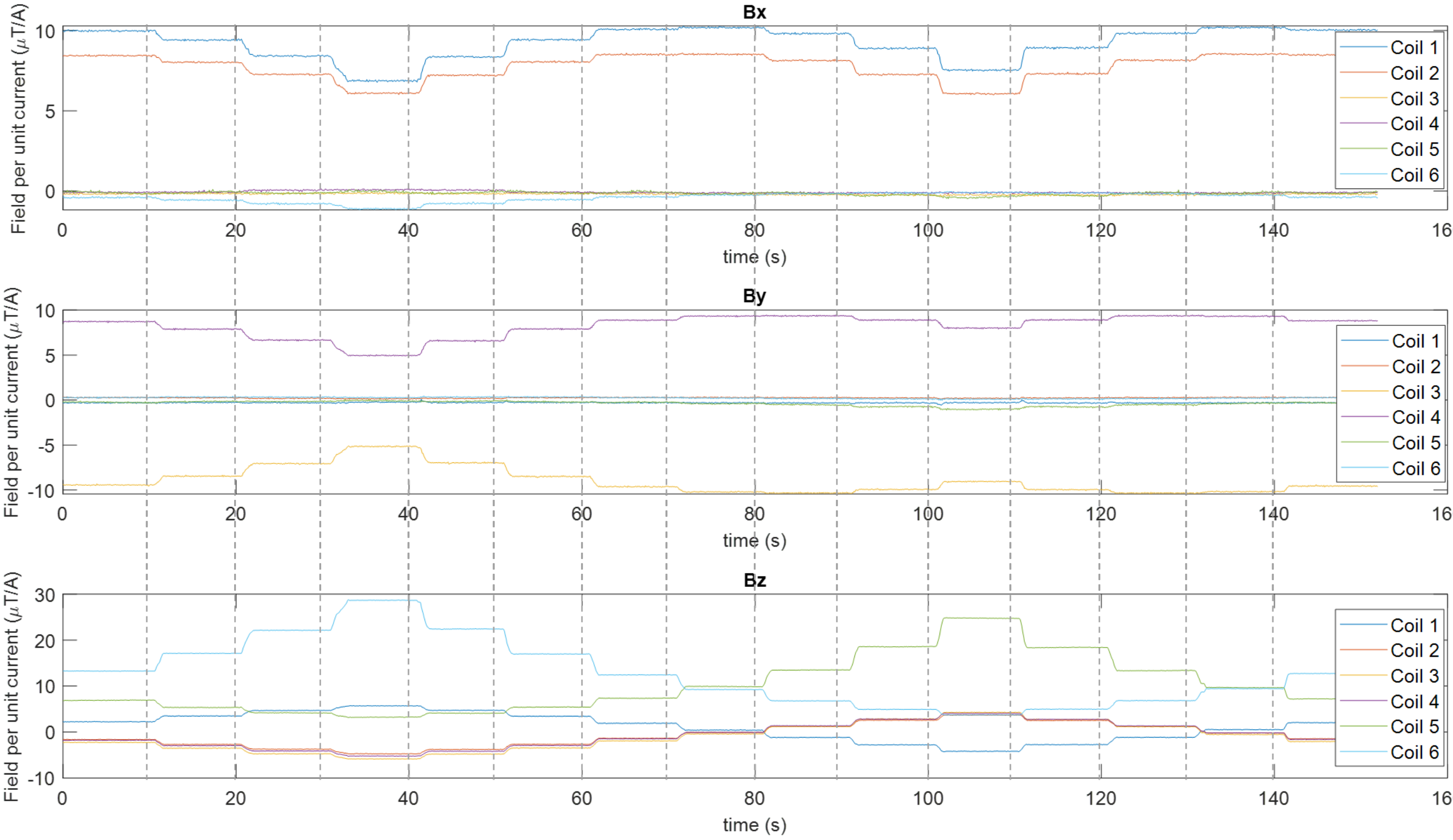

Figure 5.13: *Line plots showing how the field per unit current ($\mu T/A$) produced by each coil varied over the entire translation experiment for K_p=0.09. The B_x (top), B_y (middle), and B_z (bottom) magnetic field components per unit current are plotted for coil 1 (dark blue), coil 2 (red), coil 3 (yellow), coil 4 (purple), coil 5 (green), and coil 6 (light blue).*

A detailed plot showing how each element of the calibration matrix changes during the experiment is provided in Figure 5.13. The plots show how much each coil contributes to the B_x, B_y, and B_z components of the magnetic field per unit of current. The form of these plots is similar to the form of the un-compensated ('Nulling currents off') measurement shown in Figure 5.12.

5.7.3.4 Discussion

The results above show that the program can update the calibration matrix and apply nulling currents during a translation experiment in order to reduce the change in magnetic field at the position of the sensor.

However, the data also show that whilst the calibration matrix and coil currents were able to update during the experiment, the program needs to be faster to reduce the artifact in the magnetic field during the 10 second movement window. This could be done by increasing the frequency separation between the frequencies assigned to each coil, hence reducing the measurement time needed to resolve the peaks in the FFT, and ensuring that the calibration matrix could be calculated at a faster rate.

Further experiments would involve recording the time taken to process measurements at each stage within the LabView program to check that each section was running optimally and that the response of the program was as fast as possible.

5.7.4 Response to sensor rotation

A final experiment was carried out in order to test how well the system nulled the magnetic field over the sensor during a 360° rotation about the z-axis of the sensor.

5.7.4.1 Experiment

Using the same experimental set up described in Section 5.7.3.1, the sensor was positioned at the centre of the box and rotated clockwise about the z-axis of the sensor (see Figure **??**). The rotations were carried out with controlled movements consisting of a clockwise rotation of 90° every 10 seconds. The sensor was taped to the meter ruler so that the sensor could be rotated through the hole in the side of the box. Different proportional gain values, K_p =0, 0.06, 0.09, 0.12, 0.15, were used to test and tune the controller.

5.7.4.2 Analysis

Analysis was carried out as described in section 5.7.3.2.

5.7.4.3 Results

The response of the controller with different proportional gains is shown in Figure 5.14. For $K_p = 0.06$ (Figure 5.14a), the magnetic field smoothly reduced to zero after each 90° rotation. As the gain increased from 0.09 to 0.15 (see Figures 5.14b to 5.14d respectively), the magnetic field nulling became increasingly unstable with oscillations about zero field. For $K_p = 0.15$, these oscillations did not stabilise before the next rotation.

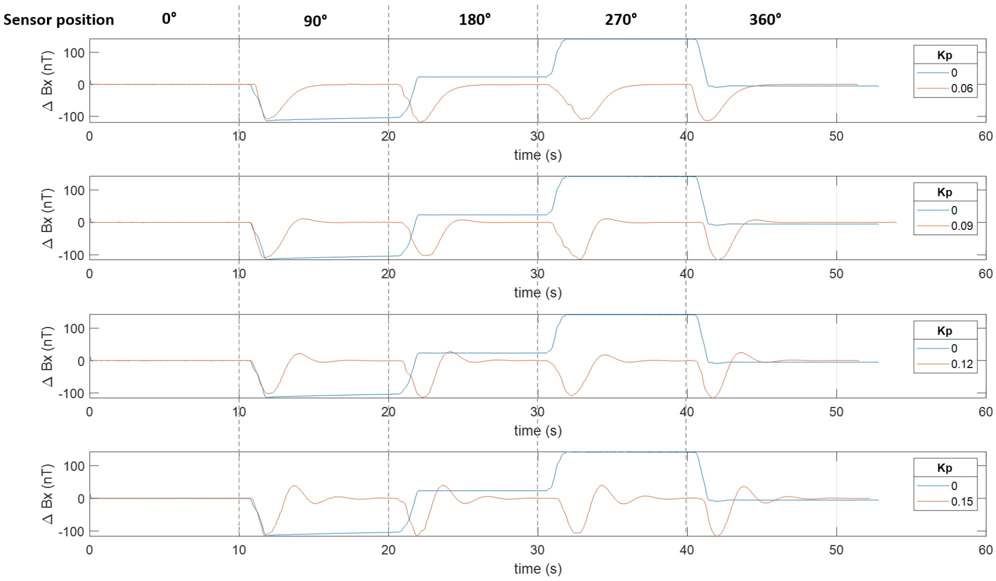

Figure 5.14: *Rotation experiment, varying K_p- results showing the change in the B_x component of the magnetic field (nT) during a full 360° rotation about the z axis of the sensor, when nulling with different proportional gains. (From top to bottom) K_p=0.06, 0.09, 0.12 and 0.15. 'Nulling off' is shown in blue (K_p=0) and 'nulling on' is shown in red. The movement windows are marked with grey dashed vertical lines, and the sensor position after each movement is indicated at the top of the figure.*

Figure 5.15 shows how the magnetic field changes during rotation both without nulling and with nulling (where the proportional gain was set to 0.09). As the sensor was rotating about the z sensitive axis, the largest changes in magnetic field are in B_x (blue trace) and B_y (red trace). When the nulling currents are switched on, there is a magnetic field artefact due to the response of the controller as seen in the translation results (see Section 5.7.3.3). However, once the system stabilises, the magnetic field components are nulled to approximately 0 nT.

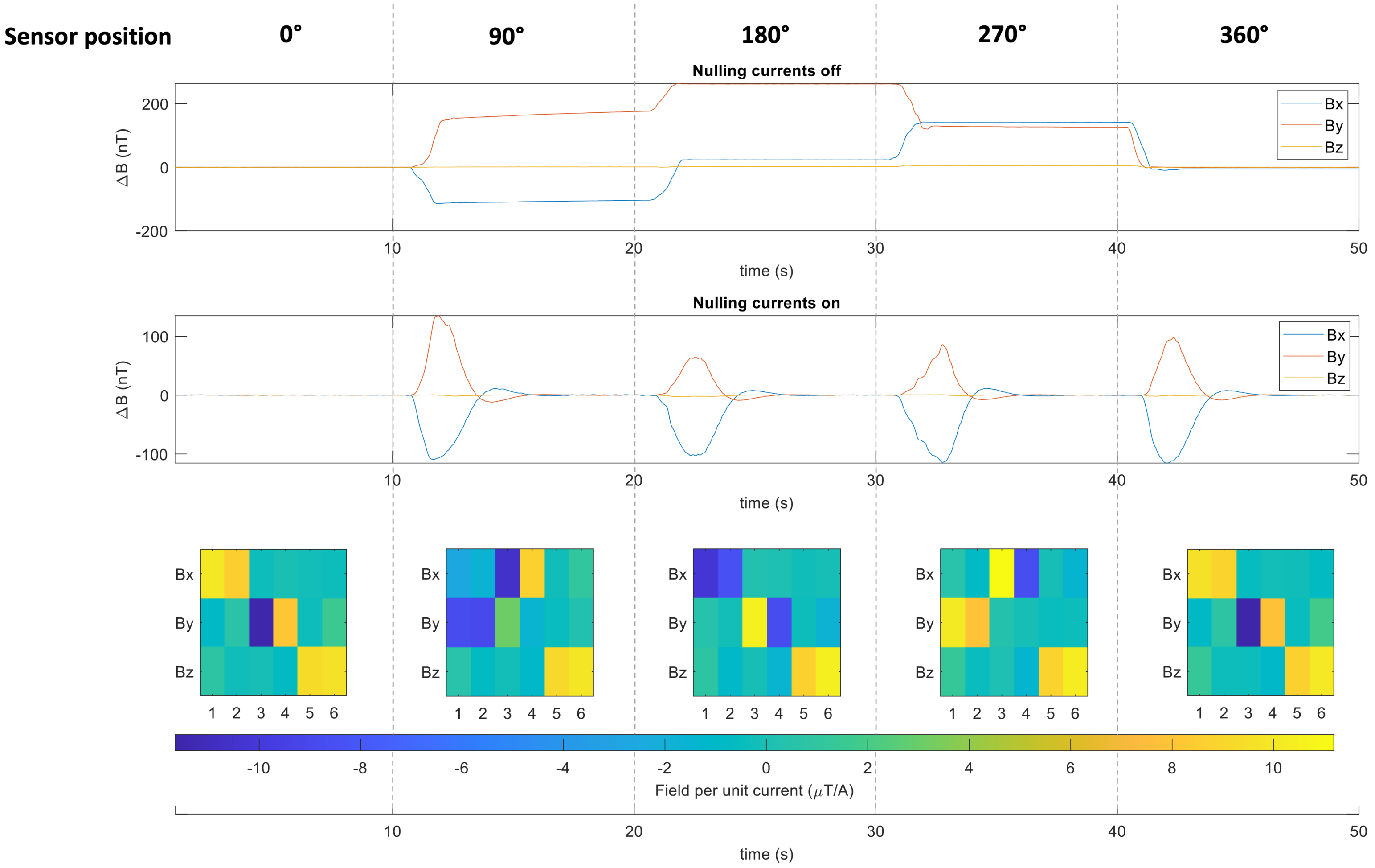

Figure 5.15: *Rotation experiment,* K_p*=0.09. Plots showing the change in magnetic field,* ΔB *with nulling off (top), nulling on (middle), and and also how the calibration matrix varies as the sensor rotates (bottom). Each 10 second movement window is shown via the grey dashed vertical lines and the position of the sensor at the end of each movement window is shown at the top of the figure. The graphs show the change in field (nT) with no nulling, compared to when the nulling currents are applied to the coils. The magnetic field components* B_x*,* B_y*,* B_z *are shown in blue, red, and yellow respectively. The calibration matrix values (*$\mu T/A$*) taken from the centre of each time window are plotted as heat maps.*

The calibration matrix at the centre of each movement window was plotted. As the sensor was rotating about the B_z sensor axis, there was no change in the contribution of the magnetic field per unit current from coils 5 and 6 throughout the measurements. At the start of the experiment (between 0 and 10 seconds), the directions of B_x and B_y were pointing between coils 1 and 2, and 3 and 4 respectively. It can be seen that when the sensor was rotated 90° the pair of coils contributing to the field per unit current for each sensor axis flips. This happens four times, before the sensor returns its initial starting position.

Figure 5.16 shows detailed plots of how each element of the calibration matrix changes during rotation. These plots mimic the form of the uncompensated magnetic field shown in Figure 5.15.

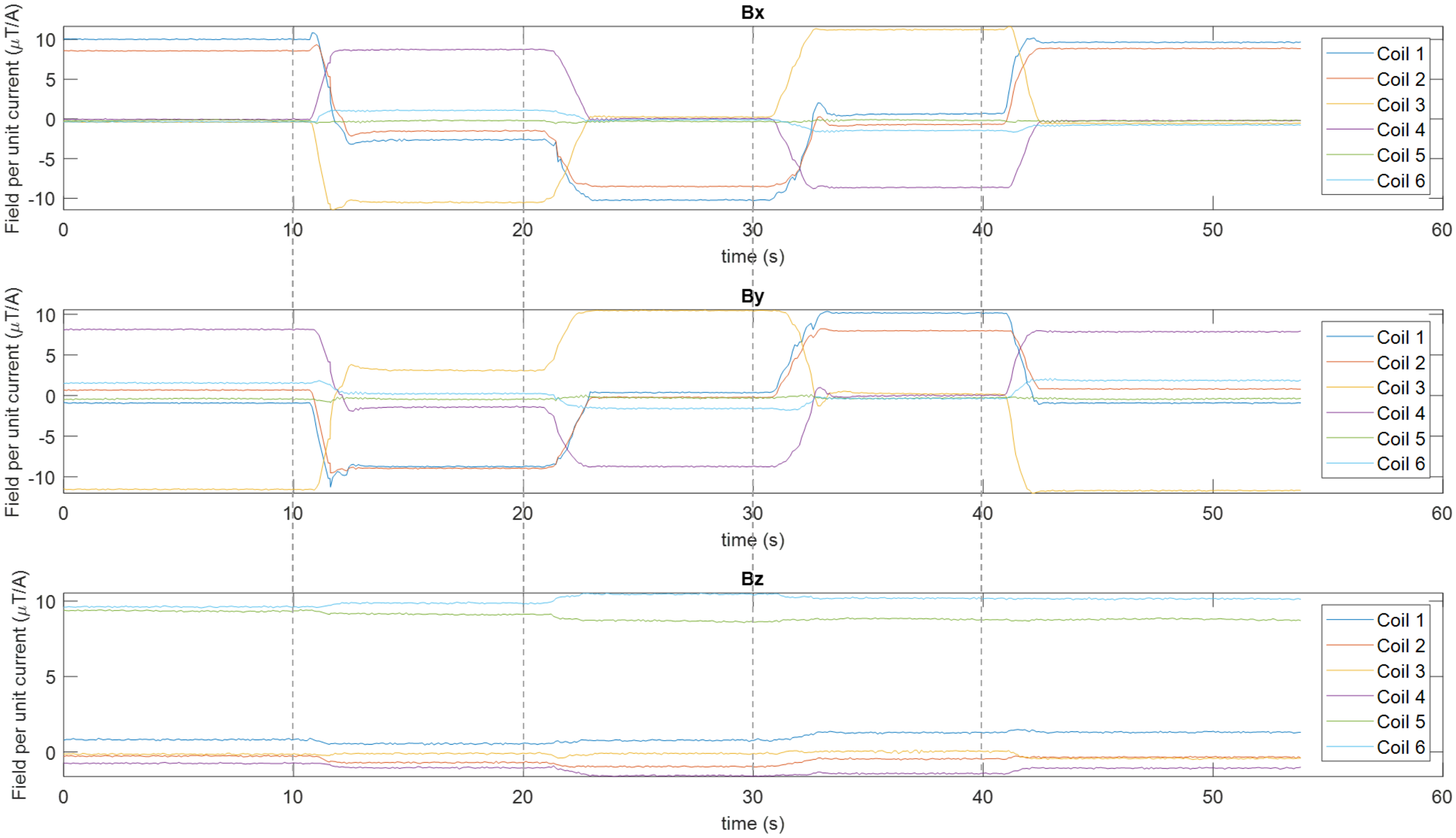

Figure 5.16: *Line plots showing how the field per unit current (μT/A) produced by each coil varied over the entire rotation experiment for* K_p*=0.09. The* B_x *(top),* B_y *(middle), and* B_z *(bottom) magnetic field components per unit current are plotted for coil 1 (dark blue), coil 2 (red), coil 3 (yellow), coil 4 (purple), coil 5 (green), and coil 6 (light blue).*

5.7.4.4 Discussion

The response of the system and ability of the program to null the change in magnetic field during a rotation are similar to those seen during a translation. There is a significant artefact during movement which stabilises once the sensor has stopped moving. This could be improved by reducing the time taken to calculate the calibration matrix (as described in Section 5.7.3.4).

5.8 Discussion and future work

5.8.1 Magnetic field cancellation for OPM-MEG

The work described in this chapter was motivated by a need for magnetic field cancellation that would enable movement of participants during an OPM-MEG experiment. A limiting factor in previous magnetic field nulling work was that calibration of the electromagnetic coils was done before the experiment, and hence the nulled region could not move with the participant.

Here it has been shown that by driving electromagnetic coils with a sinusoidal calibration current, each with its own distinct frequency, it is possible to update the calibration matrix during the experiment. Therefore, it is possible to null the magnetic field over the sensor whilst it moves within the space between the electromagnetic coils.

Whilst continuous calibration is an exciting advancement, scaling up this approach to null over an OPM array will be challenging. Firstly, the number of electromagnetic coils used to null the magnetic field inside an OPM-optimised MSR is much larger than the six coils used in the MuMetal box above. The OPM-MEG matrix coil system in Nottingham has 48 independently driven electromagnetic coils (Holmes et al. [2023a]). In order to continuously calibrate this system at the speeds used in the translation and rotation experiments described previously in this chapter, the bandwidth of the calibration system would need to span 480 Hz. This is not a problem for a fluxgate magnetometer such as the SENSYS, where the 2 kHz bandwidth would span the coil frequencies needed to calibrate the system. However, the bandwidth of a QuSpin Zero-Field OPM is much smaller and rolls off at around 100 Hz (Osborne et al. [2018]). Therefore one would need to either reduce the number of coils in the system (hence decreasing the overall frequency range needed to calibrate the coils), or use a magnetic field sensor which is sensitive enough to measure the femtotesla fields from the brain but which also has a larger bandwidth.

Another factor to consider is that the calibration frequencies assigned to each coil must lie outside the frequency range of the neural oscillations being measured.

Typically, movement related magnetic field artefacts can be characterised as low frequency interference below 10 Hz (see Figure 2.29). Therefore, as the results from Figure 5.8 show that the system can only null fields below 0.2 Hz, continuous calibration and field cancellation must work faster. This could be done by increasing the frequency separation between the coils. By doing so, the recording time needed to resolve the peaks in the FFT is reduced and updates to the coil currents can happen faster. Improvements to the proportional controller, such as adding correctly tuned integral and differential gains, would ensure that responses to changes in the magnetic field would happen quickly and with less overshoot.

Another point to consider is that calculating the inverse of a non-square matrix is computationally intensive. The test rig demonstrated in this thesis has a small number of coils and only one three-axis sensor, and so the time taken to calculate the pseudo inverse is short. For an OPM-MEG system, the number of sensors is large (at the point of writing, the system in Nottingham is formed of 64 three-axis OPMs, which is equivalent to 192 channels). As the number of sensors and coils increase, the computation time will get longer, which will slow down the response time of the field control program.

5.8.2 Other uses

Other uses of this technique could be determining the location of a sensor within a coil system where cameras and optical tracking technology is not available, such as in small magnetic shields with limited space. If the contribution of the magnetic field from each coil over the entire space is known prior to an experiment (either through modelling of the coil the system, or through previous field mapping), then the position of the sensor can be inferred from the evolution of the calibration matrix.

It could also be used to quickly recalibrate coils before ‘normal’ seated OPM-MEG experiments. This would be useful if the position of the nulled region needed to be changed, e.g. if the sensor array was lower down when scanning a seated child or during a standing experiment. Because the participant was not moving around, the nulled volume is static around the array and calibration would only need to happen once.

5.8.3 Alternative approach to moving the nulled volume

Recent experiments carried out by Holmes et al. [2023b] showed that the magnetic field over a sensor array could also be nulled throughout an experiment by using real-time optical tracking data and magnetic field data to characterise the magnetic field over the OPM array using a spherical harmonics model. The coil calibration matrix was updated using the perfect reflection model described earlier. Thus the coil currents could be updated throughout an experiment using a feedback controller as done here, enabling movements that are not constrained to a fixed region.

5.8.4 OPM advancements

Research and development into optically pumped magnetometers is fast and competitive and consequently the sensor technology has moved forward significantly since the work described in this chapter commenced.

The on-board coils that control the magnetic field across the vapour cell in the OPM can now be used in *closed loop* mode but with a dynamic range of ± 15 nT (Robinson et al. [2022]). This means that is is possible to now compensate for changes in the magnetic field across the cell by updating the on-board coil currents, which, in open loop mode, are otherwise fixed throughout an experiment. Whilst this development might possibly in the future eliminate the need for external magnetic field cancellation, more work needs to be done to investigate the interactions between the on-board coils (cross-talk) and how the interactions impact the sensor measurements. Furthermore, any large changes in magnetic field outside of the dynamic range will still need magnetic field compensation with off-board coils. Hence the need for electromagnetic nulling coils in the MSR, and active field compensation using the technique described in this chapter, is not completely eliminated.

5.9 Conclusions

In this chapter a new calibration technique is presented and implemented inside a MuMetal box containing six square electromagnetic nulling coils (one per face). Calibration by continuously pulsing the coils during an experiment is shown to enable continuous calibration and magnetic field cancellation over a moving fluxgate magnetometer. A custom LabVIEW program used to control the system is described. Translation and rotation experiments using a single fluxgate magnetometer are carried out. Finally, applications and limitations of the continuous calibration technique for OPM-MEG are discussed.

Chapter 6

Summary and Closing Remarks

6.1 Summary

This thesis has explored passive and active magnetic shielding solutions, with an emphasis on how these findings can help improve magnetic shielding for OPM-MEG.

In Chapter 3, interactions between passive and active magnetic shielding were investigated. It was shown that an infinite plane model could be used to describe the interactions between a small coil mounted on the inside of a single layer MuMetal shield. At 0.1 Hz, 10 Hz, and 110 Hz (frequencies similar in magnitude to those used to drive the electromagnetic coils in Chapter 5), the interactions can be described as near perfect reflections. The implications of this are that complex calculations are not needed when designing coil systems. There is also no need to consider frequency dependent variation in the magnitude of the field and phase, which is important if electromagnetic coils become mounted on the walls of the MSR, especially if continuous calibration with time-varying fields is implemented (as described in Chapter 5) to null over a moving array of OPMs.

Future work includes incorporating the solutions to the infinite plane model into magnetic field models and coil design, especially as the coils become wall mounted. Furthermore, whilst beyond the scope of this thesis, the infinite plane model can also be used to investigate the effectiveness of a passive magnetic shield by simulating the attenuated field on the opposite side of the plane to the coil. Ongoing research is currently comparing experimental results of the attenuation of a magnetic field produced by a coil on the outside of the MuBin, to the solutions for the infinite plane model. FEM simulations are also being carried out using ANSYS software. If the attenuation of the magnetic field produced by a coil outside of a box can be described by the infinite plane model, it would show that a simpler model (one with fewer boundary conditions) can be used to describe a cubic shield. Other avenues of investigation include modelling the effects of joints or welds on the flow of eddy currents and shunted magnetic fields.

In Chapter 4, shaking was implemented to enhance the shielding performance of a three layer cylindrical MuMetal shield. Without shaking, the shielding factor was ≈ 44,000 between 0.1 Hz and 1 Hz interference, and reached a maximum of 90,000 at 20 Hz. With shaking, improvements in the shielding factor were seen at low frequencies below 1 Hz, with gains of 10% when shaking the outer layer, and further improvements of 20% when shaking the inner layer.

Investigations into enhancing the shielding factor of the MuBin and also the OPM-MEG shielded room via shaking are currently ongoing. This also includes looking into the effects of different amplitudes of the shaking current and different shaking frequencies. Shaking has the potential to enhance shielding factors of lighter shielded rooms with fewer layers. In turn this would make the installation of an OPM-MEG system easier and more affordable.

As well as enhancing the effects of shaking, questions regarding the physical mechanisms of shaking and *how* shaking works is also an interesting avenue of investigation that could be followed.

In Chapter 5, a continuous calibration and field cancellation technique was used to null the magnetic field over a moving fluxgate magnetometer inside a single layer magnetic shield. A LabVIEW program was developed to implement the new method which enabled magnetic field nulling during a rotation and translation experiment.

Although the method demonstrated in Chapter 5 was carried out with a single fluxgate magnetometer with only six coils inside a small-single layer shield, it is possible to see how this system could be scaled up to null the magnetic field during an OPM-MEG experiment- using the existing wall mounted electromagnetic coils in the MSR and measuring the calibration field from each coil using the OPM array. This would enable the magnetic field to be nulled over a moving sensor array during an experiment, allowing participants to move more freely whilst being scanned.

6.2 Closing remarks

Magnetic shielding is an essential part of an OPM-MEG system, and the combination of passive shielding and active shielding using electromagnetic coils has enabled the measurement of magnetic fields from the brain using optically pumped magnetometers.

As electromagnetic coils become wall-mounted to open up space in the MSR, it is important that interactions between coils and ferromagnetic shielding materials such as MuMetal are well understood. Not only do these interactions present interesting physics problems, but knowing how passive and active shielding interact with one another will help to engineer highly efficient magnetic shields.

Exploiting inherent properties of ferromagnetic materials, such as the reordering of domains by driving the material about the hysteresis loop, can enhance the shielding effects without adding more layers of shielding material. Optimising shaking and degaussing procedures, which rely on the hysteretic behaviour of the material properties, are therefore valuable areas of research, whether for use in MSRs for OPM-MEG or for general use in magnetic shielding.

It is an exciting time to be involved in OPM-MEG, not only in our understanding of the brain, but also the new and challenging physics and engineering problems which have arisen during its development, especially with regards to passive and active magnetic shielding.

Bibliography

S. Afach, G. Bison, K. Bodek, F. Burri, Z. Chowdhuri, M. Daum, M. Fertl, B. Franke, Z. Grujic, V. Hélaine, R. Henneck, M. Kasprzak, K. Kirch, H.-C. Koch, A. Kozela, J. Krempel, B. Lauss, T. Lefort, Y. Lemière, M. Meier, O. Naviliat-Cuncic, F. M. Piegsa, G. Pignol, C. Plonka-Spehr, P. N. Prashanth, G. Quéméner, D. Rebreyend, S. Roccia, P. Schmidt-Wellenburg, A. Schnabel, N. Severijns, J. Voigt, A. Weis, G. Wyszynski, J. Zejma, J. Zenner, and G. Zsigmond. Dynamic stabilization of the magnetic field surrounding the neutron electric dipole moment spectrometer at the Paul Scherrer Institute. *Journal of Applied Physics*, 116(8):84510, 2014. ISSN 0021-8979. doi: 10.1063/1.4894158.

F. Allmendinger, B. Brauneis, W. Heil, and U. Schmidt. Degaussing Procedure and Performance Enhancement by Low-Frequency Shaking of a 3-Layer Magnetically Shielded Room. *ArXiv*, pages 1–13, 2023.

I. Altarev, E. Babcock, D. Beck, M. Burghoff, S. Chesnevskaya, T. Chupp, S. Degenkolb, I. Fan, P. Fierlinger, A. Frei, E. Gutsmiedl, S. Knappe-Grüneberg, F. Kuchler, T. Lauer, P. Link, T. Lins, M. Marino, J. McAndrew, B. Niessen, S. Paul, G. Petzoldt, U. Schläpfer, A. Schnabel, S. Sharma, J. Singh, R. Stoepler, S. Stuiber, M. Sturm, B. Taubenheim, L. Trahms, J. Voigt, and T. Zechlau. A magnetically shielded room with ultra low residual field and gradient. *Review of Scientific Instruments*, 85(7), 2014. ISSN 10897623. doi: 10.1063/1.4886146.

I. Altarev, M. Bales, D. H. Beck, T. Chupp, K. Fierlinger, P. Fierlinger, F. Kuchler, T. Lins, M. G. Marino, B. Niessen, G. Petzoldt, U. Schläpfer, A. Schnabel, J. T. Singh, R. Stoepler, S. Stuiber, M. Sturm, B. Taubenheim, and J. Voigt. A large-scale magnetic shield with 106 damping at millihertz frequencies. *Journal of Applied Physics*, 117(18), 2015a. ISSN 10897550. doi: 10.1063/1.4919366.

I. Altarev, P. Fierlinger, T. Lins, M. G. Marino, B. Nießen, G. Petzoldt, M. Reisner, S. Stuiber, M. Sturm, J. Taggart Singh, B. Taubenheim, H. K. Rohrer, and U. Schläpfer. Minimizing magnetic fields for precision experiments. *Journal of Applied Physics*, 117(23):233903, 6 2015b. ISSN 0021-8979. doi: 10.1063/1.4922671.

P. Arpaia, P. N. Burrows, M. Buzio, C. Gohil, M. Pentella, and D. Schulte. Magnetic characterization of Mumetal® for passive shielding of stray fields down to the nano-Tesla level. *Nuclear Instruments and Methods in Physics Research, Section A: Accelerators, Spectrometers, Detectors and Associated Equipment*, 988(December 2020): 164904, 2021. ISSN 01689002. doi: 10.1016/j.nima.2020.164904.

S. Baillet. Magnetoencephalography for brain electrophysiology and imaging. *Nature Neuroscience*, 20(3):327–339, 2017. ISSN 1546-1726. doi: 10.1038/nn.4504.

C. A. Baker, D. D. Doyle, P. Geltenbort, K. Green, M. G. D. van der Grinten, P. G. Harris, P. Iaydjiev, S. N. Ivanov, D. J. R. May, J. M. Pendlebury, J. D. Richardson, D. Shiers, and K. F. Smith. Improved Experimental Limit on the Electric Dipole Moment of the Neutron. *Phys. Rev. Lett.*, 97(13):131801, 9 2006. doi: 10.1103/PhysRevLett.97.131801. URL `https://link.aps.org/doi/10.1103/PhysRevLett.97.131801`.

E. L. Barratt, P. K. Tewarie, M. A. Clarke, E. L. Hall, P. A. Gowland, P. G. Morris, S. T. Francis, N. Evangelou, and M. J. Brookes. Abnormal task driven neural oscillations in multiple sclerosis: A visuomotor MEG study. *Human Brain Mapping*, 38(5):2441–2453, 2017. doi: https://doi.org/10.1002/hbm.23531. URL `https://onlinelibrary.wiley.com/doi/abs/10.1002/hbm.23531`.

J. Bork, H. Hahlbohm, R. Klein, and A. Schnabel. The 8-layered magnetically shielded room of the PTB : Design and construction. *Design*, pages 2–5, 1980.

E. Boto, R. Bowtell, P. Krüger, T. M. Fromhold, P. G. Morris, S. S. Meyer, G. R. Barnes, and M. J. Brookes. On the potential of a new generation of magnetometers for MEG: A beamformer simulation study. *PLoS ONE*, 11(8):1–24, 2016. ISSN 19326203. doi: 10.1371/journal.pone.0157655.

E. Boto, S. S. Meyer, V. Shah, O. Alem, S. Knappe, P. Kruger, T. M. Fromhold, M. Lim, P. M. Glover, P. G. Morris, R. Bowtell, G. R. Barnes, and M. J. Brookes. A new generation of magnetoencephalography: Room temperature measurements using optically-pumped magnetometers. *NeuroImage*, 149(January):404–414, 2017. ISSN 10959572. doi: 10.1016/j.neuroimage.2017.01.034.

E. Boto, N. Holmes, J. Leggett, G. Roberts, V. Shah, S. S. Meyer, L. D. Muñoz, K. J. Mullinger, T. M. Tierney, S. Bestmann, G. R. Barnes, R. Bowtell, and M. J. Brookes. Moving magnetoencephalography towards real-world applications with a wearable system. *Nature*, 555(7698):657–661, 2018. ISSN 14764687. doi: 10.1038/nature26147.

R. M. R. M. Bozorth. *Ferromagnetism / Richard M. Bozorth.* Bell Telephone Laboratories series. Van Nostrand, Princeton, N.J., 1951.

M. J. Brookes, J. Leggett, M. Rea, R. M. Hill, N. Holmes, E. Boto, and R. Bowtell. Magnetoencephalography with optically pumped magnetometers (OPM-MEG): the next generation of functional neuroimaging. *Trends in Neurosciences*, 45(8):621–634, 2022. ISSN 1878108X. doi: 10.1016/j.tins.2022.05.008.

S. Celozzi, R. Araneo, and G. Lovat. Electromagnetic Shielding. In *Electromagnetic Shielding*, pages 282–316. 2008. ISBN 9780470055366. doi: 10.1002/9780470268483.

Cestriom. Degaussing. URL `https://cestriom.com/en/technology/demagnetization-basics/`.

J. Clarke. Josephson Junction Detectors. *Science*, 184(4143):1235–1242, 11 1974. ISSN 00368075, 10959203. URL `http://www.jstor.org/stable/1738057`.

D. Cohen. ENHANCEMENT OF FERROMAGNETIC SHIELDING AGAINST LOW-FREQUENCY MAGNETIC FIELDS. *Applied Physics Letters*, 10(3):67–69, 11 1967. ISSN 0003-6951. doi: 10.1063/1.1754854.

D. Cohen. Magnetoencephalography: detection of the brain's electrical activity with a superconducting magnetometer. *Science (New York, N.Y.)*, 175(4022):664–666, 2 1972. ISSN 0036-8075 (Print). doi: 10.1126/science.175.4022.664.

D. Cohen, U. Schläpfer, S. Ahlfors, M. Hämäläinen, and E. Halgren. New six-layer magnetically-shielded room for MEG. *Biomag Proceed*, (8000):10–12, 2002. URL `http://www.martinos.org/meg/pdfs/2002BiomagProceed(ourMSR).pdf`.

J. S. Ebersole. Magnetoencephalography/Magnetic Source Imaging in the Assessment of Patients with Epilepsy. *Epilepsia*, 38(s4):S1–S5, 1997. doi: https://doi.org/10.1111/j.1528-1157.1997.tb04533.x. URL `https://onlinelibrary.wiley.com/doi/abs/10.1111/j.1528-1157.1997.tb04533.x`.

O. Feys, P. Corvilain, A. Aeby, C. Sculier, N. Holmes, M. Brookes, S. Goldman, V. Wens, and X. De Tiège. On-Scalp Optically Pumped Magnetometers versus Cryogenic Magnetoencephalography for Diagnostic Evaluation of Epilepsy in School-aged Children. *Radiology*, 304(2):429–434, 5 2022. ISSN 0033-8419. doi: 10.1148/radiol.212453.

O. Feys, P. Corvilain, J. Bertels, C. Sculier, N. Holmes, M. Brookes, V. Wens, and X. De Tiège. On-scalp magnetoencephalography for the diagnostic evaluation of epilepsy during infancy. *Clinical Neurophysiology*, 155:29–31, 2023. ISSN 1388-2457. doi: https://doi.org/10.1016/j.clinph.2023.08.010.

J. Füzer, P. Kollár, D. Olekšáková, and S. Roth. AC magnetic properties of the bulk Fe-Ni and Fe-Ni-Mo soft magnetic alloys prepared by warm compaction. *Journal of Alloys and Compounds*, 483(1-2):557–559, 2009. ISSN 09258388. doi: 10.1016/j.jallcom.2008.08.137.

L. E. Gascoyne, M. J. Brookes, M. Rathnaiah, M. Z. U. H. Katshu, L. Koelewijn, G. Williams, J. Kumar, J. T. R. Walters, Z. A. Seedat, L. Palaniyappan, J. F. W. Deakin, K. D. Singh, P. F. Liddle, and P. G. Morris. Motor-related oscillatory activity in schizophrenia according to phase of illness and clinical symptom severity. *NeuroImage: Clinical*, 29:102524, 2021. ISSN 2213-1582. doi: https://doi.org/10.1016/j.nicl.2020.102524. URL `https://www.sciencedirect.com/science/article/pii/S2213158220303612`.

I. S. I. S. Grant. *Electromagnetism / I.S. Grant, W.R. Phillips.* Manchester physics series. John Wiley & Sons, Chichester, 2nd ed. edition, 1990. ISBN 0471927112.

M. Hämäläinen, R. Hari, R. J. Ilmoniemi, J. Knuutila, and O. V. Lounasmaa. Magnetoencephalography—theory, instrumentation, and applications to noninvasive studies of the working human brain. *Rev. Mod. Phys.*, 65(2):413–497, 4 1993. doi: 10.1103/RevModPhys.65.413.

P. Hansen, M. Kringelbach, and R. Salmelin. *MEG: An Introduction to Methods.* Oxford University Press, 2010. ISBN 9780195307238. doi: 10.1093/acprof:oso/9780195307238.001.0001. URL `https://doi.org/10.1093/acprof:oso/9780195307238.001.0001`.

S. S. Hidalgo-Tobon. Theory of gradient coil design methods for magnetic resonance imaging. *Concepts in Magnetic Resonance Part A*, 36A(4):223–242, 2010. doi: https://doi.org/10.1002/cmr.a.20163.

R. M. Hill, E. Boto, N. Holmes, C. Hartley, Z. A. Seedat, J. Leggett, G. Roberts, V. Shah, T. M. Tierney, M. W. Woolrich, C. J. Stagg, G. R. Barnes, R. Bowtell, R. Slater, and M. J. Brookes. A tool for functional brain imaging with lifespan compliance. *Nature Communications*, 10(1):4785, 2019. ISSN 2041-1723. doi: 10.1038/s41467-019-12486-x. URL `https://doi.org/10.1038/s41467-019-12486-x`.

R. M. Hill, E. Boto, M. Rea, N. Holmes, J. Leggett, L. A. Coles, M. Papastavrou, S. K. Everton, B. A. E. Hunt, D. Sims, J. Osborne, V. Shah, R. Bowtell, and M. J. Brookes. Multi-channel whole-head OPM-MEG: Helmet design and a comparison with a conventional system. *NeuroImage*, 219:116995, 2020. ISSN 1053-8119. doi: https://doi.org/10.1016/j.neuroimage.2020.116995.

P. J. Hobson, J. Vovrosh, B. Stray, M. Packer, J. Winch, N. Holmes, F. Hayati, K. McGovern, R. Bowtell, M. J. Brookes, K. Bongs, T. M. Fromhold, and M. Holynski. Bespoke magnetic field design for a magnetically shielded cold atom interferometer. *Scientific Reports*, 12(1):1–12, 2022. ISSN 20452322. doi: 10.1038/s41598-022-13979-4. URL `https://doi.org/10.1038/s41598-022-13979-4`.

P. J. Hobson, N. Holmes, P. Patel, B. Styles, J. Chalmers, C. Morley, A. Davis, M. Packer, T. X. Smith, S. Raudonyte, D. Holmes, R. Harrison, D. Woolger, D. Sims, M. J. Brookes, R. Bowtell, and M. Fromhold. Benchtop Magnetic Shielding for Benchmarking Atomic Magnetometers. *IEEE Transactions on Instrumentation and Measurement*, 72:1–9, 2023. ISSN 15579662. doi: 10.1109/TIM.2023.3293540.

N. Holmes, J. Leggett, E. Boto, G. Roberts, R. M. Hill, T. M. Tierney, V. Shah, G. R. Barnes, M. J. Brookes, and R. Bowtell. A bi-planar coil system for nulling background magnetic fields in scalp mounted magnetoencephalography. *NeuroImage*, 181(April): 760–774, 2018. ISSN 10959572. doi: 10.1016/j.neuroimage.2018.07.028.

N. Holmes, T. M. Tierney, J. Leggett, E. Boto, S. Mellor, G. Roberts, R. M. Hill, V. Shah, G. R. Barnes, M. J. Brookes, and R. Bowtell. Balanced, bi-planar magnetic field and field gradient coils for field compensation in wearable magnetoencephalography. *Scientific Reports*, 9(1):1–15, 2019. ISSN 20452322. doi: 10.1038/s41598-019-50697-w.

N. Holmes, M. Rea, J. Chalmers, J. Leggett, L. J. Edwards, P. Nell, S. Pink, P. Patel, J. Wood, N. Murby, D. Woolger, E. Dawson, C. Mariani, T. M. Tierney, S. Mellor, G. C. O'Neill, E. Boto, R. M. Hill, V. Shah, J. Osborne, R. Pardington, P. Fierlinger,

G. R. Barnes, P. Glover, M. J. Brookes, and R. Bowtell. A lightweight magnetically shielded room with active shielding. *Scientific Reports*, 12(1):1–13, 2022. ISSN 20452322. doi: 10.1038/s41598-022-17346-1.

N. Holmes, M. Rea, R. M. Hill, E. Boto, J. Leggett, L. J. Edwards, N. Rhodes, V. Shah, J. Osborne, T. M. Fromhold, P. Glover, P. R. Montague, M. J. Brookes, and R. Bowtell. Naturalistic Hyperscanning with Wearable Magnetoencephalography. *Sensors*, 23(12): 5454, 2023a. ISSN 14248220. doi: 10.3390/s23125454.

N. Holmes, M. Rea, R. M. Hill, J. Leggett, L. J. Edwards, P. J. Hobson, E. Boto, T. M. Tierney, L. Rier, G. R. Rivero, V. Shah, J. Osborne, T. M. Fromhold, P. Glover, M. J. Brookes, and R. Bowtell. Enabling ambulatory movement in wearable magnetoencephalography with matrix coil active magnetic shielding. *NeuroImage*, 274:120157, 2023b. ISSN 1053-8119. doi: https://doi.org/10.1016/j.neuroimage.2023.120157. URL `https://www.sciencedirect.com/science/article/pii/S1053811923003087`.

C.-K. Hou. The effects of grain size on the magnetic properties of fully processed, continuous-annealed low-carbon electrical steels. *IEEE Transactions on Magnetics*, 32(2):471–477, 1996. doi: 10.1109/20.486534.

V. Kelhä, R. Peltonen, and B. Rantala. The Effect of Shaking on Magnetic Shields. *IEEE Transactions on Magnetics*, MAG-16(4):575–578, 1980. ISSN 19410069. doi: 10.1109/TMAG.1980.1060655.

C. Kittel. Untersuchung von Einflußfaktoren auf den magnetischen Schirmfaktor eines MU-Metall Zylinders. *Technische Hochshule Lübek*, Diplomarbe, 2010.

F. Lopes da Silva. EEG and MEG: Relevance to neuroscience. *Neuron*, 80(5):1112–1128, 2013. ISSN 08966273. doi: 10.1016/j.neuron.2013.10.017.

A. J. Mager. Magnetic Shields. *IEEE Transactions on Magnetics*, 6(1):67–75, 1970. ISSN 19410069. doi: 10.1109/TMAG.1970.1066714.

Magnetic Shield Corp. MuMetal technical data. URL `https://www.magnetic-shield.com/mumetal-technical-data/`.

Magnetic Shields Ltd. Heat treatment MSL, a. URL `https://www.magneticshields.co.uk/service-heat-treatment`.

Magnetic Shields Ltd. MuMetal B-H curve. b. URL `http://mumetal.co.uk/?p=109`.

A. J. Mäkinen, R. Zetter, J. Iivanainen, K. C. J. Zevenhoven, L. Parkkonen, and R. J. Ilmoniemi. Magnetic-field modeling with surface currents: Physical and computational principles of bfieldtools. 2020.

S. Mellor, T. M. Tierney, G. C. OaNeill, N. Alexander, R. A. Seymour, N. Holmes, J. D. Lopez, R. M. Hill, E. Boto, M. Rea, G. Roberts, J. Leggett, R. Bowtell, M. J. Brookes, E. A. Maguire, M. C. Walker, and G. R. Barnes. Magnetic Field Mapping and Correction for Moving OP-MEG. *IEEE transactions on bio-medical engineering*, 69 (2):528–536, 2 2022. ISSN 1558-2531 (Electronic). doi: 10.1109/TBME.2021.3100770.

K. Nagashima, I. Sasada, and K. Tashiro. High-performance bench-top cylindrical magnetic shield with magnetic shaking enhancement. *IEEE Transactions on Magnetics*, 38(5 I):3335–3337, 2002. ISSN 00189464. doi: 10.1109/TMAG.2002.803123.

J. Osborne, J. Orton, O. Alem, and V. Shah. Fully integrated, standalone zero field optically pumped magnetometer for biomagnetism. (February):51, 2018. ISSN 1996756X. doi: 10.1117/12.2299197.

M. Packer, P. J. Hobson, N. Holmes, J. Leggett, P. Glover, M. J. Brookes, R. Bowtell, and T. M. Fromhold. Optimal Inverse Design of Magnetic Field Profiles in a Magnetically Shielded Cylinder. *Physical Review Applied*, 14(5):1, 2020. ISSN 23317019. doi: 10.1103/PhysRevApplied.14.054004. URL `https://doi.org/10.1103/PhysRevApplied.14.054004`.

M. Packer, P. J. Hobson, A. Davis, N. Holmes, J. Leggett, P. Glover, N. L. Hardwicke, M. J. Brookes, R. Bowtell, and T. M. Fromhold. Magnetic field design in a cylindrical high-permeability shield: The combination of simple building blocks and a genetic algorithm. *Journal of Applied Physics*, 131(9):93902, 2022. ISSN 0021-8979. doi: 10.1063/5.0071986. URL `https://doi.org/10.1063/5.0071986`.

D. Platzek, H. Nowak, F. Giessler, J. Röther, and M. Eiselt. Active shielding to reduce low frequency disturbances in direct current near biomagnetic measurements. *Review of Scientific Instruments*, 70(5):2465–2470, 5 1999. ISSN 0034-6748. doi: 10.1063/1.1149779. URL `https://doi.org/10.1063/1.1149779`.

S. Rampp, H. Stefan, X. Wu, M. Kaltenhäuser, B. Maess, F. C. Schmitt, C. H. Wolters, H. Hamer, B. S. Kasper, S. Schwab, A. Doerfler, I. Blümcke, K. Rössler, and M. Buchfelder. Magnetoencephalography for epileptic focus localization in a series of 1000 cases. *Brain : a journal of neurology*, 142(10):3059–3071, 10 2019. ISSN 1460-2156 (Electronic). doi: 10.1093/brain/awz231.

M. Rea, N. Holmes, R. M. Hill, E. Boto, J. Leggett, L. J. Edwards, D. Woolger, E. Dawson, V. Shah, J. Osborne, R. Bowtell, and M. J. Brookes. NeuroImage Precision magnetic field modelling and control for wearable magnetoencephalography. *NeuroImage*, 241(December 2020):118401, 2021. ISSN 1053-8119. doi: 10.1016/j.neuroimage.2021.118401.

S. E. Robinson, A. B. Andonegui, T. Holroyd, K. J. Hughes, O. Alem, S. Knappe, T. Maydew, A. Griesshammer, and A. Nugent. Cross-Axis Dynamic Field Compensation of Optically Pumped Magnetometer Arrays for MEG. *NeuroImage*, 262:119559, 2022. ISSN 1053-8119. doi: https://doi.org/10.1016/j.neuroimage.2022.119559.

S. Robson, M. Brookes, L. Palaniyappan, J. Kumar, M. Skelton, N. Christodoulou, A. Qureshi, F. Jan, M. Z. U. H. Katshu, E. Liddle, P. Liddle, and P. Morris. Abnormal visuomotor processing in schizophrenia. *NeuroImage: Clinical*, 12, 9 2015. doi: 10.1016/j.nicl.2015.08.005.

I. Sasada, S. Kubo, and K. Harada. Effective shielding for low level magnetic fields. *Journal of Applied Physics*, 5698(64):5696–5698, 1988.

H. Schofield, E. Boto, V. Shah, R. M. Hill, J. Osborne, M. Rea, C. Doyle, N. Holmes, R. Bowtell, D. Woolger, and M. J. Brookes. Quantum enabled functional neuroimaging: the why and how of magnetoencephalography using optically pumped magnetometers. *Contemporary Physics*, 63(3):161–179, 7 2022. ISSN 0010-7514. doi: 10.1080/00107514.2023.2182950. URL `https://doi.org/10.1080/00107514.2023.2182950`.

T. Schurig. Cool sensing. *Nature Physics*, 15(8):870, 2019. ISSN 17452481. doi: 10.1038/s41567-019-0604-7. URL `http://dx.doi.org/10.1038/s41567-019-0604-7`.

R. A. Seymour, N. Alexander, S. Mellor, G. C. O'Neill, T. M. Tierney, G. R. Barnes, and E. A. Maguire. Using OPMs to measure neural activity in standing, mobile participants. *NeuroImage*, 244:118604, 12 2021. ISSN 1095-9572 (Electronic). doi: 10.1016/j.neuroimage.2021.118604.

V. Shah and M. V. Romalis. Spin-exchange relaxation-free magnetometry using elliptically polarized light. *Physical Review A - Atomic, Molecular, and Optical Physics*, 80 (1):1–6, 2009. ISSN 10502947. doi: 10.1103/PhysRevA.80.013416.

V. Shah, S. Knappe, P. D. Schwindt, and J. Kitching. Subpicotesla atomic magnetometry with a microfabricated vapour cell. *Nature Photonics*, 1(11):649–652, 2007. ISSN 17494885. doi: 10.1038/nphoton.2007.201.

S. Skogestad. *Multivariable feedback control : analysis and design / Sigurd Skogestad, Ian Postlethwaite.* John Wiley & Sons, Chichester, 2nd ed. edition, 2005. ISBN 047001167X.

T. M. Tierney, N. Holmes, S. Mellor, J. D. López, G. Roberts, R. M. Hill, E. Boto, J. Leggett, V. Shah, M. J. Brookes, R. Bowtell, and G. R. Barnes. Optically pumped magnetometers: From quantum origins to multi-channel magnetoencephalography. *NeuroImage*, 199:598–608, 10 2019. ISSN 1095-9572 (Electronic). doi: 10.1016/j.neuroimage.2019.05.063.

S. A. Winkler, F. Schmitt, H. Landes, J. de Bever, T. Wade, A. Alejski, and B. K. Rutt. Gradient and shim technologies for ultra high field MRI. *NeuroImage*, 168: 59–70, 3 2018. ISSN 10538119. doi: 10.1016/j.neuroimage.2016.11.033. URL `https://linkinghub.elsevier.com/retrieve/pii/S1053811916306498`.

V. V. Yashchuk, S.-K. Lee, and E. Paperno. Magnetic shielding. In D. Budker and D. F. Jackson Kimball, editors, *Optical Magnetometry*, page 225–248. Cambridge University Press, 2013. doi: 10.1017/CBO9780511846380.013.

L. Zhou, C. Davis, and P. Kok. Steel microstructure – Magnetic permeability modelling: The effect of ferrite grain size and phase fraction. *Journal of Magnetism and Magnetic Materials*, 519:167439, 2021. ISSN 0304-8853. doi: https://doi.org/10.1016/j.jmmm.2020.167439.

J. E. Zimmerman, P. Thiene, and J. T. Harding. Design and Operation of Stable rf-Biased Superconducting Point-Contact Quantum Devices, and a Note on the Properties of Perfectly Clean Metal Contacts. *Journal of Applied Physics*, 41(4):1572–1580, 12 1970. ISSN 0021-8979. doi: 10.1063/1.1659074. URL `https://doi.org/10.1063/1.1659074`.

Appendices

Appendix A

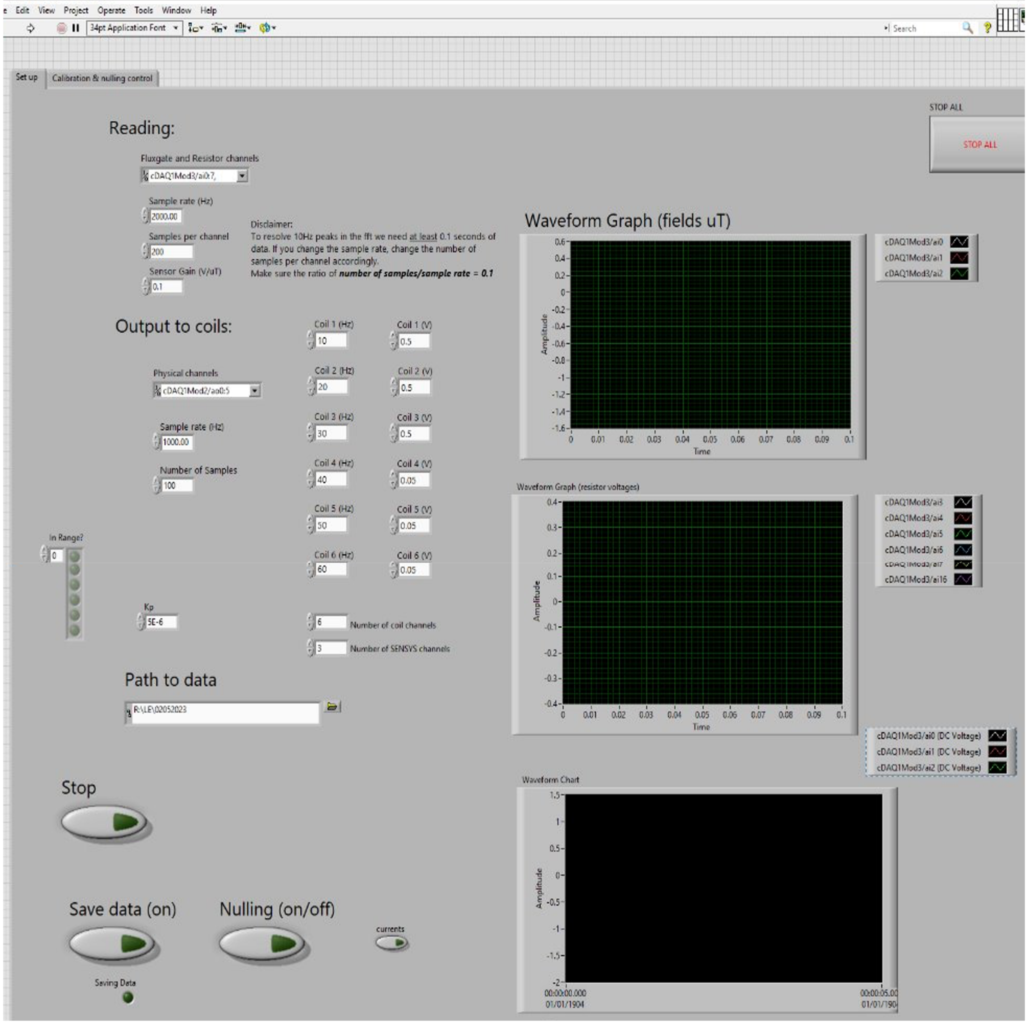

Fluxgate and Resistor channels: cDAQ1Mod3/ai0:7,

Sample rate (Hz): 2000.00

Samples per channel: 200

Sensor Gain (V/uT): 0.1

Disclaimer:
To resolve 10Hz peaks in the fft we need <u>at least</u> 0.1 seconds of data. If you change the sample rate, change the number of samples per channel accordingly.
Make sure the ratio of ***number of samples/sample rate = 0.1***

Physical channels: cDAQ1Mod2/ao0:5

Sample rate (Hz): 1000.00

Number of Samples: 100

Coil 1 (Hz): 10
Coil 1 (V): 0.5
Coil 2 (Hz): 20
Coil 2 (V): 0.5
Coil 3 (Hz): 30
Coil 3 (V): 0.5
Coil 4 (Hz): 40
Coil 4 (V): 0.05
Coil 5 (Hz): 50
Coil 5 (V): 0.05
Coil 6 (Hz): 60
Coil 6 (V): 0.05

In Range?: 0

Kp: 5E-6

Number of coil channels: 6

Number of SENSYS channels: 3

Path to data: R:\LE\02052023

Figure 6.1: *A screenshot of the front panel of the LabVIEW program developed to implement continuous calibration over a moving sensor (see Chapter 5). Users are able to update the channels that are sampled, the sample rate and also the number of samples per channel. The sensor gain and the proportional gain, k_p can also be changed. A path where data will be saved can be defined. Users are also able to change the frequency and voltage output to each coil before running the program. Three charts which update throughout an experiment display the measured magnetic field in μT, the measured voltage across the in-series resistors, and the change in the DC magnetic field in μT. The user can press buttons on the front panel during an experiment to save the data to a file by pressing the "Save data" button, turn the nulling on and off using the "Nulling" button, and also stop the experiment.*

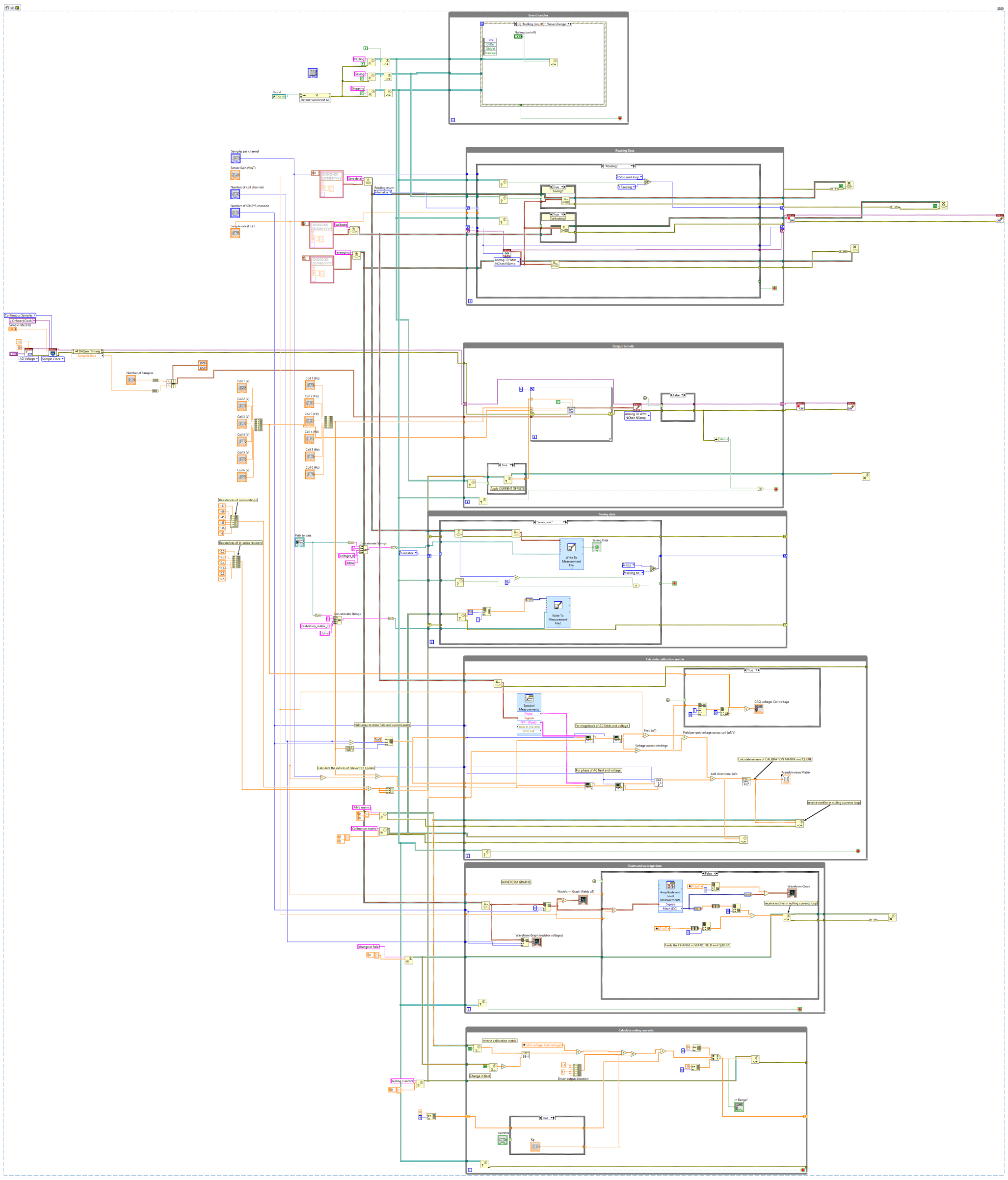

Figure 6.2: *A screenshot of the main LabVIEW block diagram developed to implement continuous calibration over a moving sensor (see Chapter 5).*

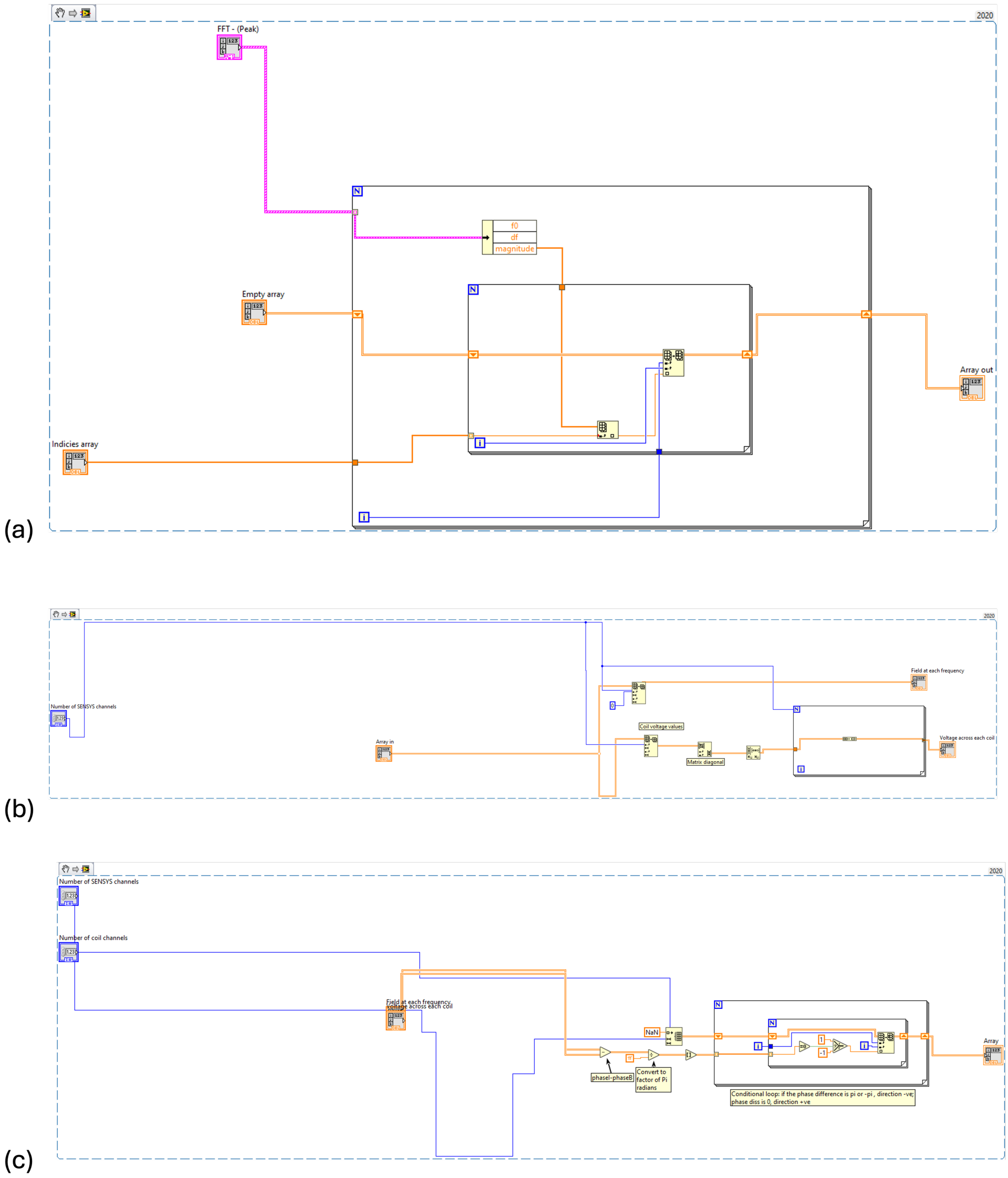

Conditional loop: if the phase difference is pi or -pi , direction -ve; phase diss is 0, direction +ve

Figure 6.3: *A screenshot of the sub VI block diagrams which were developed to be called inside the main LabVIEW block diagram (see Figure 6.2). (a) Shows a program which extracts the amplitude in a FFT at a specified frequency (as described in Section 5.5.2). (b) A screenshot of a program which finds the ratio of the field components per unit current for all coils. (c) Shows a screenshot of a program which calculates the direction of the field per unit current produced by each coil (see Section 5.5.3).*

Appendix B

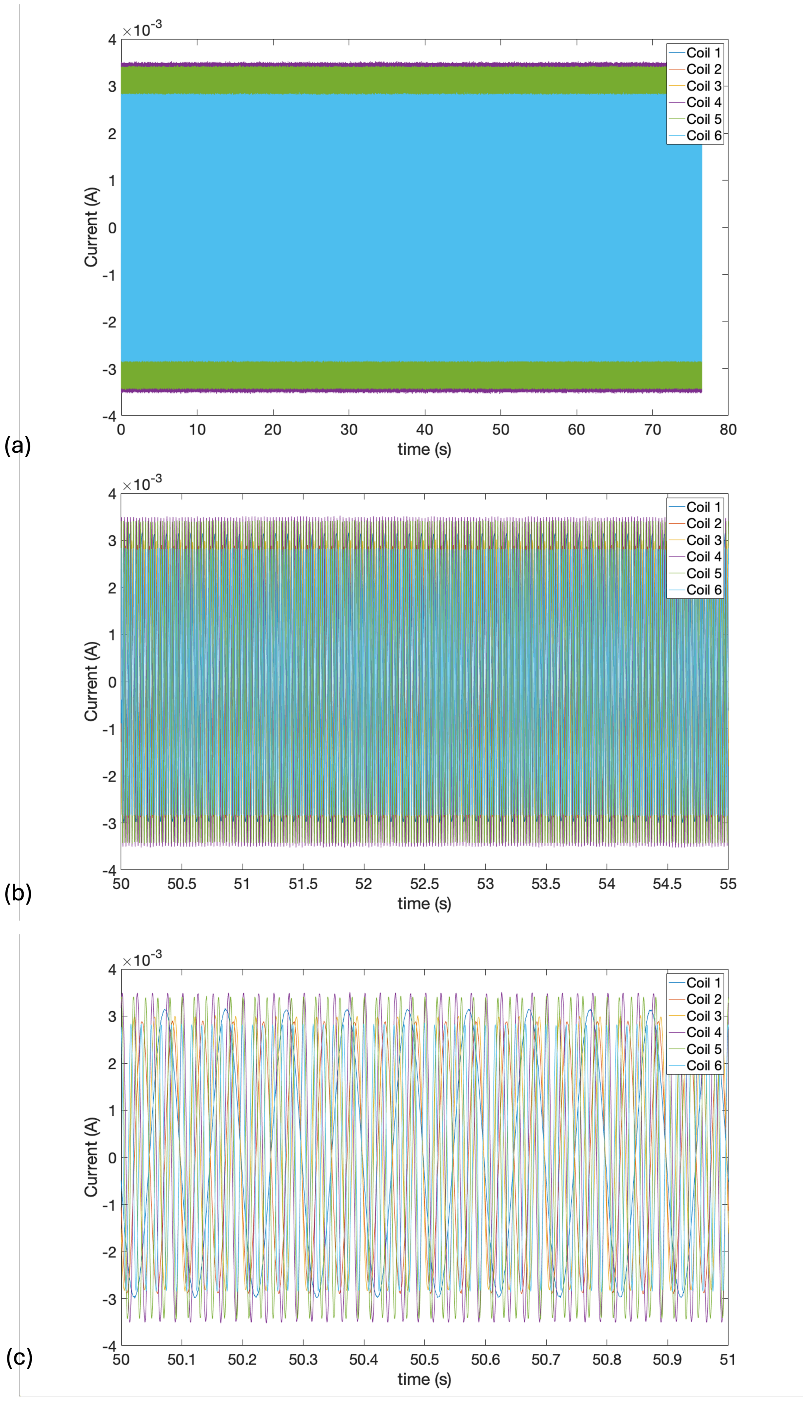

Figure 6.4: *Graphs showing a single data set collected during a continuous calibration experiment with a stationary sensor to investigate the response of the system when applying an AC interference magnetic field (Section 5.7.2). The data shown were collected whilst the proportional gain,* K_p*= 0 (i.e. nulling off). The frequency of the interference field was 0.1 Hz with an amplitude of* $\approx$ *20 nT. Each of the graphs show the measured current in amps for each coil, where coils 1 to 6 are shown in dark blue, red, yellow, purple, green, and light blue, respectively. Each graph is from the same data set, but due to the high frequencies of the coil currents, the time window on the x axis is reduced to show the underlying form of the coil currents. (a) Shows the entire data set. (b) Shows a 5 second window between 50 s to 55 s. (c) Shows a 1 second window between 50 s and 51 s.*

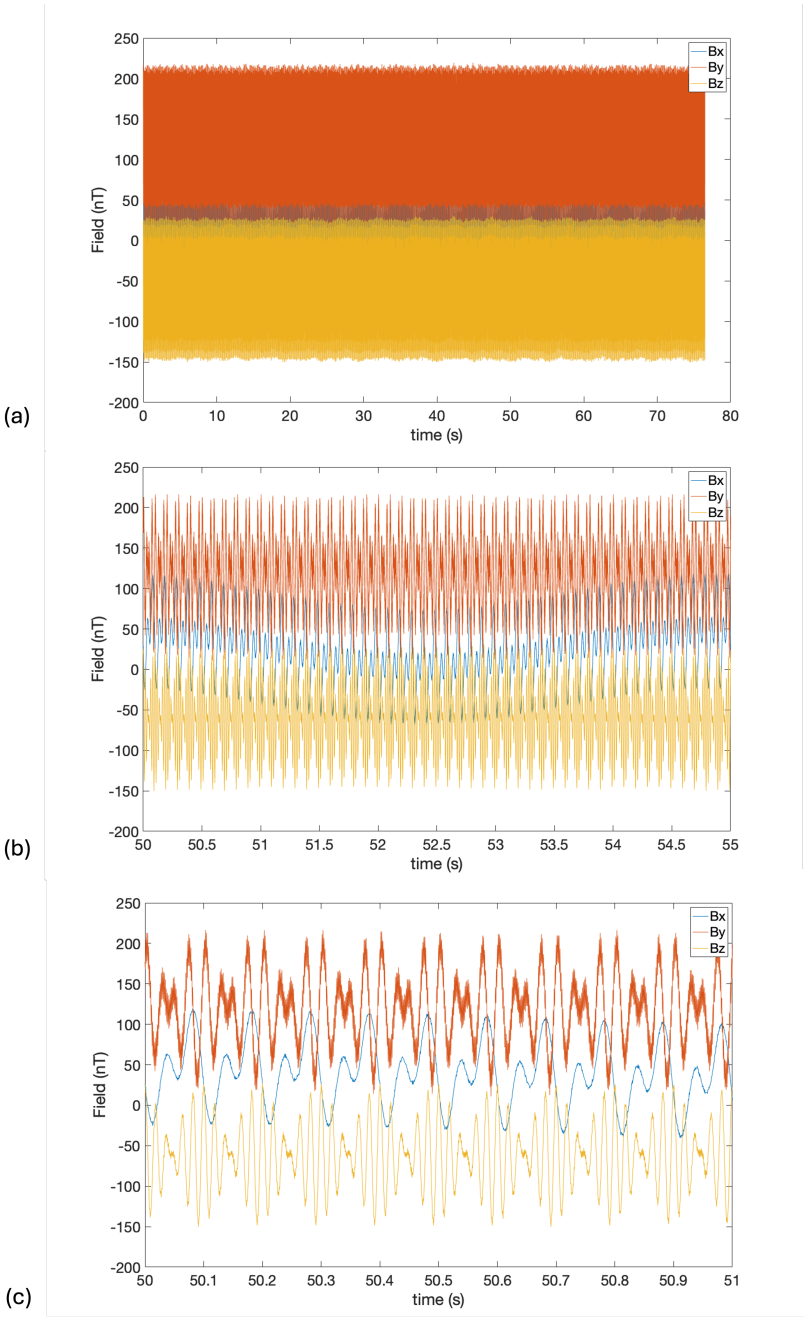

Figure 6.5: *Graphs showing a single data set collected during a continuous calibration experiment with a stationary sensor to investigate the response of the system when applying an AC interference magnetic field (Section 5.7.2). The data shown were collected whilst the proportional gain,* K_p *= 0 (i.e. nulling off). The frequency of the interference field was 0.1 Hz with an amplitude of* $\approx$ *20 nT. Each of the graphs show the component of the magnetic fields measured by the fluxgate magnetometer.* B_x*,* B_y*, and* B_z *are plotted in blue, red, and yellow respectively. Each graph is from the same data set, but the time window on the x axis is reduced to show the underlying form of the magnetic field over a smaller timescale. (a) Shows the entire data set. (b) Shows a 5 second window between 50 s to 55 s. (c) Shows a 1 second window between 50 s and 51 s.*

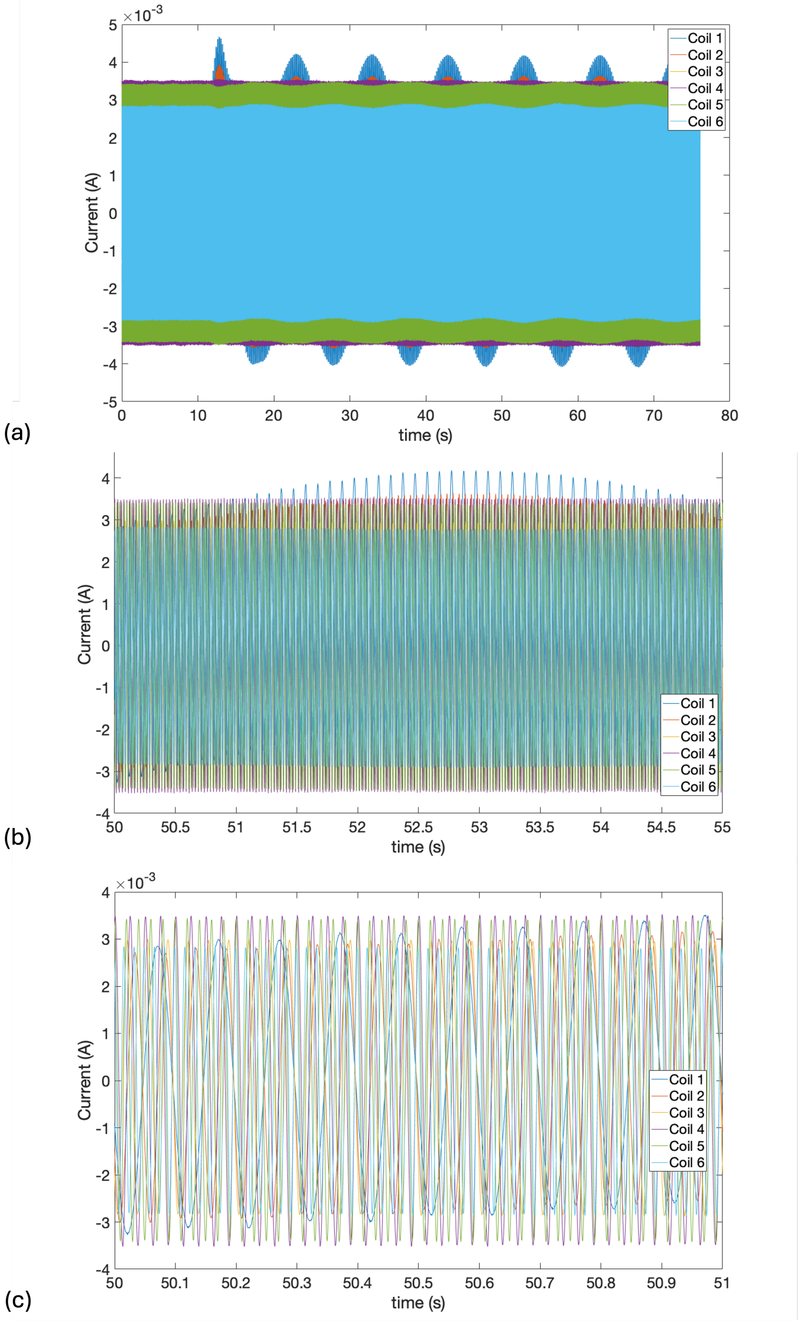

Figure 6.6: *Graphs showing a single data set collected during a continuous calibration experiment with a stationary sensor to investigate the response of the system when applying an AC interference magnetic field (Section 5.7.2). The data shown were collected whilst the proportional gain,* K_p*= 0.2 (i.e. nulling on). The frequency of the interference field was 0.1 Hz with an amplitude of ≈ 20 nT. Each of the graphs show the measured current in amps for each coil, where coils 1 to 6 are shown in dark blue, red, yellow, purple, green, and light blue, respectively. Each graph is from the same data set, but due to the high frequencies of the coil currents, the time window on the x axis is reduced to show the underlying form of the coil currents. (a) Shows the entire data set. (b) Shows a 5 second window between 50 s to 55 s. (c) Shows a 1 second window between 50 s and 51 s.*

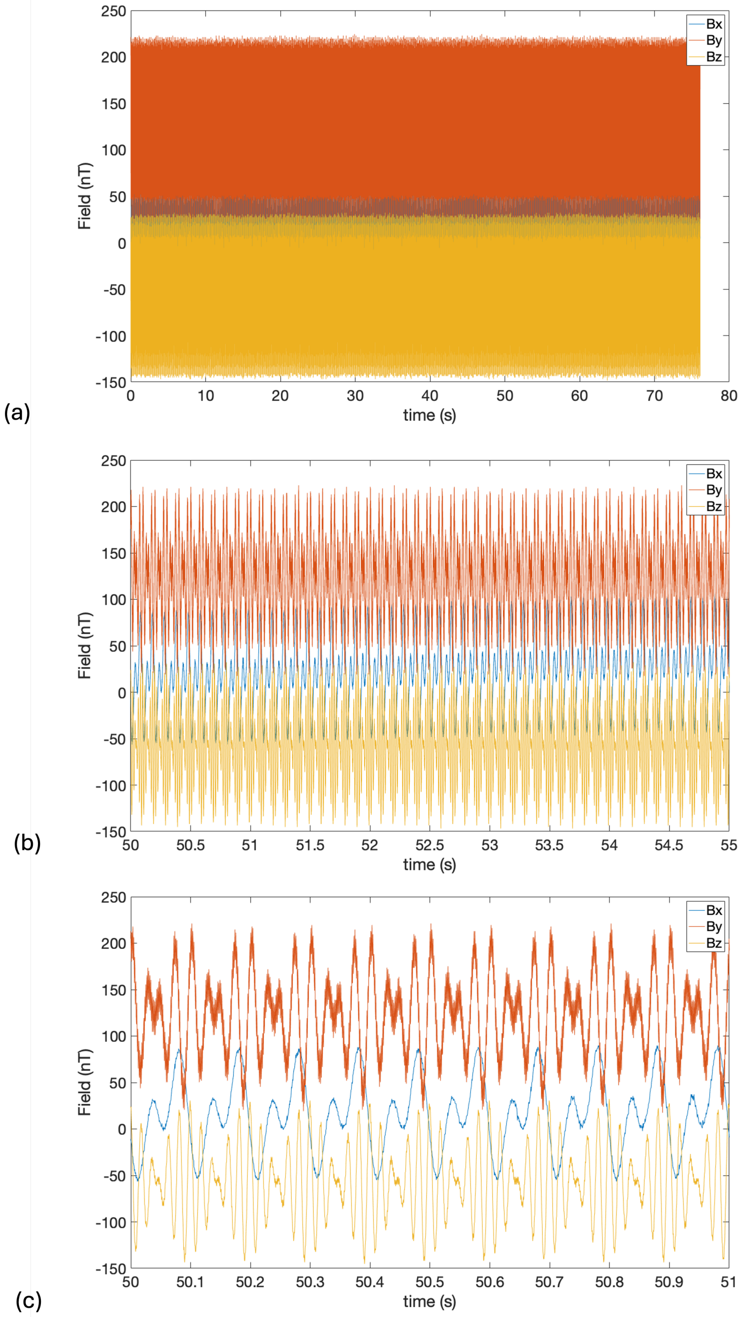

Figure 6.7: *Graphs showing a single data set collected during a continuous calibration experiment with a stationary sensor to investigate the response of the system when applying an AC interference magnetic field (Section 5.7.2). The data shown were collected whilst the proportional gain,* $K_p = 0.2$ *(i.e. nulling on). The frequency of the interference field was 0.1 Hz with an amplitude of* ≈ 20 *nT. Each of the graphs show the component of the magnetic fields measured by the fluxgate magnetometer.* B_x*,* B_y*, and* B_z *are plotted in blue, red, and yellow respectively. Each graph is from the same data set, but the time window on the* x *axis is reduced to show the underlying form of the magnetic field over a smaller timescale. (a) Shows the entire data set. (b) Shows a 5 second window between 50 s to 55 s. (c) Shows a 1 second window between 50 s and 51 s.*